# Tidally induced non-adiabatic stellar oscillations:

# How planets make stars wobble


Andrew Bunting

St John's College

University of Oxford

A thesis submitted for the degree of

*Doctor of Philosophy*

Trinity 2020

# Statement of Originality

I declare that this thesis is entirely my own work and, except where stated, describes my own research.

Some of this research has also been published in Bunting et al. (2019) or has been submitted to be published, and is reproduced here with the permission of the authors and Oxford University Press.

### Bunting et al. (2019)

"Non-adiabatic tidal oscillations induced by a planetary companion" by A. Bunting, John C. B. Papaloizou and Caroline Terquem, 2019, https://doi.org/10.1093/mnras/stz2561.

### Bunting & Terquem, 2020

"Tidally induced stellar oscillations: converting modelled oscillations excited by hot Jupiters into observables" by A. Bunting and Caroline Terquem, 2020, submitted to the Monthly Notices of the Royal Astronomical Society

# Acknowledgements

I am very grateful to my supervisor, Caroline Terquem, for her help, support and guidance throughout my research, to John Papaloizou for his insight and wisdom, and to the many friends at Oxford Astrophysics for their encouragement and humour. I would like to thank the Science and Technology Facilities Council (STFC) for their financial support through grant ST/N504233/1.

I would not have been able to complete this project without my friends and family, to whom I am indebted for their persistent love, care and reminders that there is more to life than physics. I am especially thankful for Affi, who has been an unrelenting support and joy in innumerable ways.

Finally, I am thankful to God, for creating such a gloriously complex universe which we can study, and for sustaining me every day: "The LORD is my light and my salvation" (Psalm 27:1a).

# Abstract

We calculate the dynamical tides raised by a close planetary companion on non–rotating stars of 1 $M_\odot$ and 1.4 $M_\odot$. Using the Henyey method, we solve the fully non–adiabatic equations throughout the star, both for the case of frozen convection and for the case where an approximation for the perturbation to the convective flux is used. The horizontal Lagrangian displacement is found to be 10 to 100 times larger than the equilibrium tide value in a thin region near the surface of the star. This is because non–adiabatic effects dominate in a region that extends from below the outer edge of the convection zone up to the stellar surface, and the equilibrium tide approximation is inconsistent with non–adiabaticity. We derive analytical estimates which give a good approximation to the numerical values of the magnitude of the ratio of the horizontal and radial displacements at the surface.

We calculate the conversion of these oscillations into observable spectroscopic and photometric signals. Observables are calculated for some real planetary systems to give specific predictions. Time–dependent line broadening and the radial velocity signal during transit are both investigated as methods to provide further insight into the nature of the stellar oscillations. The photometric signal is predicted to be roughly proportional to the inverse square of the orbital period, $P^{-2}$, as in the equilibrium tide approximation. However, the radial velocity signal is predicted to be proportional to $P^{-1}$, and is therefore much larger at long orbital periods than the signal corresponding to the equilibrium tide approximation, which is proportional to $P^{-3}$. The prospects for detecting these oscillations and the implications for the detection and characterisation of planets are discussed.

# Contents

# List of Figures

# Chapter 1

# Introduction

Whilst the 'twinkle, twinkle' of the nursery rhyme (Taylor & Taylor, 1806) is an effect of the atmosphere (Jakeman et al., 1978), stars have been known to vary for millennia. The variation of Algol, an eclipsing binary, was tied to lucky and unlucky days in ancient Egypt as early as $\sim 1200$ BC (Jetsu & Porceddu, 2015), and Mira variables (red giant stars with brightness variations on a timescale of several months) had been recorded as varying in brightness by $\sim 100$ BC (Hoffleit, 1997).

Periodic oscillations have also been observed in our nearest star, the sun, and evidence for large-scale velocity fields at the solar surface mounted throughout the $20^{\text{th}}$ century (Plaskett (1916); Hart (1954)), with short-lived oscillations being attributed to large-scale motions in the photosphere (Leighton et al. (1962); Howard & Harvey (1970); Ulrich (1970)).

Similar oscillations have since been observed in other stars, with p-mode oscillations (where the restoring force is due to pressure gradients) tentatively being observed on Procyon using radial velocity (RV) measurements (Brown et al., 1991), and $\eta$ Boo being observed to oscillate at 21 different frequencies, including non-radial modes (Kjeldsen et al., 2003).

These stellar oscillations have also been discussed in the context of classical pulsators, such as $\beta$ Cephei pulsators (Heynderickx et al., 1994), $\delta$ Scuti variables (Garg et al., 2010), and RR Lyrae stars (Dziembowski, 2016). Whilst much of the variation arises due to purely radial modes of oscillation, observations suggest that both non-radial modes and multi-mode oscillations are present, showing that even these 'classical' examples of stellar oscillations can exhibit variation and complexity.

The observation of these stellar oscillations has given rise to a new field of astrophysics – asteroseismology, the study of vibrations in stars. As the observed frequencies of oscillation correspond to the star's normal modes, which depend on the properties of the star not only at the surface, but throughout its body, observations of

the stellar vibrations can be used to investigate the interior of the star. This was first applied to the sun, as helioseismology, where the observed oscillation frequencies were used to probe the solar interior and build up a model of the sun's internal structure (Deubner & Gough, 1984).

This process of analysing observed frequencies, and particularly the frequency spacing, has been used more generally to investigate structure of other stars. Oscillations, including non-radial modes, have been discussed for decades (see Cox (1976) for an early review). Increasingly precise observations of stars providing more and more information, combined with modern stellar models (Paxton et al. (2011); Paxton et al. (2013); Paxton et al. (2015); Paxton et al. (2018); Paxton et al. (2019)) have led to great advancements in asteroseismology, as both classical pulsations and solar-like oscillations have now been detected in many stars (Chaplin & Miglio (2013); see Cunha et al. (2007) and Di Mauro (2017) for further reviews).

Asteroseismology is not the only field to emerge recently – with the Nobel prize-winning discovery of the first confirmed exoplanet, Pegasi 51 b, in 1995 (Mayor & Queloz, 1995) the study of extrasolar planets exploded onto the scene. Despite 51 Peg b being discovered via the radial velocity method, the advent of space-based photometric telescopes such as CoRoT and Kepler (Borucki et al. (2011); Coughlin et al. (2016)) has led to thousands of transiting planets being detected, such that this is the detection method for the majority of confirmed exoplanets currently known.

With both the RV and transit detection methods preferentially selecting close-in, massive planets many 'Hot Jupiters' have been detected – massive planets, resembling Jupiter, but orbiting very close to their host star with orbital periods of only a few days – which are vastly different to what might have been expected based purely on observations of our own solar system. Approximately 1 in 100 solar-type stars are thought to host such a planet (Howard et al. (2012); Wright et al. (2012)), making them fairly common. Given their proximity and substantial mass, Hot Jupiters have a significant gravitational interaction with their host stars, and provide an external perturbation which can induce oscillations, in contrast to the oscillations excited by the internal mechanisms mentioned above.

Such tidal interaction had been studied long before any extrasolar planets were discovered (Darwin, 1879), and much effort has gone into investigating how tidal interactions can lead to changes in an object's orbit, such as tidal friction leading to orbital decay (Goldreich & Nicholson (1989); Lai (1997); Willems et al. (2003); Weinberg et al. (2012)), or causing the rotation of periastron in eccentric orbits (Quataert et al. (1996); Smeyers et al. (1998); Willems (2003)).

This orbital evolution occurs on very long timescales, but more immediate evidence for tidal oscillations has been observed. The first photometric tidal oscillations discovered with Kepler were found in HAT-P-7 b, with an amplitude of $\sim 37$ ppm, for a Hot Jupiter on a 2.2 day circular orbit (Welsh et al., 2010). Similar observations have also been made for other systems, such as CoRoT-3 b (Mazeh & Faigler, 2010) and KOI-13 (Mislis & Hodgkin (2012); Mazeh et al. (2012)).

For perturbers with significantly elliptical orbits, a different phenomenon has been observed, that of so-called 'heartbeat stars'. The strength of the tidal interaction depends strongly on the distance between the objects (it goes as $D^{-3}$, where $D$ is the distance between the centres of the interacting objects), and is therefore much stronger at periastron than anywhere else in the orbit. The perturber therefore effectively 'strikes' the star once per orbit as it goes through periastron, causing the star to oscillate in response, and relax over the course of the orbit, before being struck again when the perturber next passes through periastron. One example is the eccentric binary system KOI-54, which shows a very rich array of oscillations, with more than 30 oscillation frequencies being clearly observed (Welsh et al., 2011).

It should also be possible to directly observe the tidal oscillations spectroscopically – the motion of the surface will result in a change in the observed wavelength of light through the Doppler effect, essentially a RV signal. This signal could be mistakenly attributed to a slightly eccentric orbit (Arras et al., 2012). For example, WASP-12 b was originally thought to be a Hot Jupiter on a slightly eccentric orbit (Triaud et al., 2010), but Arras et al. (2012) and Maciejewski et al. (2020b) suggest that the RV signal is more likely the result of a planet on a circular orbit causing a tidal oscillation.

Understanding the cause of these oscillations has been the topic of some interest, with heartbeat stars and eccentric orbits being looked into by many. Modelling of these systems has been done with varying degrees of complexity, from the simplest equilibrium tide approximation to those including some non-adiabatic effects (Burkart et al., 2012). Both the photometric variability (Fuller, 2017) and RV signal have been considered (Willems & Aerts (2002); Penoyre & Stone (2019)). For this case, the star is forced at an infinite number of frequencies, at multiples of the orbital frequency (though practically this infinite series is truncated after a finite number of terms, as the forcing amplitude becomes negligible (Willems, 2003)), and these are often considered to be forcing the normal modes of the star, such that a mode which has a frequency close to a multiple of the orbital frequency will be greatly excited.

Alternatively, and particularly for a circular orbit where the star is forced only at one frequency, the stellar response can be calculated inhomogeneously – that is, the

calculation is direct, rather than going via the stellar eigenfunctions. This calculation has been done for both massive stars (Savonije & Papaloizou, 1983) and solar-mass stars (Terquem et al., 1998), where the stellar oscillation equations have been solved to map the response throughout the star. Although both Savonije & Papaloizou (1983) and Terquem et al. (1998) were focussed on the orbital evolution resulting from the dissipation of the tidal oscillations, which primarily occurs within the body of the star, it was noted that behaviour at the very surface of the star can become highly non-adiabatic, and can diverge significantly from the equilibrium tide case.

For the direct observation of tidal oscillations, as stars are opaque, the surface behaviour is the only thing that really matters. The conversion from the calculated surface behaviour into an observable prediction was initially set out by Dziembowski (1977), where both the photometric and RV variation are considered, in the general context of non-radial stellar oscillations. This has been applied to oscillations in pulsating white dwarfs, known as ZZ Ceti stars, to make predictions for both the brightness and colour variations which might be observable (Robinson et al. (1982); Brickhill (1992)). Applying this to planetary systems has given predictions for the photometric variation from Pfahl et al. (2008), who use a non-adiabatic solution to the oscillation equations to make the predictions, though they do draw attention to some modelling difficulties at the stellar surface. The simpler equilibrium tide has been used by Arras et al. (2012) to make predictions for the RV signals which would arise from a close-in planetary companion, and they predict that some systems would produce a RV variation well above the detectable limit (and which might be mistaken as arising due to non-zero eccentricity, as previously mentioned).

Whilst it is all well and good calculating these signals, it might be asked that, as the tidal response is essentially a second order effect, wouldn't it be easier to just stick with the standard RV and transit detection methods? Although that is certainly true for many systems we might observe, both methods have their drawbacks, particularly with respect to constraining the properties of the planet once it has been found. In the case of the transit method, only a planetary radius can be determined, the mass is not actually constrained – therefore knowledge of the average density of the planet, and thus investigation into its internal structure, is limited. The RV method is not able to measure the mass directly either, as the observed signal varies as $m_{\rm P}\sin(i)$ (where $m_{\rm P}$ is the planetary mass, and $i$ is the orbital inclination of the system). Investigation into tidal oscillations can help with this, as it can provide another way to observe the planet, and could provide mass estimates for planets either directly (for a transiting

system) or by breaking the mass-inclination degeneracy (for RV detections), as the tidal signal has a different dependence on inclination.

In general, the better we are able to define a planet's basic properties, the better we are able to test theories regarding its structure, formation and evolution, and the better we will be able to use further observations to learn more about the planet being observed (Beichman et al., 2014). Having a method to determine planetary masses, or to be used as a check against masses which have already been determined (by, for instance, using both the transit and RV methods together) can increase our confidence in the constraints placed upon the basic properties of the planet, and enables us to better examine a whole range of questions related to exoplanets, across their whole life cycle.

Beyond this, tidal oscillations could also be used to detect planets. This could be indirectly, by helping to clean up observations such that the signal arising due to a known planet can be more completely removed, reducing the noise which might inhibit further planetary detections in the same system. It is also possible that tidal oscillations could lead to directly detecting new planets, as the photometric variation of the star is present for non-transiting planets – a planet which misses transit by a few degrees would have a tidal photometric signal comparable to that of a transiting planet, and could potentially be detected through this.

If the planet is already a completely known entity, investigations could be focussed upon the star instead – a well-defined perturbation would enable the stellar structure to be investigated in a manner similar to standard asteroseismology, where the oscillations are used to probe deeper into the star than we can see directly. This could be used to test and improve modelling of the region close to the stellar surface where non-adiabatic effects become prominent, and perturbations to the convective flux may be significant (Savonije & Papaloizou (1983); Pfahl et al. (2008)).

Bearing all of that in mind, this thesis will essentially seek to address the two questions which most often come up as I explain my work to friends and family. The first question is my explanation of the core question I am addressing in my research: "How do planets make stars wobble?" The second question to be addressed is often given after I have explained what I study, and is along the lines of: "Why does this matter?", or, more brutally: "What's the point?" The method used to address the first question will be set out in chapter 2, which delves into the details of the Henyey method (Henyey et al., 1964) and how it is applied to solve the non-adiabatic stellar oscillation equations, whilst addressing some particular practicalities with the numerics. The solution is then explored in chapter 3, where the stellar response to the

tidal perturbation is discussed throughout the star, and particular attention is paid to the surface region. How this might be observed is explored in chapter 4, where the surface response is converted into predictions for observable signals for both the spectroscopic and photometric signals, and the second question may be touched upon (depending on what you count as being a worthwhile reason for going to all of this trouble). The thesis is then concluded in chapter 5, where the salient points of this work are highlighted.

Before diving straight in, the remainder of this introduction sets out a more algebraic account of the fundamentals upon which this research is built, first with a general description of stellar oscillations in section 1.1, then with an examination of the tidal perturbation and equilibrium tide approximation in sections 1.2 and 1.3, and finally a discussion of the most successful exoplanet detection techniques in section 1.4.

## 1.1 Introduction to stellar oscillations

An oscillation occurs when an element is displaced from a location at which it is in equilibrium, and is acted upon by a restoring force. For a pendulum this restoring force is due to gravity, for a vibrating string it is tension. In the case of stellar oscillations, there are two main modes of oscillation: p-modes and g-modes. The restoring force for the p-modes is due to pressure gradients, hence the name, and are acoustic oscillations which propagate at the speed of sound. G-modes are also aptly named, as the restoring force in this case is gravity, through buoyancy. As this work generally concerns g-modes, as they have longer periods (which can be comparable to the orbital periods of close-in planets), we now set out a rudimentary mathematical description of this behaviour.

Imagine a blob of fluid, existing within a star whose structure is in hydrostatic equilibrium. Imagine the blob is slowly displaced by some small distance, $\delta r$, such that pressure equilibrium is maintained, but without heat transfer occurring between the blob and its surroundings (that is, the process is adiabatic). The change in pressure experienced by the blob is

$$\delta p = p(r+\delta r) - p(r) = \frac{\mathrm{d}p}{\mathrm{d}r}\delta r. \tag{1.1}$$

The blob changes density to maintain this pressure equilibrium, but it does so adiabatically, giving the change in density of the blob as

$$\delta \rho = \left(\frac{\partial \rho}{\partial p}\right)_s \delta p. \tag{1.2}$$

where the subscript $s$ denotes that the gradient is at constant entropy (and therefore is adiabatic). This may give rise to a difference in density between the blob and its surroundings, given by

$$\Delta\rho = \delta\rho - \frac{\mathrm{d}\rho}{\mathrm{d}r}\delta r = \frac{\mathrm{d}p}{\mathrm{d}r}\left(\left(\frac{\partial\rho}{\partial p}\right)_s - \frac{\mathrm{d}\rho}{\mathrm{d}p}\right)\delta r \tag{1.3}$$

To study the oscillatory motion we need to quantify the restoring force, which is due to buoyancy. This can be derived by considering the fluid element to be cubic in shape, and considering the forces acting upon it. The net force acting on the cube in the radial direction will be the sum of the gravitational force and the pressure forces acting on its lower and upper faces, giving the total force as

$$\mathrm{d}F = -g\,\mathrm{d}m + p(r)\mathrm{d}A - p(r+h)\mathrm{d}A \tag{1.4}$$

where $g$ is the magnitude of the gravitational acceleration, $\mathrm{d}m$ is the mass of the fluid element, and $\mathrm{d}A$ is the area of the upper and lower faces, which are at $r$ and $r+h$, respectively. Simplifying this equation, and converting the force into the mass element, $\mathrm{d}m$, times the acceleration in the radial direction, $\delta\ddot{r}$, gives

$$\delta\ddot{r}\,\mathrm{d}m = -g\,\mathrm{d}m - \frac{\mathrm{d}p}{\mathrm{d}r}h\,\mathrm{d}A. \tag{1.5}$$

As $h\,\mathrm{d}A$ is the volume of the fluid element, its density can be expressed as $\rho = \mathrm{d}m/(h\,\mathrm{d}A)$. Using the fact that the surrounding material is in hydrostatic equilibrium gives

$$\rho\,\delta\ddot{r} = -\rho\,g + \rho_0\,g \tag{1.6}$$

where $\rho_0$ is the density of the surroundings. Assuming that the difference between $\rho$ and $\rho_0$ is small, we get

$$\delta\ddot{r} = -\left(\frac{\rho-\rho_0}{\rho}\right) \approx -\frac{\Delta\rho}{\rho_0}g. \tag{1.7}$$

Combining this with equation 1.3, and assuming an oscillatory solution, gives an expression for the oscillation of the blob that we displaced as

$$-\omega^2\,\delta r = -\frac{g}{\rho}\frac{\mathrm{d}p}{\mathrm{d}r}\left(\left(\frac{\partial\rho}{\partial p}\right)_s - \frac{\mathrm{d}\rho}{\mathrm{d}p}\right)\delta r. \tag{1.8}$$

From this, we can then isolate the square of the angular frequency at which this blob will oscillate as

$$\omega^2 = \frac{g}{\rho}\frac{\mathrm{d}p}{\mathrm{d}r}\left(\left(\frac{\partial\rho}{\partial p}\right)_s - \frac{\mathrm{d}\rho}{\mathrm{d}p}\right). \tag{1.9}$$

This is a simplistic derivation of the Brunt–Väisälä frequency, which will be used throughout this work, denoted as $N$. There are many different ways to express this frequency, and a different one will be used later on, but this approach is a helpful one to gain insight into the underlying physics of the process.

It is particularly helpful to notice the relationship between the squared Brunt–Väisälä frequency and the gradient of the density difference (i.e. $\Delta\rho/\delta r$) – if the latter is positive, the former will be too. This then corresponds to a real value for $\omega$, which gives rise to an oscillation. This will occur if, when the blob is displaced upwards, it is surrounded by material which is less dense than itself. This will occur in regions which are stratified, and the star's energy flux is transported by radiation.

The other situation, when a displacement upwards results in the blob being less dense than its surroundings, will give rise to the blob moving further away from its equilibrium position. This region of the star is therefore unstable to perturbations, and will therefore be expected to be a convective region of the star. The square of the Brunt–Väisälä frequency in this region is negative, and therefore the frequency is imaginary. This imaginary frequency means that the waves will be evanescent in convective regions, whereas they are oscillatory in radiative regions. We therefore expect that g-modes will largely occur in radiative regions of the star. In low mass stars they will therefore be largely confined to the stellar core by the thick convection zone, though some amplitude will still make it to the stellar surface, where it can propagate in the thin radiative skin.

So far, we have only asserted that the blob we are considering has somehow been displaced from its equilibrium position by some kind of one-off perturbation, on a gas giant such as Jupiter it could even be caused by 'rock storms' (Markham & Stevenson, 2018). In cases such as these, the perturbation is likely to be short–lived, and therefore the star will oscillate at its resonant frequencies, similar to striking a bell. If the perturbation is persistent, the system will act as a damped, driven oscillator, reaching a steady state where both the amplitude and frequency of the response are determined by the perturbation. Such a perturbation might be provided by a nearby massive planet, as will be explored below.

## 1.2 Tidal perturbation

As the orbit of a planet around a star is expected to evolve on a timescale much longer than the orbital period, the tidal potential considered here is the lowest order time–varying potential which is not constant across the star. We neglect any constant

terms, as although they may introduce a slight constant deformation to the star, they will not cause an oscillatory response. To find this we evaluate the potential in the frame of the star, accounting for the force acting at the stellar centre of mass (the indirect term) in that frame, as

$$\Phi_{\rm P} = \Phi + \frac{Gm_{\rm p}}{D^3}\boldsymbol{D}\cdot\boldsymbol{r}, \tag{1.10}$$

where $\Phi_{\rm P}$ is the tidal potential, $\Phi$ is the gravitational potential due to the perturber, $G$ is the gravitational constant, $m_{\rm p}$ is the mass of the perturbing body, $\boldsymbol{D}$ is the vector from the centre of the star to the perturber, approximated as a point mass, and $\boldsymbol{r}$ is the position vector from the centre of the star to the point at which the potential is calculated.

This can be expanded in terms of $r/D$, which is a small quantity, with $D = |\mathbf{D}|$, to give

$$\Phi_{\rm P} = -\frac{Gm_{\rm p}}{D}\left[1 + \left(\frac{r}{D}\right)^2\left(\frac{3}{2}(\hat{\boldsymbol{D}}\cdot\hat{\boldsymbol{r}})^2 - \frac{1}{2}\right)\right] + O\left(\frac{r^3}{D^3}\right) \tag{1.11}$$

where the hats denote unit vectors. We then use the fact that $\hat{\boldsymbol{D}}\cdot\hat{\boldsymbol{r}} = [\cos(\omega t)\hat{\boldsymbol{x}} + \sin(\omega t)\hat{\boldsymbol{y}}]\cdot[\sin(\theta)\cos(\phi)\hat{\boldsymbol{x}} + \sin(\theta)\sin(\phi)\hat{\boldsymbol{y}} + \cos(\theta)\hat{\boldsymbol{z}}]$, where we adopt a coordinate system with origin at the stellar centre of mass and $(x,y)$ plane coinciding with that of the orbit, and $\omega$ being the angular frequency of the orbit. The unit vectors in the coordinate directions are $\hat{\boldsymbol{x}}$, $\hat{\boldsymbol{y}}$, $\hat{\boldsymbol{z}}$. The spherical coordinates, $(r,\theta,\phi)$, have the orbital angular momentum vector aligned with $\theta = 0$, and $\hat{\boldsymbol{x}}$ is aligned with $\hat{\boldsymbol{r}}$ for $\theta = \pi/2$ and $\phi = 0$. Later in the thesis, when other coordinate systems are introduced, this will be referred to as the star's coordinate system, and may have a subscript asterisk to signify that. The associated unit vectors are $\hat{\boldsymbol{r}}$, $\hat{\boldsymbol{\theta}}$ and $\hat{\boldsymbol{\phi}}$, respectively. Removing terms with non–zero time average from equation 1.11 (and therefore keeping only the oscillatory terms), we arrive at the expression

$$\Phi_{\rm P} \simeq -\frac{Gm_{\rm p}}{4D}\left[\left(\frac{r}{D}\right)^2 3\sin^2(\theta)\cos\left[2(\omega t - \phi)\right]\right]. \tag{1.12}$$

As $3\sin^2(\theta) = P_2^{|2|}(\cos\theta)$ (the associated Legendre polynomial), $\Phi_P$ can be written in terms of a spherical harmonic as

$$\Phi_{\rm P} \simeq \Re\left(-\frac{GM_{\rm p}}{4D^3}r^2 4\sqrt{\frac{2\pi}{15}}Y_2^{-2}(\theta,\phi)\mathrm{e}^{2\mathrm{i}\omega t}\right) \tag{1.13}$$

where $Y_2^{-2}(\theta,\phi) = \frac{1}{4}\sqrt{\frac{15}{2\pi}}\sin^2\theta\mathrm{e}^{-2\mathrm{i}\phi}$, and $\Re$ denotes the taking of the real part. Therefore the properties of the spherical harmonic apply to the tidal perturbation as well.

Because the tidal perturbation is the only source of time and angular dependence (as the equilibrium model is taken to be spherically symmetric and static) in the system of linear equations, any perturbed quantity in equations (2.16) to (2.19), $q'$, can be expressed in the form

$$q'(r,\theta,\phi,t) = \Re\left(q'(r) 3\sin^2\theta \mathrm{e}^{2\mathrm{i}(\omega t-\phi)}\right) \tag{1.14}$$

where $q'(r)$ may itself be complex. For simplicity, many variables discussed throughout this work will take the $3\sin^2\theta\mathrm{e}^{2\mathrm{i}(\omega t-\phi)}$ factor as read, and only discuss $q'(r)$.

To give a sense for the perturbation, it is useful to consider how an equipotential of the gravitational field is affected – we expect two bulges at the equator of the star (one under the planet, and one on the far side) whilst the poles of the star will be largely unaffected. Unsurprisingly, the size of the bulge depends linearly on the mass of the planet, but it also depends on the star – the larger the star's radius the stronger the tidal perturbation will be at the surface, as it scales as $r^2$. Finally, the perturbation also depends on the arrangement of the system as a whole, with the $D^{-3}$ dependence making the perturbation very sensitive to changes in the orbital separation of the bodies.

## 1.3 The equilibrium tide and the low frequency limit in the adiabatic region

A very simple way to apply this tidal perturbation is obviously a helpful starting point, which provides insight into the response of the star – the equilibrium tide approximation is exactly that. This section briefly covers the equilibrium tide and its prediction for the radial displacement, so that the equilibrium tide and the non–adiabatic dynamical tide, which is calculated and discussed later in this work, can be compared. Discussion of the horizontal displacement in the equilibrium tide is given in appendix A.

The equilibrium tide is calculated in the low–frequency limit, such that $\omega \approx 0$, in which the equation of motion reduces to the condition for hydrostatic equilibrium, which, when linearised, takes the form:

$$0 = -\nabla p' - \rho_0 \nabla \Phi_\mathrm{P} - \rho' \nabla \Phi_0, \tag{1.15}$$

where $\Phi_\mathrm{P}(r) = -Gm_\mathrm{P} r^2/(4D^3)$ is the radial part of the tidal potential obtained after factoring out the angular dependent factor $Y_2^{-2}(\theta,\phi)\mathrm{e}^{2\mathrm{i}\omega t}$ (see section 1.2). The same factor is also removed from the perturbation response.

Here $\Phi_0$ is the equilibrium gravitational potential, $p'$ is the Eulerian perturbation to the pressure, $\rho_0$ is the equilibrium density, and $\rho'$ is the perturbation to the density. We have used the Cowling approximation, which assumes that the change in the star's self-gravity is small, such that the only change in the gravitational potential is that of the tidal potential. This approximation is expected to hold well as the stellar core is far more dense than the stellar envelope, and the displacement there is expected to be small.

We assume that the background star is in hydrostatic equilibrium, giving:

$$\frac{dp_0}{dr} = -g\rho_0 \tag{1.16}$$

where $g \equiv d\Phi_0/dr$ is the magnitude of the gravitational acceleration.

The horizontal component of equation (1.15) yields:

$$p' = -\rho_0 \Phi_{\rm P}, \tag{1.17}$$

which can be substituted into the radial component of equation (1.15) giving an expression for $\rho'$ as:

$$\rho' = \frac{d\rho_0}{dr}\frac{\Phi_{\rm P}}{g}. \tag{1.18}$$

Similarly (1.17) can be written as:

$$p' = \frac{dp_0}{dr}\frac{\Phi_{\rm P}}{g}. \tag{1.19}$$

Then from (1.18 ) and (1.19) we obtain:

$$\Delta p - \frac{\Gamma_1 p_0}{\rho_0}\Delta\rho = \left(\xi_r + \frac{\Phi_{\rm P}}{g}\right)\left(\frac{dp_0}{dr} - \frac{\Gamma_1 p_0}{\rho_0}\frac{d\rho_0}{dr}\right). \tag{1.20}$$

where $\Gamma_1 = \left(\frac{\partial \ln p}{\partial \ln \rho}\right)_s$ is the first adiabatic exponent (Chandrasekhar, 1939) and $\Delta q$ gives the Lagrangian perturbation to some variable, $q$, such that $\Delta q = q' + \xi_r \frac{\partial q_0}{\partial r}$. From this we can conclude that for adiabatic perturbations at a location for which $N^2 \neq 0$, we have:

$$\xi_r = -\frac{\Phi_{\rm P}}{g}, \tag{1.21}$$

where $\xi_r$ is the radial displacement from the equilibrium position. This is the standard form of the radial displacement for the equilibrium tide. We remark that taken together with equations (1.18) and (1.19), this implies that the Lagrangian perturbations to the pressure and density, $\Delta p$ and $\Delta\rho$, are both zero. This is consistent

with these quantities being related by a condition for adiabatic change. But note that other relations between these quantities, such as may occur in a non-adiabatic zone, may lead to an inconsistency, with the consequence that hydrostatic equilibrium may not be assumed and the standard equilibrium tide discussed above will not be applicable. Further details can be found in appendix A and Bunting et al. (2019).

## 1.4 Introduction to exoplanet detection methods

For centuries only a small number of planets have been visible – those within our own solar system. With such a small sample size, constraining the formation and evolution mechanisms for planetary systems is very difficult, although many different theories were proposed (Winn & Fabrycky, 2015).

Since the first exoplanet orbiting a main-sequence star was confirmed 25 years ago (Mayor & Queloz, 1995) many more have been discovered (note that the very first exoplanets discovered were orbiting pulsars, see Wolszczan & Frail (1992) and Thorsett et al. (1993)). A large number of these discoveries have been of systems which differ greatly from those which might have naïvely been predicted by extrapolating from the solar system.

There are many different techniques used to detect these planets, including direct imaging and microlensing, but the two most successful methods so far have been the radial velocity method (which led to the discovery of the first exoplanet, 51 Pegasi b by Mayor & Queloz (1995)) and the transit method (in no small part due to the success of the Kepler satellite (Coughlin et al., 2016)). Here we set out the basics of these two methods, and discuss the selection effects at work.

### 1.4.1 Radial velocity method

The radial velocity detection method depends on spectroscopic variation of the light from a star, as a result of the motion of the star caused by the presence of an orbiting planet. This arises from the fact that a planet in orbit around a star will move the centre of mass of the orbital system away from the star's centre. The star will also be orbiting this common centre of mass, and will therefore be periodically moving towards, and then away from, an observer (unless the system is viewed from 'above'). To describe this system, we introduce an inertial coordinate frame, centred on the common centre of mass of the system, in which the position of the star and planet are given by $\boldsymbol{r}_*$ and $\boldsymbol{r}_\mathrm{p}$, respectively. It is helpful to introduce the vector from the centre

of the star to the centre of the planet as

$$\boldsymbol{D} = \boldsymbol{r}_\mathrm{p} - \boldsymbol{r}_* \tag{1.22}$$

which can be combined with the fact that the origin of this coordinate system is at the system's centre of mass, expressed as

$$m_* \boldsymbol{r}_* + m_\mathrm{p} \boldsymbol{r}_\mathrm{p} = 0, \tag{1.23}$$

where $m_*$ is the stellar mass, and $m_\mathrm{p}$ is the planetary mass, to give

$$\boldsymbol{r}_* = -\frac{m_\mathrm{p}}{m_* + m_\mathrm{p}} \boldsymbol{D}. \tag{1.24}$$

For simplicity, we now take the case of a circular orbit in the x-y plane, giving

$$\boldsymbol{D} = \cos \omega t \hat{\boldsymbol{x}} + \sin \omega t \hat{\boldsymbol{y}} = D \hat{\boldsymbol{r}} \tag{1.25}$$

where the hats denote unit vectors, $D = |\boldsymbol{D}|$ and $\omega$ is the orbital angular frequency. To find the velocity of the star, we take the time derivative of its location vector, giving

$$\dot{\boldsymbol{r}}_* = -\frac{m_\mathrm{p}}{m_* + m_\mathrm{p}} \dot{\boldsymbol{D}} = -\frac{m_\mathrm{p}}{m_* + m_\mathrm{p}} \omega D(-\sin \omega t \hat{\boldsymbol{x}} + \cos \omega t \hat{\boldsymbol{y}}). \tag{1.26}$$

This gives a constant magnitude for the velocity of the star, but in any given direction the velocity will vary sinusoidally (assuming a circular orbit), with angular frequency $\omega$. Using the expression for centripetal acceleration, we can relate the angular frequency (and therefore the orbital period) to the orbital separation, as

$$\frac{G m_* m_\mathrm{p}}{D^2} = m_* \omega^2 |\boldsymbol{r}_*| = m_* \omega^2 \frac{D m_\mathrm{p}}{m_* + m_\mathrm{p}}, \tag{1.27}$$

where $G$ is the gravitational constant. Using $\omega = 2\pi/P$, where $P$ is the orbital period of the planet, enables us to reexpress the magnitude of the star's velocity as

$$|\dot{\boldsymbol{r}}_*| = m_\mathrm{p} \left( \frac{2\pi G}{(m_\mathrm{p} + m_*)^2 P} \right)^{\frac{1}{3}} \tag{1.28}$$

This gives the magnitude of the velocity of the star, but the extent to which this results in a Doppler shift measured by an observer depends on the orientation of the system – if observed face on there will be no motion either towards or away from the observer, and if edge on the observer will detect the full orbital velocity. The observed amplitude of the radial velocity variations depend on the magnitude of the velocity projected along the observer's line of sight. The inclination of the system, $i$, is the

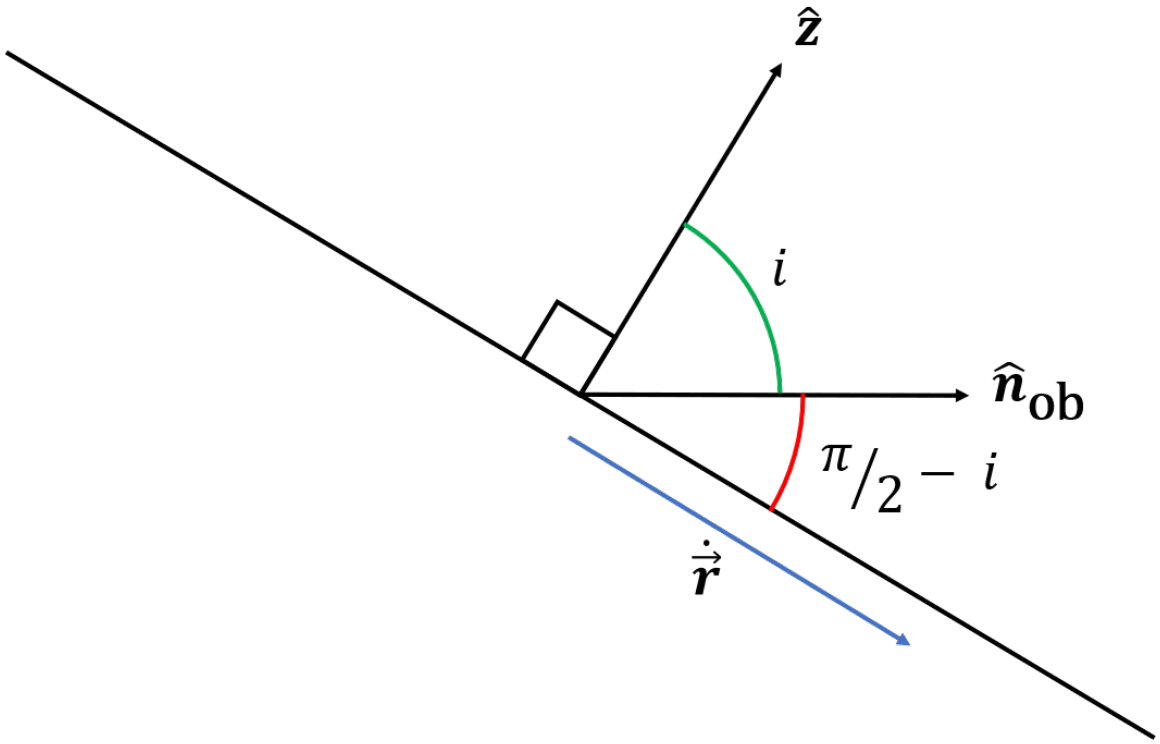


Figure 1.1: The radial velocity of a system depends upon the inclination of the orbit with respect to the observer, $i$, equal to $\cos^{-1}(\hat{\boldsymbol{z}} \cdot \hat{\boldsymbol{n}}_{\rm ob})$, where $\hat{\boldsymbol{z}}$ is the normal to the orbital plane. The amplitude of the radial velocity variation is given by the maximum value of the velocity, $\dot{\boldsymbol{r}}_*$, projected along the direction to the observer, $\hat{\boldsymbol{n}}_{\rm ob}$. This is given by $\dot{\boldsymbol{r}}_* \cdot \hat{\boldsymbol{n}}_{\rm ob} = |\dot{\boldsymbol{r}}_*| \cos((\pi/2) - i) = |\dot{\boldsymbol{r}}_*| \sin(i)$.

angle between the orbital angular momentum vector (parallel to $\hat{\boldsymbol{z}}$ in this case) and the vector towards the observer, $\hat{\boldsymbol{n}}_{\rm ob}$, and is equal to $\cos^{-1}(\hat{\boldsymbol{z}} \cdot \hat{\boldsymbol{n}}_{\rm ob})$ (see the diagram in figure 1.1). The amplitude of the radial velocity variation can then be expressed as

$$K_{\rm orb} = m_{\rm p} \sin(i) \left( \frac{2\pi G}{(m_{\rm p} + m_*)^2 P} \right)^{\frac{1}{3}}. \tag{1.29}$$

With this expression, we can determine some of the selection effects present in radial velocity exoplanet detections, and also spot where it falls short. In the case that $m_{\rm p} \ll m_*$, as is generally expected, $K_{\rm orb} \propto m_{\rm p}$ – a more massive planet results in a correspondingly larger signal. However, the mass cannot be directly measured, as it is degenerate with the inclination, therefore the measured mass gives a minimum possible value, until further observations can disentangle $m_{\rm p}$ and $i$ from each other.

The mass of the star (more precisely, the total mass of the system, though this is approximately equal to the stellar mass) has a slightly weaker effect on the radial velocity amplitude, as $K_{\rm orb} \propto m_*^{-\frac{2}{3}}$. A lower mass star makes detection slightly easier

as it is easier for the planet's mass to move the star. This is slightly counteracted by the fact that the lower gravitational pull from the star will result in a slower orbit. The dependence of the probability of detection on the stellar mass is not as simple as this, however, as changing the stellar mass can significantly change the brightness and variability of the host star. Additionally, stellar properties, such as rotational period and the structure of absorption lines, vary along the main sequence and can significantly impact the ability to detect radial velocity signals even for stars of equal mass.

The amplitude of the signal is also related to the period of the orbit: $K_{\text{orb}} \propto P^{-\frac{1}{3}}$. Although this effect is weaker still than the two effects mentioned above, shorter period orbits lead to larger signals. Two contrasting effects give rise to this: shorter periods mean that the star completes one orbit in a shorter time, although the 'track' has also become shorter as the closer orbit means that the centre of the star is displaced from the system's centre of mass by a shorter distance. Overall, the track shrinks slightly less than the period shrinks, resulting in an overall increase in the star's speed. Alternatively, this can be understood through the Virial theorem, which relates the orbital velocity to the orbital separation as $v^2 \propto \frac{1}{D}$.

### 1.4.2 Transit method

The transit method of exoplanet detection relies upon the planet causing a periodic change in the brightness of the star. This occurs when the planet passes between the star and the observer, and part of the star's disc is blocked from view. The proportional change in brightness, or the 'transit depth', is equal to the fraction of the stellar disc which is blocked by the planet, giving

$$\frac{\Delta L}{L} = \frac{\pi R_{\text{p}}^2}{\pi R_*^2} = \left(\frac{R_{\text{p}}}{R_*}\right)^2 \tag{1.30}$$

where $R_{\text{p}}$ and $R_*$ and the radii of the planet and star, respectively. For a planet with a radius similar to that of Jupiter orbiting a star of similar size to the sun this transit depth will be around 1 per cent.

In order for this method to work, the system must be arranged in such a way as to enable a transit. A 'perfect' transit will occur if the planet passes in front of the equator of the star, such that the normal to the orbital plane, $\hat{\boldsymbol{z}}$, is perpendicular to the direction towards the observer, $\hat{\boldsymbol{n}}_{\text{ob}}$, which can be expressed as $\hat{\boldsymbol{n}}_{\text{ob}} \cdot \hat{\boldsymbol{z}} = 0$, therefore $\theta = \pi/2$. As the star has non-zero size, there is some leeway – a slightly less than perfect orientation may still result in a transit.

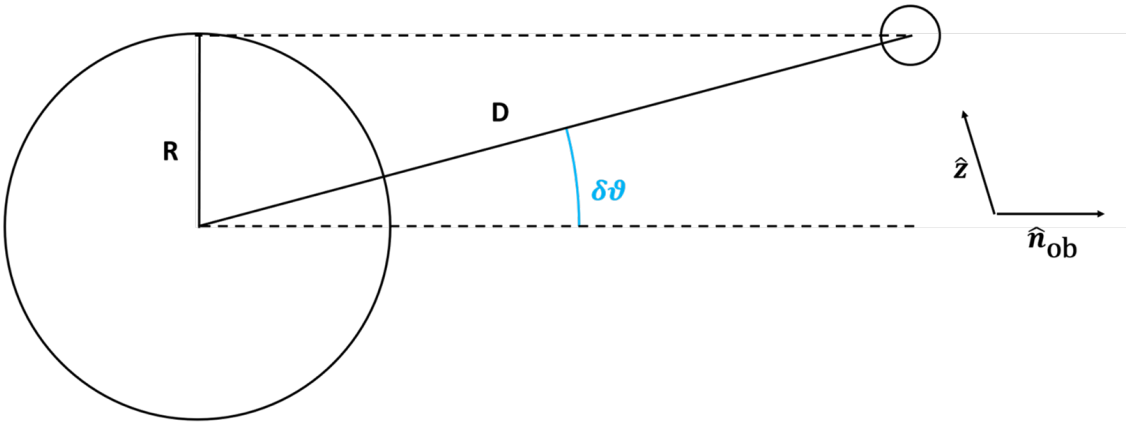


Figure 1.2: The transit method depends upon the planet passing between the observer and the star, such that some of the light from the star is blocked. This will occur if the normal to the plane of the orbit, $\hat{\boldsymbol{z}}$, is perpendicular to the direction towards the observer, $\hat{\boldsymbol{n}}_{\rm ob}$. This may still occur for a slightly tilted orbit, as long as the tilt, $\delta\theta$, is sufficiently small (the tilt is related to the orbital inclination, $i$, by $\delta\theta = \frac{\pi}{2} - i$). This can be quantified as $|D\sin(\delta\theta)| < R_*$, where $R_*$ is the stellar radius and $D$ is the orbital separation at the time of transit (we consider the case of a circular orbit, where $D$ is constant throughout the orbit). As $R \ll D$, this simplifies to $|\delta\theta| < \frac{R}{D}$. This diagram shows the limiting case, where $|\delta\theta|$ is at its maximum value for which a transit still occurs.

Figure 1.2 shows the arrangement for the limiting case, where a transit only just occurs. The inclination can deviate from $\pi/2$ by an amount, $\delta\theta$, such that $|D\sin(\delta\theta)| < R_*$, where $R_*$ is the stellar radius and $D$ is the orbital separation at the time of transit. Throughout this work we consider planets on circular orbits, so we simplify here to the case that $D$ is constant throughout the orbit. As $R \ll D$ this can be approximately expressed as $|\delta\theta| < \frac{R}{D}$.

The probability of a transit occurring in a system can then be calculated by considering the proportion of orientations for which a transit occurs. This is done by integrating over the unit sphere with the condition that $|\theta - \pi/2| < \delta\theta$, giving the probability of a transit as

$$p_{\text{transit}} = \frac{\int_0^{2\pi} \mathrm{d}\phi \int_{\frac{\pi}{2}-\delta\theta}^{\frac{\pi}{2}+\delta\theta} \sin(\theta)\mathrm{d}\theta}{\int_0^{2\pi} \mathrm{d}\phi \int_0^{\pi} \sin(\theta)\mathrm{d}\theta} = \frac{2\pi}{4\pi} \int_{\frac{\pi}{2}-\delta\theta}^{\frac{\pi}{2}+\delta\theta} \sin(\theta)\mathrm{d}\theta \tag{1.31}$$

which is evaluated to give $p_{\text{transit}} = \sin(\delta\theta) \approx R_*/D$ once the small angle approximation is used. Using equation 1.27, we see that $p_{\text{transit}} \propto P^{-\frac{2}{3}}$. Short period planets will therefore be preferentially selected for, even more so than in the radial velocity method. This is compounded by the fact that a shorter period planet is more likely to have multiple transits observed, making detection easier.

Systems with a greater transit depth will also be easier to detect above the background noise. Therefore planets with large radii will be more easily detected. Whilst this may occur due to low mass planets being 'puffed up' to very large radii such as in the Kepler-51 system (Masuda, 2014), it will also result in massive planets being preferentially detected due to their large radii.

Although we have only considered a very simplified view of the transit method, other information about the planet's orbit can also be gleaned from the transit, by looking at the duration of the transit, and the shape of the lightcurve as the transit begins and ends. For a lone transiting planet, however, the mass cannot be determined without either assuming an average density or utilising other techniques.

Overall, massive, close-in planets are the easiest to detect using the two most successful exoplanet detection methods meaning that many so-called 'Hot Jupiters' have been discovered, and providing many examples of systems in which the tidal interaction between a planet and its host star may be significant.

# Chapter 2

# Methods

Before diving into the exciting prospect of new ways to detect exoplanets, we must first spend some time focussing on something potentially less glamorous – setting out exactly what we are investigating in a rigorously defined way, so that we have an understanding of the underlying maths when we do come to apply it to planets.

This chapter is focussed on the problem which we seek to address, and explaining the method used to approach it. First, the derivation of the stellar oscillation equations is briefly outlined in section 2.1, before the numerical method used to solve these equations (originally developed by Henyey et al. (1964)) is explained in section 2.2 and the specifics of applying it to this problem are delved into in section 2.3. For another account of the application of the Henyey method please see Savonije & Papaloizou (1983).

## 2.1 Stellar oscillation equations

Here we set out the skeleton for the derivation of the stellar oscillation equations used in this work, including stating the approximations used along the way. Further details can be found in Unno et al. (1989). The following assumptions are adopted in order to derive a set of governing equations for the forced response problem:

1. Time independence of the background: the equilibrium state of the star changes on a timescale much longer than the period of the oscillations.

2. Spherical symmetry: the equilibrium structure of the star is spherically symmetric, parametrized only as a function of radius. This is assumed to apply after horizontal averaging in convection zones.

3. Non-rotating star: this approximation is valid if the rotational period of the star is much longer than the orbital period of the planet.

4. Cowling approximation: the perturbation to the gravitational potential of the star is neglected, which is justified in the outer region of the star which has low density and in the inner parts of the star where the wavelength of the oscillatory response is small.

5. Small perturbations: the departures from equilibrium are everywhere small such that the linear regime is a valid approximation.

We start from the continuity, momentum, and energy equations together with the expression we used for the heat flux in the form

$$\frac{\partial \rho}{\partial t} + \boldsymbol{\nabla} \cdot (\rho \boldsymbol{u}) = 0, \tag{2.1}$$

$$\rho \left( \frac{\partial}{\partial t} + \boldsymbol{u} \cdot \boldsymbol{\nabla} \right) \boldsymbol{u} = -\boldsymbol{\nabla} p - \rho \boldsymbol{\nabla} \Phi \tag{2.2}$$

$$\rho T \left( \frac{\partial}{\partial t} + \boldsymbol{u} \cdot \boldsymbol{\nabla} \right) s = -\boldsymbol{\nabla} \cdot \boldsymbol{F} \tag{2.3}$$

$$\boldsymbol{F} = -K \boldsymbol{\nabla} T + \boldsymbol{F}_{\mathrm{c}} \tag{2.4}$$

where $\rho$ is the density, $\boldsymbol{u}$ is the vector velocity, $p$ is the pressure, $\Phi$ is the gravitational potential, $T$ is the temperature, $s$ is the specific entropy, $\boldsymbol{F}$ is the total flux, $\boldsymbol{F}_{\mathrm{c}}$ is the convective flux and $K$ is the radiative thermal conductivity.

In this work, we assume that the local convection time scale is much less than the oscillation period (such that many convective turnovers occur over the course of a single oscillation) so that the convective flux can relax to an equilibrium value in regions where we need to take it into account. Assuming a standard form derived from mixing length theory, the expression for the convective flux we adopt is given by:

$$\boldsymbol{F}_{\mathrm{c}} = -\hat{\boldsymbol{n}} \frac{b \rho T v_{\mathrm{c}} l}{1 + c \sigma T^3 (\rho^2 c_p l v_{\mathrm{c}} \kappa)^{-1}} \hat{\boldsymbol{n}} \cdot \boldsymbol{\nabla} s \tag{2.5}$$

where $\sigma$ is the Stefan-Boltzmann constant, $v_{\mathrm{c}}$ is the convective velocity, $\hat{\boldsymbol{n}}$ is the unit vector in the direction opposite to that of gravity, $c_p \equiv T \left( \partial s / \partial T \right)_p$ is the specific heat capacity at constant pressure, $l$ is the mixing length, and $b$ and $c$ are numerical factors which depend on the model of convection being used (see Salaris & Cassisi, 2008, for more details and discussion). Note that in the steady unperturbed state $\hat{\boldsymbol{n}} = \hat{\boldsymbol{r}}$, with the latter pointing in the radial direction.

This is the form of the convective flux as used in Modules for Experiments in Stellar Astrophysics (MESA) (Paxton et al. (2011); Paxton et al. (2013); Paxton et al. (2015); Paxton et al. (2018); Paxton et al. (2019)), the program used to produce the

background stellar models for this work. The MLT approach to convection is discussed further in section 3.1.2. Simplistically, equation 2.5 can be thought of as accounting for the energy flux due to a moving fluid element transporting excess heat. It is expected to travel at speed $v_c$ for a distance $l$ where it then dissipates and deposits its excess heat. The denominator accounts for radiative cooling which will occur as the fluid element travels through regions which are cooler than it is.

Equations (2.1) - (2.5) are linearised, and only first order terms are retained. As the background state is in equilibrium, we set $\boldsymbol{u} = \partial\boldsymbol{\xi}/\partial t$ where $\boldsymbol{\xi}$ is the Lagrangian displacement. This gives us the set of linearised equations:

$$\frac{\partial}{\partial t}\left(\rho' + \boldsymbol{\nabla}\cdot(\rho_0\boldsymbol{\xi})\right) = 0, \tag{2.6}$$

$$\rho_0\frac{\partial^2\boldsymbol{\xi}}{\partial t^2} = -\boldsymbol{\nabla}p' - \rho_0\boldsymbol{\nabla}\Phi_{\rm P} - \rho'\boldsymbol{\nabla}\Phi_0, \tag{2.7}$$

$$\rho_0 T_0\frac{\partial}{\partial t}\left(s' + \boldsymbol{\xi}\cdot\boldsymbol{\nabla}s_0\right) = -\boldsymbol{\nabla}\cdot\boldsymbol{F}', \tag{2.8}$$

$$\boldsymbol{F}' = -K'\boldsymbol{\nabla}T_0 - K_0\boldsymbol{\nabla}T' + \boldsymbol{F}'_{\rm c}, \tag{2.9}$$

$$\frac{K'}{K_0} = 3\frac{T'}{T_0} - \frac{\kappa'}{\kappa_0} - \frac{\rho'}{\rho_0}, \tag{2.10}$$

$$\kappa' = \kappa_\rho\frac{\rho'}{\rho_0} + \kappa_T\frac{T'}{T_0}, \tag{2.11}$$

$$s' = c_p\left(\frac{T'}{T_0} - \nabla_{\rm ad}\frac{p'}{p_0}\right), \tag{2.12}$$

$$\frac{\rho'}{\rho_0} = \frac{1}{\chi_\rho}\left(\frac{p'}{p_0} - \chi_T\frac{T'}{T_0}\right), \tag{2.13}$$

where $q'$ denotes the Eulerian perturbation to the variable $q$, and the subscript 0 refers to the value of the background model of the unperturbed star. We have introduced $\nabla_{\rm ad} \equiv (\partial\ln T/\partial\ln p)_s$, the adiabatic gradient; $\kappa$, the opacity; $\kappa_\rho \equiv (\partial\kappa/\partial\ln\rho)_T$; $\kappa_T \equiv (\partial\kappa/\partial\ln T)_\rho$; $\chi_\rho \equiv (\partial\ln p/\partial\ln\rho)_T$ and $\chi_T \equiv (\partial\ln p/\partial\ln T)_\rho$.

To find the perturbation to the convective flux (further details can be found in chapter 3 and appendix B) we take the unperturbed form to be

$$\boldsymbol{F}_{\rm c} = -\hat{\boldsymbol{r}}A\hat{\boldsymbol{r}}\cdot\boldsymbol{\nabla}s, \tag{2.14}$$

where comparison with (2.5) defines $A$. We expect that the contribution of $\boldsymbol{F}'_{\rm c}$ is small when the response is essentially adiabatic, and only becomes important in a thin layer towards the surface where non-adiabatic effects become significant. Therefore

we make the approximation that $\boldsymbol{F}'_{\rm c}$ is dominated by the gradient of the entropy perturbation.. This leads to a perturbed convective flux of the form

$$\boldsymbol{F}'_{\rm c} = -\hat{\boldsymbol{r}}A\hat{\boldsymbol{r}}\cdot\boldsymbol{\nabla}s' - \boldsymbol{\Delta}\hat{\boldsymbol{n}}_c A\hat{\boldsymbol{r}}\cdot\boldsymbol{\nabla}s \tag{2.15}$$

where $-\boldsymbol{\Delta}\hat{\boldsymbol{n}}_c$ is the change in the direction of convection, which is perpendicular to the radial direction, therefore the first term on the right side gives the radial component, and the second term gives the horizontal components. The assumption that $A$ is taken to be unchanged by the perturbation rests on the assumed dominance of the gradient term, as might be expected for small scale perturbations in a thin layer, such that the length scale over which $s'$ changes is smaller than the scale over which $s_0$ changes. This is found to hold true in the upper convective region, where the gradient of $s'$ with respect to $s_0$ is greater than the proportional perturbations to the other variables, which is expected to be the scale of the perturbation to $A$. Similarly, we therefore expect that the radial component will dominate such that the tangential components may be neglected. Practically, this also enables the perturbation to the convective flux to be explored as simply as possible, and without delving into non-local arguments regarding the full perturbation to the convective velocity, for example. We remark that, as discussed in chapter 3, particularly in section 3.1.2, we have investigated cases where $A$ is allowed to vary, also incorporating the dependence of the convective velocity on the entropy gradient, and do not find qualitative changes of behaviour.

Following these procedures we obtain a set of 15 equations, with the associated 15 variables being: $p', T', \boldsymbol{\xi}, \boldsymbol{F}', \rho', s', K', \kappa$ and $\boldsymbol{F}'_{\rm c}$. We eliminate eleven of these with the aim of obtaining four equations for the four variables which we desire to remain, namely $p', T', \xi_r$ and $F'_r$, where the subscripted $r$ denotes the radial component of the vector quantity.

The equations are all linear and have time–independent coefficients, so we can separate the time dependence from the spatial dependence. As the perturbing potential is proportional to $Y_l^{-m}(\theta,\phi)\mathrm{e}^{\mathrm{i}m\omega t}$, with $l = m = 2$, we look for solutions with the same angular and time dependence. Therefore, with $q'$ representing one of the variables we solve for, we have $\partial q'/\partial t = im\omega q'$, $\partial q'/\partial\phi = -imq'$ and $\nabla^2_\perp q' = -(l(l+1)/r^2)q'$, where $\boldsymbol{\nabla}_\perp = \boldsymbol{\nabla} - \hat{\boldsymbol{r}}\partial/\partial r$, so that $\nabla^2_\perp = \nabla^2 - (1/r^2)\partial/\partial r\left(r^2\partial/\partial r\right)$. Note that the equilibrium variables are purely radial, so $\boldsymbol{\nabla}_\perp q_0 = 0$.

In order to make best use of the properties of spherical harmonics, the equations must be formed in such a way as to ensure that $\boldsymbol{\nabla}_\perp$ only appears as $\nabla^2_\perp$. To do this, the vector equations must be split into their radial and tangential components, and the divergence terms must also be split into the radial and tangential parts.

By eliminating the unwanted unknowns, we are left with the oscillation equations, given in equations (2.16) to (2.19). Further details of this derivation can be found in Appendix B.

For solving these equations numerically, we have converted to dimensionless variables $\tilde{\xi}_r = \xi_r/R$, $\tilde{F}_r = F_r'/F_{r_{\rm BC}}$, $\tilde{p} = p'/p_0$ and $\tilde{T} = T'/T_0$, where $F_{r_{\rm BC}} = F_{r_0}|_{r=R}$. The equations are also converted to a dimensionless form, whilst avoiding any potential singularities, giving

$$\frac{1}{\rho_0 R}\frac{\partial}{\partial r}(r^2\rho_0\tilde{\xi}_r) + \left(\frac{r^2}{\chi_\rho R^2} - \frac{l(l+1)p_0}{m^2\omega^2R^2\rho_0}\right)\tilde{p} - \frac{\chi_T}{\chi_\rho}\frac{r^2}{R^2}\tilde{T} = \frac{l(l+1)}{m^2\omega^2R^2}\Phi_P\,, \quad (2.16)$$

$$i\frac{1}{c_p}\frac{r^2}{R}\frac{ds_0}{dr}\tilde{\xi}_r + \frac{F_{r_{\rm BC}}}{m\omega\rho_0 T_0 c_p R^2}\frac{\partial}{\partial r}\left(r^2\tilde{F}_r\right) - i\nabla_{\rm ad}\frac{r^2}{R^2}\tilde{p} + \left(i\frac{r^2}{R^2} + \frac{l(l+1)K_0}{\rho_0 m\omega c_p R^2}\right)\tilde{T} = 0\,, \quad (2.17)$$

$$\begin{aligned} &-\frac{dr}{dT_0}\frac{F_{r_{\rm BC}}}{K_0}\tilde{F}_r - \frac{dr}{dT_0}T_0\frac{\partial\tilde{T}}{\partial r} + \left[-4 + \frac{\kappa_T}{\kappa_0} - \frac{\chi_T}{\chi_\rho}\left(1+\frac{\kappa_\rho}{\kappa_0}\right)\right]\tilde{T} \\ &\quad + \frac{dr}{dT_0}\frac{dr}{ds_0}\frac{F_{{\rm c},r,0}}{K_0}\frac{d}{dr}(c_p\tilde{T}) + \frac{1}{\chi_\rho}\left(1+\frac{\kappa_\rho}{\kappa_0}\right)\tilde{p} - \frac{dr}{dT_0}\frac{dr}{ds_0}\frac{F_{{\rm c},r,0}}{K_0}\frac{d}{dr}(c_p\nabla_{\rm ad}\tilde{p}) = 0 \end{aligned} \quad (2.18)$$

and

$$-\tilde{\xi}_r + \frac{1}{m^2\omega^2R}\left(\frac{1}{\rho_0}\frac{\partial\left(p_0\tilde{p}\right)}{\partial r} + \frac{d\Phi_0}{dr}\frac{\tilde{p}}{\chi_\rho}\right) - \frac{d\Phi_0}{dr}\frac{1}{m^2\omega^2R}\frac{\chi_T}{\chi_\rho}\tilde{T} = -\frac{1}{m^2\omega^2R}\frac{\partial\Phi_P}{\partial r}\,. \quad (2.19)$$

## 2.2 Explanation of the Henyey method

The equations to be solved are those set out in equations 2.16 to 2.19, which can be solved to give $\tilde{\xi}_r$, $\tilde{F}_r$, $\tilde{p}$ and $\tilde{T}$ all throughout the star. To do this we have used the Henyey method (Henyey et al., 1964), as used by Savonije & Papaloizou (1983). The set of boundary conditions (BCs) for these equations make solving them difficult – two conditions apply at the centre of the star, and two apply at the surface:

$$\xi_r \equiv 0 \text{ at } r = 0 \quad (2.20)$$

$$F_r' \equiv 0 \text{ at } r = 0 \quad (2.21)$$

$$\Delta p \equiv 0 \text{ at } r = R \quad (2.22)$$

$$4\frac{\Delta T}{T_0} - \frac{\Delta F_r}{F_{r_0}} \equiv 0 \text{ at } r = R \quad (2.23)$$

where $\Delta q$ is the Lagrangian derivative of some example variable, $q$. The first two (inner) BCs demand that the oscillations are continuous at the centre, and the latter (outer) BCs demand that the outer layer of the star acts as a free surface, and that the surface emits as a blackbody.

The split BCs make it difficult to work with a solution from one boundary to the other, as the problem is under-constrained until all BCs can be applied. It is this splitting, combined with the potentially highly oscillatory nature of the solutions, which means that other methods, such as the Shooting Method, would be difficult to reliably implement, and therefore we have opted for the Henyey method.

In order to simplify the maths, the stellar oscillation equations are re-cast into vector form, with $\boldsymbol{u} = \left(\tilde{\xi}_r, \tilde{F}_r\right)^T$ and $\boldsymbol{v} = \left(\tilde{p}, \tilde{T}\right)^T$, and are expressed as the finite difference equations

$$\mathbf{A}_{k,k+1}\boldsymbol{u}_k + \mathbf{C}_{k,k+1}\boldsymbol{u}_{k+1} + \mathbf{D}_{k,k+1}\boldsymbol{v}_{k+1} = \boldsymbol{M}_{k,k+1} \tag{2.24}$$

and

$$\mathbf{E}_{k,k+1}\boldsymbol{u}_k + \mathbf{F}_{k,k+1}\boldsymbol{v}_k + \mathbf{H}_{k,k+1}\boldsymbol{v}_{k+1} = \boldsymbol{N}_{k,k+1}, \tag{2.25}$$

where the subscripts $k$ and $k+1$ refer to adjacent cells on the numerical grid upon which the equations are being solved (there are $J$ cells, running from $k=0$ at the centre to $k=J-1$ at the surface of the star). We introduce the matrices $\mathbf{A}$, $\mathbf{C}$, $\mathbf{D}$, $\mathbf{E}$, $\mathbf{F}$ and $\mathbf{H}$, as well as the vectors $\boldsymbol{M}$ and $\boldsymbol{N}$ in order to shorten the expressions. The components of these matrices and vectors are given by the relevant coefficients in equations 2.16 to 2.19. The particular method of discretising the equations is discussed in section 2.3.2. Equations 2.24 and 2.25 are therefore numerical approximations to equations 2.16 and 2.17, and 2.18 and 2.19 respectively, evaluated at cell $k$. Further details can be found in appendix C.

The core of the Henyey method is how it deals with the split boundary conditions. This is done by introducing the following relation:

$$\boldsymbol{u}_k + \boldsymbol{\alpha}_k \boldsymbol{v}_k + \boldsymbol{\gamma}_k = 0, \tag{2.26}$$

where $\boldsymbol{\alpha}_k$ is a matrix, and $\boldsymbol{\gamma}_k$ a vector, which describe the relationship between $\boldsymbol{u}_k$ and $\boldsymbol{v}_k$, and are found over the course of solving the equations by using recurrence relations. The central boundary condition dictates that $\boldsymbol{\alpha}_0 = 0$ and $\boldsymbol{\gamma}_0 = 0$. From this

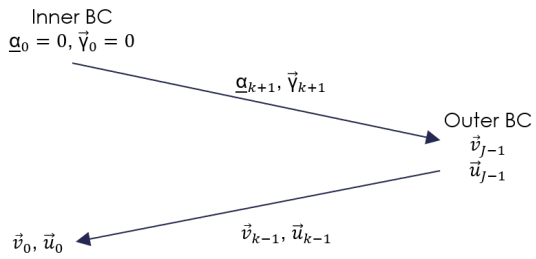


Figure 2.1: A diagrammatic overview of the Henyey method, showing what is being evaluated at each stage of the code. The inner boundary condition (BC) is enforced by setting $\boldsymbol{\alpha}_0 = 0$ and $\boldsymbol{\gamma}_0 = 0$. The arrows represent the two recurrence relations, with the inwards arrow progressively calculating the solution as it works back towards the centre of the grid.

start point, recurrence relations using equations 2.24, 2.25 and 2.26 are used to find expressions for $\boldsymbol{\alpha}_{k+1}$ and $\boldsymbol{\gamma}_{k+1}$.

Once the relations have been found at all points throughout the star, the outer boundary condition is used to find $\boldsymbol{u}_{J-1}$ and $\boldsymbol{v}_{J-1}$ (that is, the surface values), and another recurrence relation is used to find $\boldsymbol{u}_{k-1}$ and $\boldsymbol{v}_{k-1}$ from $\boldsymbol{u}_k$ and $\boldsymbol{v}_k$, until the solution is given throughout the whole star. This process is shown diagrammatically in figure 2.1.

This code was built from scratch, and tested extensively in various situations, particularly assessing the differences between analytically equivalent expressions of the recurrence relations and the differences between different applications of the boundary conditions. The numerical components were also extensively tested, including ensuring the accuracy of matrix and vector manipulation, particularly matrix inversion in the case of small determinants; a structure to deal with the manipulation of complex numbers was built and tested; and a method of interpolation of input data was built, such that the maximum cell size could be precisely controlled and varied across the grid. These were used to solve a variety of different equations, ranging from simple algebraic equations up to the complex differential equations which are used to solve the stellar oscillation equations.

## 2.3 Applying the Henyey method

This section discusses the practical side of the implementation of the stellar oscillation equations, including the problems associated with that, and how they were addressed and overcome.

### 2.3.1 Choice of expressions

In order to enact the Henyey method, the recurrence relations must be accurately expressed. In general there are many different, but analytically equivalent, ways to express the combination of matrices required. A major consideration was to ensure that inverting singular matrices (such as using $\boldsymbol{\alpha}_0^{-1}$) was avoided, which limited the possible sensible range of expressions. Even so, these different expressions were tested to discover which versions were most effective in solving the test equations, and how to express them using the fewest matrix manipulations. For the outgoing recurrence relation, there was only one essential expression, and all the others were found to be exactly analytically equivalent. For the returning recurrence relation, however, two genuinely distinct options are available. Both cases were tested and their accuracy evaluated, and case I was selected to be used. Further details can be found in appendix C.

### 2.3.2 Discretisation and resolution

Converting from equations 2.16 to 2.19, which are continuous, to equations 2.24 and 2.25, which are discrete, necessarily requires some degree of approximation. In order to minimise the error introduced through this, care must be taken in how this discretisation is achieved. Errors can be introduced in two primary ways – through the values of the variables used, or the derivatives of the variables.

To balance the impact of these two possible sources of error, the variables are split into two different types: cell-centre variables, defined at the centre of the cell; and cell-face variables, defined at the outer edge of the cell. $\boldsymbol{u}$ contains cell-face variables, and $\boldsymbol{v}$ contains cell-centre variables, as shown in figure 2.2. This enables the variables and derivatives to be evaluated by using inputs taken from the smallest possible surrounding region.

For example, equation 2.24 involves the derivative of $\boldsymbol{u}$, but not of $\boldsymbol{v}$, so the equation is evaluated at the centre of cell $k+1$. The value of $\boldsymbol{v}$ is given at precisely this location, so no further work is needed there, and the value of $\boldsymbol{u}$ is given by a simple average over $\boldsymbol{u}_k$ and $\boldsymbol{u}_{k+1}$. The derivative of $\boldsymbol{u}$ is found by assuming that the variable in question varies linearly between the two known values.

Equation 2.25, on the other hand, requires the derivative of only $\boldsymbol{v}$. As $\boldsymbol{u}$ is evaluated at the outer face of the cell, that is where we must evaluate both $\boldsymbol{v}$ and its derivative. Using the assumption of linear variation in $\boldsymbol{v}$ between the two cell centres gives both the estimated gradient, and the value of $\boldsymbol{v}$. As the adjacent cells

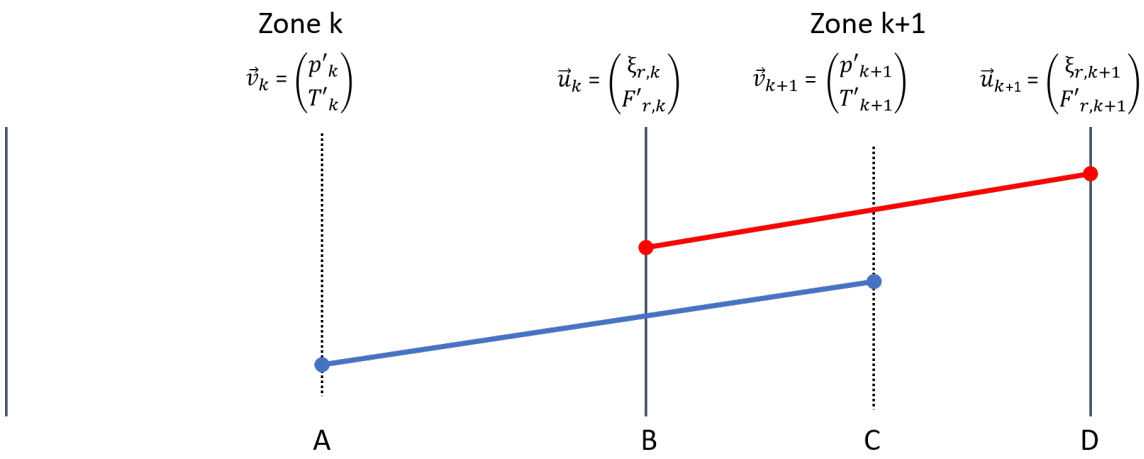


Figure 2.2: This diagram shows the layout of two adjacent cells, showing the staggered variable setup. The cell-face variables, $\boldsymbol{u}$, are defined at locations B and D, for cells $k$ and $k+1$ respectively; the cell-centre variables, $\boldsymbol{v}$, are defined at locations A and C, for $k$ and $k+1$ respectively. Equation 2.24 is evaluated at location C, and the linear interpolation used to evaluate $\boldsymbol{u}$ here is represented by the red line. Equation 2.25 is evaluated at location B, and the linear interpolation used to evaluate $\boldsymbol{v}$ here is represented by the blue line. The difference in size between the adjacent cells makes it clear that location B is not equidistant between A and C, making the interpolation an unevenly weighted average.

may be different sizes the location at which we evaluate this equation will not, in general, be equidistant between the two cell centres. While the error associated with the derivative grows as the ratio of the cell widths deviates from 1, the error in the interpolated value of $\boldsymbol{v}$ actually decreases (as the location at which it must be evaluated is closer to a location at which $v$ has a known value). In order to avoid increasing the error in the derivative, and to reduce the risk of any other numerical artifacts, adjacent cells must be of similar size, such that the proportional difference in adjacent cell sizes is below some threshold, for example 10%.

Another way to ensure the error introduced by discretising the equations is small is to ensure that the linear approximation is valid. This must be true for both the background stellar model, and also for the solution. This is done by using a sufficiently fine grid of cells. This required minimum resolution will not be constant across the whole star, however. The solution will require a fine resolution in regions where large changes occur over small scales, such as in the radiative core of a star (where the solution may be highly oscillatory). Locations in the star where the stellar model changes over small scales will also require high resolution, and may also cause large gradients in the solution, making it doubly important to ensure sufficient resolution.

The background model itself is calculated using Modules for Experiments in Stellar Astrophysics (MESA) (Paxton et al. (2011); Paxton et al. (2013); Paxton et al. (2015); Paxton et al. (2018); Paxton et al. (2019)) to generate 1D, spherically symmetric models of stars. This enables the observed parameters of any system that I may seek to recreate to be matched, varying the mass, radius, and age of the star, amongst other things. There is, however, some exploration required with this process, as MESA does not retrofit parameters such as brightness or surface temperature, but rather evolves the star from the initial properties. The example inlist as used in creating the stellar models in this work is given in Appendix H.

MESA outputs the equilibrium state of the star on a grid with varying resolution, according to what is required to accurately model the star's evolution. This can result in areas which require high resolution to properly capture the solution to the oscillation equations having low resolution in the MESA model. For example the radiative core of a star, where MESA does not need a high resolution grid, but where the solution to the oscillation equations will be highly oscillatory. At the base of the convection zone gradients in the equilibrium model may become very steep, such that the MESA model does not accurately capture the variation of the equilibrium state here. This leads to an apparent discontinuity is the gradients given by MESA, which can result numerical artefacts at the base of the convection zone.

In order to convert from the MESA grid to the grid used in the Henyey solver linear interpolation is used in order to estimate values at the new grid locations. In this conversion from one grid to another it is important to ensure that the new grid's resolution is at least the resolution of the MESA model at all points, in order to ensure that the variation of the equilibrium state of the star is accurately captured.

### 2.3.3 Memory limitations

An unfortunate reality which must be faced when seeking to increase the resolution used in the Henyey solver, is the fact that we only have access to finite computing resources. In particular, the RAM (random access memory) requirements have been the primary limiting factor in the quest for ever greater resolution.

The Henyey method itself is partly responsible for this – once the outer boundary conditions have been applied to find the solution at the stellar surface, this information is then propagated back down to the centre of the star, requiring information about cell $k$ to be stored in order to be used in this inward-going recursion relation. Whilst it would be possible to forego this procedure and only produce a complete solution at the very surface of the star, that would undermine the credibility of the process

as it would not be known whether the solution throughout the rest of the star was reasonable and within the assumptions of the model.

In order to minimise the memory required to complete this procedure, the necessary information for the inward-going recursion relation was compressed into its most minimal form. This is achieved by reexpressing the chosen recurrence relation (see section 2.3.1 and appendix C) into the form

$$\boldsymbol{f}_k = \mathbf{RECu}_k \boldsymbol{u}_{k+1} + \mathbf{RECv}_k \boldsymbol{v}_{k+1} + \boldsymbol{RECc}_k \tag{2.27}$$

where $\boldsymbol{f}_k$ is a stand-in for either $\boldsymbol{u}_k$ or $\boldsymbol{v}_k$ depending on the case used. Then $\mathbf{RECu}_k$, $\mathbf{RECv}_k$, and $\boldsymbol{RECc}_k$ are found by comparing coefficients with the chosen recurrence relation (either equation C.18 or C.19). Then equation 2.26 is used to calculate whichever of $\boldsymbol{u}_k$ and $\boldsymbol{v}_k$ remains unknown. Because of this we only require 4 matrices and 3 vectors to be saved over the whole star ($\boldsymbol{\alpha}$, $\mathbf{RECu}$, $\mathbf{RECv}$, $\boldsymbol{RECc}$, $\boldsymbol{\gamma}$, $\boldsymbol{u}$, $\boldsymbol{v}$). The other arrays used are then only used to relate cells $k$ and $k+1$, then overwritten for the next step such that their memory requirement is independent of the total number of cells. Using this approach rather than naïvely keeping all of the arrays in the memory allows more than an order of magnitude increase in the possible resolution.

### 2.3.4 Testing

Once the Henyey solver is producing an output, it is natural to question the validity of the solution. The two primary facets to test are the general reliability of the program in producing a solution which accurately reflects the input equations, which leads on to the second facet: ensuring that the implementation of the equations is dependable.

To investigate the general reliability of the code different sets of simultaneous equations were solved, and the numerical solution compared to the known analytical solution. To begin with, very simple sets of algebraic simultaneous equations were used. The solutions were varied, from constants or low order polynomials up to sinusoidal oscillations, with both the amplitude and wavelength varying across the grid. This was then used to test the limits of the program by finding the resolution limit when peaks could no longer be accurately resolved. The next step was to test differential equations, starting simply and becoming increasingly complex, as before. By building up to very complex sets of simultaneous differential equations in small increments, the program was tested in its ability to accurately solve the equations it was given in a wide variety of situations, and the limitations to its abilities were also explored so that such a failure could be spotted and diagnosed if it occurred again.

The next step is to ensure that our trust in the stellar oscillation equations which we have put into the Henyey solver are accurate. This requires the discretisation and interpolation of the equations to be done effectively, as discussed in section 2.3.2, and also that the equations to be carefully framed in order to avoid non-invertible matrices or divergent coefficients at all locations in the star, particularly at the centre of the star where divisions by small quantities could occur.

To test the implementation of the equations and the stability of the solution, the equations to be solved were slightly altered and the solutions then compared to the original solution. The impact of a $\pm 1$ per cent change in resolution was investigated, to determine what conclusions could be drawn about the solution in general, and what might be more limited by the parameters of the numerical method. In this case, the solution was found to be qualitatively similar throughout the star: spatial oscillations in the radiative core, which become evanescent in the convective envelope, with a sharp change in the radiative skin at the surface of the star. The spatial wavelength, and the value around which the oscillations occurred remained consistent throughout the models, showing that this behaviour was robust to changes in resolution. However, the amplitude of the oscillation within the radiative core, particularly towards the centre of the star, was seen to vary. This may be due to the recurrence relation near to nodal points of the oscillation varying slightly as the exact separation from a node varied. This shows that, even for a solution which is generally well-resolved, the exact quantitative behaviour within the stellar core is difficult to predict because of the highly oscillatory behaviour, and shows the importance of assigning the resolution throughout the star carefully.

As well as testing the stability against changes in the numerics, the orbital separation, $D$, was also varied in order to test how the uncertainty in a physical parameter would affect what conclusions could be drawn. Changing $D$ affects both the strength of the perturbation (which is proportional to $D^{-3}$) and the orbital period (which is proportional to $D^{\frac{3}{2}}$) which affects the spatial wavelength of the oscillations in the star. Again, the qualitative response was found to be unaffected, although there were some quantitative changes. The amplitude of oscillations in the centre of the star was found to be affected, similar to that caused by a change in resolution – possibly this is for a similar reason, as the change in spatial wavelength would slightly change the required resolution, and therefore the proximity of grid points to the nodal points of the oscillations. Throughout the convective zone the magnitude of the response was altered in line with the expected change due to the change in the strength of the

perturbation, but the response at the very surface, in the radiative skin, was found to be almost totally unaffected.

Additionally, the validity of the assumptions used to derive the equations must be tested. Of these, the assumption of small perturbations is the one most susceptible to breaking (assuming the stellar model has already been chosen appropriately). Care must be taken towards the centre of the star, where perturbations to the displacement and the flux can be large compared to their background values, as both the radial position, $r$, and the background flux, $F_0$ go to zero at the centre of the star. The surface boundary conditions were also investigated to understand the impact they had on the solution – we tested different conditions on $\Delta p$ and found that the response does not strongly depend upon the choice of implementation of the different reasonable boundary conditions we looked at.

Finally, the solution can be compared against previous work to assess the similarities and differences. This was done for this work by using Terquem et al. (1998) as a reference. The behaviour was found to be similar, exhibiting the same qualitative behaviour throughout the star, other than some deviation in the predicted behaviour at the surface, which will be explored later in this work. Quantitatively the behaviour was also found to be similar, particularly with regards to the radial displacement on average following the equilibrium tide prediction throughout the bulk of the star.

Overall, this shows that the solution is stable, and robust to changes in the parameters used, although there are limitations to the conclusions which can be drawn. The qualitative behaviour throughout the star was found to be very stable, and could be recovered even at very low resolution when the oscillations in the radiative core were not resolved well. However, the quantitative response in the core does depends on both the resolution used and the uncertainties of the physical parameters of the system, meaning that drawing specific quantitative conclusions from the behaviour within the radiative core should be avoided. Throughout the convective envelope, and at the stellar surface, the solution was found to be very robust. Having successfully determined that we can trust the numerical method, we shall now investigate whether the solution can be trusted on physical grounds.

# Chapter 3

# Investigating nonadiabaticity

Having now set out the framework to be used to solve the stellar oscillation equations, and concluded that the numerical method is able to accurately produce a solution to those input equations, we now discuss the physics involved, and how the assumptions used to derive the oscillation equations impact the solution.

This is focussed upon one particular change in the model compared to some previous work: the removal of the assumption that the oscillations are adiabatic. What this means is discussed in section 3.1, where some methods to model the perturbation to the flux are set out and explored. Having gone to all that effort, we then check that it was actually worthwhile in section 3.2, where the specific details of where we expect non-adiabatic effects to come into play, and how we might expect that to affect the solution, are investigated. We then present the numerical solutions in section 3.3, which are then discussed in section 3.4.

As the equilibrium tide has often been used as a simple approximation, comparison is made between the equilibrium tide solution and the fully non-adiabatic solution calculated in this work. In previous work focus has largely been upon the radial displacement induced by the tidal potential, and the horizontal displacement has been somewhat neglected, potentially because it does not contribute to the disc–integrated luminosity variations. Conditions very near the surface, which is where we are able to observe, are difficult to model, and the simple approximation may break down. Previous works have suggested that the horizontal displacement may be particularly poorly described by the equilibrium tide in this region (Savonije & Papaloizou (1983); Arras et al. (2012)), so the impact of nonadiabaticity on the horizontal displacement is highlighted in this chapter.

## 3.1 What is nonadiabaticity?

To understand what it means for the stellar oscillations to be non-adiabatic, we first consider the inverse – what does it mean for a process to be adiabatic? In words, an adiabatic process is one in which heat is not transferred from one fluid element to another. Therefore the Lagrangian perturbation to the entropy, $\Delta s$, is equal to zero. This can be understood by examining the linearised energy equation, equation 2.8, after slightly restating it as

$$im\omega\rho_0 T_0 \Delta s = -\nabla \cdot \boldsymbol{F'}. \tag{3.1}$$

In the adiabatic case, as $\Delta s = 0$, we must conclude that the divergence of $\boldsymbol{F'}$ is also zero. This means that there are no sources or sinks for radiated energy – any given fluid parcel does not change its internal energy by either emitting or absorbing energy.

We may consider the perturbation to the flux to be given by the perturbation to the internal energy of a fluid element which is expected to be transported over a time $t_{\text{th}}$, the thermal timescale. Considering the Eulerian perturbation to the internal energy, $u'$, the divergence of the flux can be roughly approximated as

$$|\nabla \cdot \boldsymbol{F'}| \sim \frac{1}{\mathrm{d}r} \frac{u' A \mathrm{d}r}{A t_{\text{th}}} \sim \frac{u'}{t_{\text{th}}} \tag{3.2}$$

where $\mathrm{d}r$ is the length scale over which we expect variations to occur, and $A$ is the area of the region under consideration. This can be used to express equation 3.1 as

$$|\rho_0 T_0 \Delta s| \sim \frac{t_{\text{osc}}}{t_{\text{th}}} u' \tag{3.3}$$

where $t_{\text{osc}} = \frac{2\pi}{m\omega}$ is the oscillation timescale. If the oscillation timescale is much shorter than the thermal timescale, we expect that $\Delta s \sim 0$, therefore the oscillation will be approximately adiabatic. If $t_{\text{osc}} \gtrsim t_{\text{th}}$ then we expect $\Delta s \neq 0$, and non-adiabatic effects will become important.

The adiabatic case (where $t_{\text{th}} \gg t_{\text{osc}}$) might be valid if, for example, the fluid element is very well insulated from its surroundings such that heat cannot flow into or out of the fluid element (we know this is not true within the star, as the background flux is non-zero, showing that energy can be transported) or if the timescale of the oscillations is short, such that energy cannot be transported from one parcel to another within an oscillation period. This is discussed in more detail below, in section 3.2.1. Briefly, we expect that the oscillation will be adiabatic in a region if the internal energy is much larger than the flux passing through a parcel within an oscillation

period. This will be valid for most of the star, but may break down either where the flux is very large (for example just outside a shell of nuclear fusion in the core of a massive star) or the energy density becomes very small (such as towards the stellar surface).

If the area of interest in the star is likely to behave approximately adiabatically it could be simpler to avoid perturbing the flux and assume that $\Delta s = 0$. Use of this approximation avoids the need to perturb the energy flux, which can be difficult to model well in some situations, particularly in the convective region as current models for convective flux can be difficult to work with. If the area of interest is likely to be affected by non-adiabatic effects, however, it is then necessary to account for the perturbation to the flux in order to accurately model that. Some models for perturbing the radiative and convective flux are discussed below.

Previous investigations into non-adiabatic tidal oscillations have taken different approaches to dealing with the presence of these effects. As the radiative diffusion approximation described in section 3.1.1 is well understood, focussing on the perturbation to the radiative flux as the primary source of nonadiabaticity is one approach that has been used. Savonije & Papaloizou (1983) investigated dissipation in massive stars, with convective cores and radiative envelopes, where it was expected that most of the dissipation would occur in the radiative region, such that only the radiative flux perturbation need be considered.

Similarly, Terquem et al. (1998) assumed that the non-adiabatic response would be close to the adiabatic response, such that first order perturbation theory could be used to introduce the non-adiabatic effects through radiative diffusion, even within the convection zone. This avoids the need to perturb the convective flux specifically, although it will break down in regions where the non-adiabatic effects become significant.

Work by Pfahl et al. (2008) seeks to include the non-adiabatic effect within the convection zone by considering the response of convection to the perturbation. The method used is based upon the description of pulsating white dwarfs set out by Brickhill (1983), where convection is taken to be efficient everywhere, such that the convection zone is taken to be entirely isentropic, and the Lagrangian perturbation to the entropy is set to be constant, such that $\frac{\partial \Delta s}{\partial r} = 0$. Although this does simplify the calculation, and avoids the need to explicitly perturb the convective flux, setting $\Delta s$ to be constant precludes any variation in the upper convective zone, precisely where convection becomes inefficient and non-adiabatic effects are expected to become prevalent.

The methods set out in this chapter seek to improve upon these previous investigations by providing a plausible mechanism to describe the perturbations to the radiative and convective fluxes, especially in the region where non-adiabatic effects are likely to be most significant.

### 3.1.1 Radiative diffusion

The distance travelled by a photon within a star is very short, with a mean free path of under 1 cm throughout a sun-like star (Mitalas & Sills, 1992). This means that any photon is expected to undertake a random walk on a scale much smaller than the scale of the structure of the star, enabling the energy flux due to radiation to be described as a diffusive process.

The energy density of blackbody radiation is given by $u = aT^4$, where $u$ is the energy density, $a = \frac{4\sigma}{c_*} = 7.5657 \times 10^{-15}$ erg cm$^{-3}$ K$^{-4}$ is the radiation density constant ($\sigma$ is the Stefan-Boltzmann constant), $c_*$ is the speed of light (the subscript-asterisk is to differentiate it from the sound speed), and $T$ is the temperature. We imagine a plane normal to some direction, $\hat{\boldsymbol{z}}$, between two fluid elements which are at locations $z$ and $z + \delta z$.

The energy passing through the plane in time $\delta t$ will be given by

$$\mathrm{d}E = F_{\mathrm{rad},z} A \, \delta t \tag{3.4}$$

where $F_{\mathrm{rad},z}$ is the radiative flux in the $\hat{\boldsymbol{z}}$ direction and $A$ is the surface area of the plane. This can be expressed in terms of energy density passing through the plane, as

$$\mathrm{d}E = \frac{1}{2} u(z) \langle v_z \rangle A \delta t - \frac{1}{2} u(z + \delta z) \langle v_z \rangle A \delta t \tag{3.5}$$

where $\langle v_z \rangle$ is the velocity of photons projected along the $\hat{\boldsymbol{z}}$ direction, averaged over all the photons which pass through the plane in time $\delta t$. The factor of $1/2$ arises as, in an isotropic distribution, only half of the photons will be travelling towards the plane, and we only include the energy density contribution from them.

To find the average velocity in the $\hat{\boldsymbol{z}}$ direction, $\langle v_z \rangle$, we must consider whether a given photon will pass through the plane in time $\delta t$. Photons travelling in the direction $\hat{\boldsymbol{n}}$ such that $\hat{\boldsymbol{n}} \cdot \hat{\boldsymbol{z}} = \cos\theta$ in a volume $AC_* \cos(\theta) \delta t$ will pass through the plane with a projected velocity of $c_* \cos(\theta)$. Using this as the weighting of the average, we get

$$\langle v_z \rangle = \frac{\int_0^{2\pi} \int_0^{\frac{\pi}{2}} A c_* \cos(\theta) \delta t \, c_* \cos(\theta) \, \sin(\theta) \, \mathrm{d}\theta \, \mathrm{d}\phi}{\int_0^{2\pi} \int_0^{\frac{\pi}{2}} A c_* \cos(\theta) \delta t \, \sin(\theta) \, \mathrm{d}\theta \, \mathrm{d}\phi} = \frac{2}{3} c_*. \tag{3.6}$$

Comparing equations 3.4 and 3.5, and using $u(z+\delta z) \approx u(z) + \frac{\partial u}{\partial z}\delta z$, and taking $\delta z$ to be the mean free path of a photon, $\lambda_{\text{mfp}}$ gives

$$F_{\text{rad},z} = -\frac{1}{3} c_* \lambda_{\text{mfp}} \frac{\partial u}{\partial z} \tag{3.7}$$

where the mean free path is given by $\lambda_{\text{mfp}} = 1/(\kappa\rho)$, where $\kappa$ is the opacity and $\rho$ is the density. The above equation is also true for the $\hat{\boldsymbol{x}}$ and $\hat{\boldsymbol{y}}$ directions, if $z$ is replaced with the appropriate variable. The vector radiative flux can then be given as

$$\boldsymbol{F}_{\text{rad}} = -\frac{c_*}{3\kappa\rho}\boldsymbol{\nabla} u = -\frac{4}{3}\frac{a c_* T^3}{\kappa\rho}\boldsymbol{\nabla} T = -K\boldsymbol{\nabla} T \tag{3.8}$$

where $K$ is the radiative thermal conductivity, which is related to the opacity, temperature and density through: $K = 4ac_*T^3/(3\kappa\rho)$.

This can be used to model the perturbation to the flux wherever the diffusion approximation is valid, which requires that the mean free path of the photons is much smaller than the length scales of the problem – the size of the cell and the local scale height. Within the radiative core this approximation will hold well, as these scales will be several orders of magnitude larger than the mean free path, and we expect that this approximation will accurately describe the energy flux in this region.

At the very surface of the star the mean free path may become very large, such that this approximation breaks down. In this region photons may be able to travel a long way before interacting with stellar material (that is, if they don't escape entirely). This region will therefore be impacted by non-adiabatic effects as heat can flow between fluid parcels within one oscillation period, and it is therefore important to have some method of modelling this behaviour.

In the background state, the flux profile follows the radiative diffusion approximation, even within this region, as sufficient time will allow the adjacent fluid parcels to interact and reach the state as described by the diffusion approximation. In using radiative diffusion to describe the perturbation in this region we assume that the timescale of the oscillation is sufficiently long that this interaction between adjacent fluid parcels can occur, and a new equilibrium is reached.

The timescale of the diffusive process will be given by

$$\tau \sim \frac{(\Delta x)^2}{D} \sim \frac{\lambda}{c_*} \tag{3.9}$$

where $\Delta x$ is the length scale of interest, and the diffusion coefficient is $D = \frac{1}{3}\lambda_{\text{mfp}} c_*$. As we are interested in the time taken for a fluid element to reach an equilibrium

state with its neighbours, the length scale we are concerned about is the distance which a photon could travel away from its parcel of origin, which is $\lambda_{\text{mfp}}$. For even the largest mean free paths at the surface, this timescale is found to be on the order of milliseconds. As the timescale of the oscillations is many orders of magnitude greater than this, we can assume that the radiative flux is able to relax to a new equilibrium state under the perturbation, such that radiative diffusion is a useful description of the flux in this region, without needing to fully model the radiative transfer and non-local effects.

This approximation appears in only one of the oscillation equations: equation 2.18. As given in section 2.1, the equation includes both radiative diffusion and the perturbation to the convective flux. To remove the perturbation to the convective flux, the two terms involving the background convective flux, $F_{c,r,0}$ must be set to 0.

This description of the perturbation to the radiative flux is expected to well describe the stellar response where radiation dominates the transport of energy. For stars similar to the sun, however, this neglects a large convective envelope where other processes might contribute to non-adiabatic behaviour more. Whilst there will be some small radiative flux perturbation in the convective region, a small change in the convective flux may provide a much greater contribution to the total perturbed flux.

### 3.1.2 Treatment of convection

For low mass stars, convection occurs close to the stellar surface and is likely to have an impact on the observable behaviour of the star. Here we adopt a description based on the local time dependent Mixing Length Theory (MLT) that has been discussed by many authors (see eg. Unno, 1967; Gough, 1977; Salaris & Cassisi, 2008; Houdek & Dupret, 2015).

Originally introduced by Biermann (1932), MLT has been widely used and has been particularly applied to model stellar evolution. At its core, the model states that a convective flow will travel a distance $l$, the mixing length, which is given by $l = \alpha H_p$, where $H_p$ is the pressure scale height. The parameter $\alpha$ is free to be adjusted in order to match observations. However, the value of $\alpha$ is different depending on the situation to be modelled, such as ranging from $\alpha = 2.8 - 1.8$ for red giant branch stars, or even varying with depth (Kupka & Muthsam, 2017). Furthermore, even adjusting $\alpha$ does not always enable observations to be matched, as the turbulent viscosity implied by MLT fails to recreate the observed circularization rates of main sequence solar-type binaries (Terquem et al., 1998).

On the other hand, its great advantage is in its simplicity. Originally stated as a steady-state 1-D, local model, it has been extended to account for time-dependence. In this, there are two distinct main approaches to understanding the physics of MLT (Houdek & Dupret, 2015), one in which the turbulent flow is analogous to kinetic gas theory (Gough, 1977) – a convective element is accelerated from rest, before instantaneously breaking up at the end of its lifetime. The other considers the buoyant force and turbulent drag to be in equilibrium during the motion such that there is a continuous exchange of momentum between the element and its surroundings (Unno, 1967). The two approaches are found to be complementary in static envelopes, but lead to different expressions for the heat and momentum fluxes if the envelope is pulsating.

In the treatment of convection described here the focus has been upon keeping the approach both simple and appropriate to the task. The approximation developed in this section is designed to match with whatever version of MLT was used to attain the background model, and is best suited to the region in which non-adiabatic effects are expected to be most prominent.

According to the MLT, under steady state conditions, or when it can be assumed to have relaxed to an equilibrium value, the convective flux is given by an expression of the form:

$$\mathbf{F}_{\rm c} = -A\boldsymbol{\nabla} s, \tag{3.10}$$

where $s$ is the entropy and $A$ depends on the convective velocity, the mixing length and various other parameters (see section 2.1 and equation 2.5 for more details).

In this work, we first consider the case when convection is frozen, i.e. the convective flux is unchanged by the perturbation. This leads to a value of the Lagrangian displacement at the surface of the star which differs in magnitude from the standard equilibrium tide value by more than an order of magnitude. We then calculate the response to forcing allowing for the perturbation of the convective flux. Again, significant departure from the equilibrium tide is obtained in that case, although the results are qualitatively different. This enables us to assess the effect of convection on the Lagrangian displacement, within the framework of the MLT.

In order to calculate the perturbed convective flux in the calculations for which the convection has assumed to have relaxed to quasi-steady conditions, given the uncertainties in the MLT, we have followed two approaches. In the first, which we label approach A, we assume that it is dominated by the perturbation to the entropy

gradient displayed on the right hand side of equation (3.10). That is to say, its linearised form is approximated as:

$$\mathbf{F}'_{\mathrm{c}} = -A\boldsymbol{\nabla}s', \tag{3.11}$$

(see section 2.1 for more details). We also use the fact that gradients are dominated by the radial component, so that the perturbed convective flux is radial with that component being given by:

$$F'_{\mathrm{c},r} = -A\frac{\partial s'}{\partial r}. \tag{3.12}$$

This is because the variations in the radial direction turn out to be over a scale $\lambda_{\mathrm{r}}$ which is very small compared to the radius $R$ of the star, and the ratio of radial to horizontal gradients near the surface of the star is on the order of $R/\lambda_{\mathrm{r}} \gg 1$.

To ensure that this approach is self-consistent, the behaviour of the entropy perturbation throughout the convection zone was investigated, and is shown in Figure 3.1. In the radiative zone $\Delta s$ is very small compared to $s'$, suggesting that the response here is very nearly adiabatic. Throughout much of the convective zone $\Delta s$ remains small, only becoming large towards the surface, which is where we expect non-adiabatic effects to come into play. In this region at the top of the convective zone the radial gradient of the entropy perturbation becomes very large, such that it is much greater than the tangential gradient, which is consistent with our assumption that the perturbation to the convective flux can be taken to be approximately radial.

In the second approach, which we label approach B, we have allowed for variations in $A$ that incorporate perturbations to the state variables and also to the convective velocity. This also has a dependence on the entropy gradient (see section 2.1). We further remark that the procedures we have adopted are consistent with those used to calculate the stellar model we have chosen as our equilibrium background. The right-hand panel of Figure 3.1 compares the contributions of the fractional entropy gradient to the fractional pressure and temperature perturbations. It is shown that, except for a small region around $r \approx 0.87R$, the fractional entropy gradient is the dominant term. This suggests that approach A is self-consistent and is a reasonable and practical approximation, although imperfect. Therefore brief comparisons with perturbed convection using approach B are worthwhile.

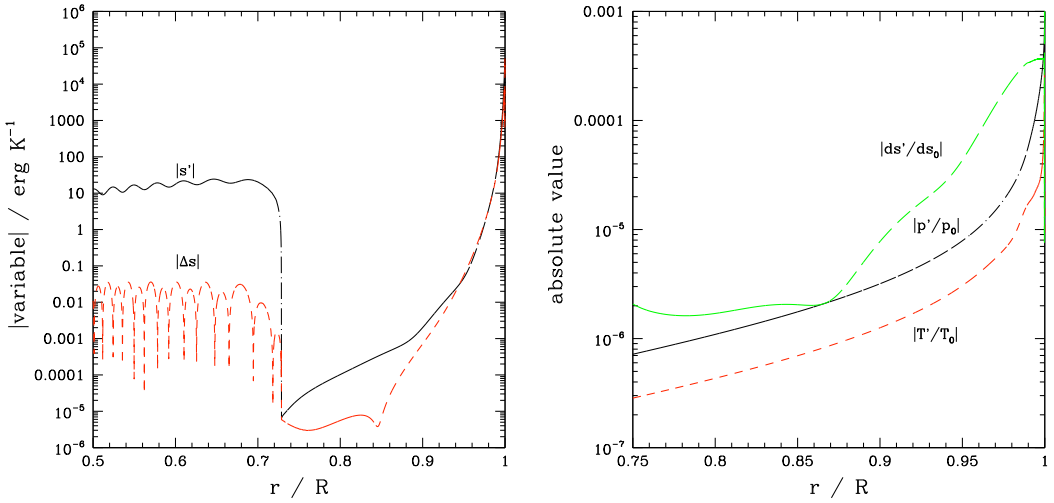


Figure 3.1: The entropy perturbation in the case of perturbed convection using approach A is shown in the left-hand panel, showing the amplitudes of both the Eulerian perturbation, $|s'|$, and the Lagrangian perturbation, $|\Delta s|$. Regions in which $|s'| \gg |\Delta s|$ suggest approximately adiabatic behaviour. The response remains approximately adiabatic throughout the bulk of the convective zone, as $\Delta s$ remains small up until the upper region of the convective zone, where the gradient of the entropy perturbation becomes very large. The right-hand panel shows the fractional variable components of the convective flux. Throughout the convection zone $|ds'/ds_0| \gtrsim |p'/p_0|$ and $|ds'/ds_0| > |T'/T_0|$, such that the approximation that $A$ is unchanged by the tidal perturbation is reasonable, if imperfect.

## 3.2 Why does nonadiabaticity matter?

Now that we are equipped with the tools to model non-adiabatic behaviour, we address why having these models matters. The particular cases of a 1.0 $M_\odot$ star and a 1.4 $M_\odot$ star are used and explored in detail, so that the expected impact of non-adiabatic effects can be explored physically and with particular focus on where we expect such departures from the simpler models to occur. The case that only the perturbation to the radiative flux is used is referred to as the 'frozen convection' case. The cases where the perturbation to the convective flux is used are referred to according to whether approach A or approach B, as discussed above, has been used – if not made explicitly clear perturbed convection is taken to refer to approach A.

At the surface of both the 1 $M_\odot$ and 1.4 $M_\odot$ stars, there is a thin, strongly stratified layer, which the increased photon mean free path in this region has made very stable against convection. This is illustrated in Figure 3.2, which shows $N^2/(m^2\omega^2)$ against $r/R$ in the surface region, where $R$ is the stellar radius and $N^2$ is the square of the Brunt–Väisälä frequency, defined through:

$$N^2 = \frac{1}{\rho_0}\frac{dp_0}{dr}\left(\frac{1}{\rho_0}\frac{d\rho_0}{dr} - \frac{1}{\Gamma_1 p_0}\frac{dp_0}{dr}\right), \tag{3.13}$$

Here $\Gamma_1 = d\ln p_0/d\ln\rho_0|_s$ is the adiabatic exponent, with the derivative being taken at constant specific entropy. Negative values of $N^2$ indicate a convection zone, which extends from $r/R = 0.73$ to $r/R = 0.9999$ for the 1 $M_\odot$ star and from $r/R = 0.93$ to $r/R = 0.9999$ for the 1.4 $M_\odot$ star.

Near the surface, $N^2$ transitions suddenly from being large and negative to being large and positive, reflecting a transition from a strongly superadiabatic convection region to a strongly stably stratified region. In this thin, radiative layer, the local thermal time scale is much shorter than the period of the forced oscillations, enabling heat to escape on a timescale much shorter than this period. Accordingly, we expect that non–adiabatic effects will be important in this region. However, the region near the surface in which non–adiabaticity is important extends below this stably stratified layer into the outer parts of the convection zone, as we show in Section 3.2.1.

### 3.2.1 Extent of the non–adiabatic zone below the stellar surface

We define $r_{\rm na,f}$ and $r_{\rm na,p}$ as the radius of the base of the non–adiabatic zone when convection is frozen and perturbed, respectively. To evaluate this radius, we start by writing the perturbed energy equation under the form:

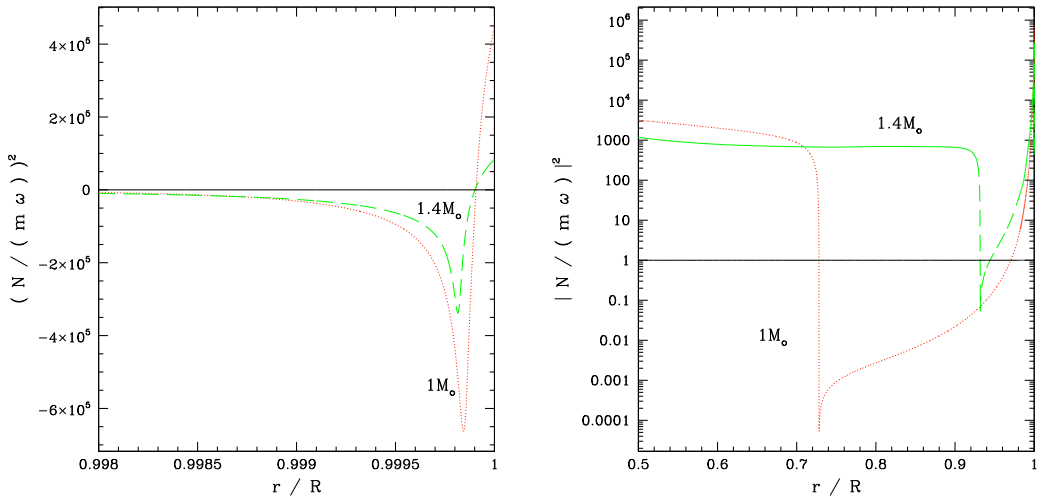


Figure 3.2: The left panel shows $N^2/(m^2\omega^2)$ as a function of $r/R$, where $R$ is the stellar radius, near the surface, for an orbital period of 4.23 days. The red dotted line corresponds to a 1 $M_\odot$ star, and the green dashed line corresponds to a 1.4 $M_\odot$ star. The squared, normalised Brunt-Väisälä frequency (in units of the angular frequency of the oscillations – twice that of the orbit) indicates the structure of the star: a negative value corresponds to an imaginary frequency and implies convection; a positive value indicates a real frequency and therefore a stratified, radiative region. The right panel shows $|N^2/(m^2\omega^2)|$ in logarithmic scale for the outer 50% of the stellar radius with the same colour coding. This quantity passes through zero near $r/R = 0.73$ and 0.94 for the lower and higher mass, respectively, which correspond to the inner boundaries of their convective envelopes. This behaviour is not fully resolved in the plots. In convection zones, the quantity $|N/(m\omega)|$ measures the ratio of the inverse forcing frequency to the convective time scale. It can be seen that this exceeds unity for the solar mass model for $r/R > 0.97$ and for $r/R > 0.94$ for the 1.4 $M_\odot$ star.

$$\rho T\left(\frac{\partial s'}{\partial t}+\boldsymbol{u}\cdot\boldsymbol{\nabla}s\right)=-\boldsymbol{\nabla}\cdot\boldsymbol{F}', \tag{3.14}$$

where $\boldsymbol{u}$ is the vector velocity. (Note that although the subscript '0' does not appear here as we are only concerned with estimates, background state variables are used). In this section, we are interested in the cases where either the perturbed radiative flux, which we denote $\boldsymbol{F}'_{\rm rad}$, or the perturbed convective flux, $\boldsymbol{F}'_{\rm c}$, dominates. As here we are only concerned with an estimate of the extent of the non–adiabatic zone, we approximate $\boldsymbol{F}'_{\rm rad}$ and $\boldsymbol{F}'_{\rm c}$ by assuming that most of the contributions to these perturbed quantities come from the radial gradients of temperature and entropy, respectively. Therefore:

$$F'_{\rm c}\sim -A\frac{\partial s'}{\partial r},\ \text{with}\ A\sim\rho v_{\rm c}lT, \tag{3.15}$$

to within a factor of order unity, where $v_{\rm c}$ is the convective velocity and $l$ is the mixing length (see equation 2.5, where we remark that we have neglected the cooling term in the denominator). For the radiative flux, we have $F'_{\rm rad}\sim -K\partial T'/\partial r$. We remark that perturbations to the opacity may also contribute to $F'_{\rm rad}$. However, this is not expected to change the estimates given below significantly when, as in our case, the non adiabatic layer extends below the very strongly superadiabatic region into regions where the opacity is no longer increasing very rapidly with temperature. Using thermodynamic relations, changes in entropy can be related to changes in temperature through $T\boldsymbol{\nabla}s=\varepsilon c_p\boldsymbol{\nabla}T$, where $\varepsilon=1-\nabla_{\rm ad}/\nabla$ with $\nabla=(\partial\ln T/\partial r)/(\partial\ln P/\partial r)$. (In the deep parts of the convection zone, convection is efficient and $|\varepsilon|\ll 1$.) Neglecting variations of $\varepsilon$, this relation implies $\partial T'/\partial r=T(\partial s'/\partial r)/(\varepsilon c_p)$, and therefore:

$$F'_{\rm rad}\sim -D\frac{\partial s'}{\partial r},\ \text{with}\ D\sim\frac{KT}{\varepsilon c_p}. \tag{3.16}$$

So both the convective and radiative fluxes can be viewed as arising from the diffusion of entropy with different diffusion coefficients. Noting $\lambda_r$ the radial scale on which perturbations vary (near the stellar surface, $\lambda_r\ll r$) we may then set $\partial/\partial r\sim 1/\lambda_r$. This yields $|\boldsymbol{\nabla}\cdot\boldsymbol{F}'|\sim|F'|/\lambda_r$, so that:

$$|\boldsymbol{\nabla}\cdot\boldsymbol{F}'_{\rm rad}|\sim\frac{Ds'}{\lambda_r^2}\ \text{and}\ |\boldsymbol{\nabla}\cdot\boldsymbol{F}'_{\rm c}|\sim\frac{As'}{\lambda_r^2}; \tag{3.17}$$

Note that, in the left hand side of equation (3.14):

$$\left|\frac{\partial s'}{\partial t}\right|=m\omega|s'|=\frac{2\pi}{P_{\rm osc}}|s'|, \tag{3.18}$$

where $m = 2$ and $P_{\rm osc} = 2\pi/(m\omega)$ is the period of the oscillations.

We now look at the two cases of frozen and perturbed convection in turn, and discuss where convection is relaxed.

#### 3.2.1.1 Frozen convection:

When convection is frozen, $\boldsymbol{F}' = \boldsymbol{F}'_{\rm rad}$. In this case, equation (3.14) yields:

$$\left|\frac{1}{s'}\frac{\partial s'}{\partial t} + \boldsymbol{u}\cdot\frac{\boldsymbol{\nabla} s}{s'}\right| \sim \frac{D}{\rho T \lambda_r^2} \sim \frac{KT}{\varepsilon c_p T \rho \lambda_r^2} \sim \frac{F_{\rm rad} H_p}{\varepsilon c_p T \rho \lambda_r^2} \sim \frac{4\pi r^2 F_{\rm rad}}{c_p T 4\pi r^2 \rho \lambda_r}\frac{H_p}{\varepsilon\lambda_r}, \quad (3.19)$$

where we have used $F_{\rm rad} \sim KT/H_p$, where $H_p$ is the pressure scale height. In the numerator, the term $4\pi r^2 F_{\rm rad}$ is the radiative luminosity $L_{\rm rad}(r)$. In the denominator, $c_p T$ is approximately the internal energy per unit mass, $4\pi r^2 \rho\lambda_r$ is the mass within a spherical shell of radius $r$ and width $\lambda_r$, and therefore the product is approximately the internal energy $E_{\rm int}(r)$ contained within that shell. This relation can therefore be written as:

$$\left|\frac{1}{s'}\frac{\partial s'}{\partial t} + \boldsymbol{u}\cdot\frac{\boldsymbol{\nabla} s}{s'}\right| \sim \frac{H_p}{\varepsilon\lambda_r}\frac{1}{t_{\rm rad}}, \quad (3.20)$$

where $t_{\rm rad} = E_{\rm int}(r)/L_{\rm rad}(r)$ is the timescale on which energy is transported by radiation through a distance $\lambda_r$ at radius $r$. In the outer parts of the convection zone where convection is not efficient, $\varepsilon \sim 1$. We also have $\lambda_r \sim H_p$ there. The perturbation is non–adiabatic, and approximately isothermal, if $t_{\rm rad} \ll P$, which means that the right hand side of equation (3.20) is large compared to $|(\partial s'/\partial t)/s'|$. In that case, the balance is between $\rho T \boldsymbol{u}\cdot\boldsymbol{\nabla} s$ and $-\boldsymbol{\nabla}\cdot\boldsymbol{F}'_{\rm rad}$. In the opposite regime, in the adiabatic parts of the convective zone, $t_{\rm rad} \gg P$ and the balance is between $\partial s'/\partial t$ and $\boldsymbol{u}\cdot\boldsymbol{\nabla} s$ (that is to say, $\boldsymbol{\nabla}\cdot\boldsymbol{F}'_{\rm rad} \simeq 0$). The transition between the two regimes is therefore where $|(\partial s'/\partial t)/s'| \sim 1/t_{\rm rad}$, which means that the radius $r_{\rm na,f}$ of the base of the non–adiabatic zone is determined by $L_{\rm rad}(r_{\rm na,f}) = m\omega E_{\rm int}(r_{\rm na,f})$.

The internal energy in a spherical shell of width $\lambda_r \sim H_p$ at $r_{\rm na,f}$ is comparable to that between $r_{\rm na,f}$ and the stellar surface $R$ (since the mass density decreases sharply towards the surface). Therefore we approximate $r_{\rm na,f}$ by writing that the internal energy of the material in the region above that radius is equal to the energy transported by radiation through that radius during $P/(2\pi)$:

$$\frac{L_{\rm rad}}{m\omega} = \int_{r_{\rm na,f}}^{R} {\rm d}E_{\rm int}(r) = \int_{r_{\rm na,f}}^{R} \frac{6\pi k_{\rm B}\rho T r^2\,{\rm d}r}{\mu m_{\rm H}}, \quad (3.21)$$

where $k_{\rm B}$ is the Boltzmann constant, $\mu$ is the mean molecular weight per gas particle (including both ions and free electrons), and $m_{\rm H}$ is the mass of a Hydrogen atom.

For simplicity, the stellar material is taken to be a monatomic ideal gas. This gives estimates of $r_{\mathrm{na,f}}/R = 0.9995$ for $\mathrm{M} = 1\ \mathrm{M}_\odot$ and $r_{\mathrm{na,f}}/R = 0.9991$ for $\mathrm{M} = 1.4\ \mathrm{M}_\odot$. Figure 3.2 shows that $r_{\mathrm{na,f}}$ is roughly the inner edge of the super–adiabatic region, where $N^2$ has large variations.

#### 3.2.1.2 Perturbed convection:

In the parts of the convection zone where the perturbed convective flux dominates, equation (3.14) yields:

$$\left|\frac{1}{s'}\frac{\partial s'}{\partial t} + \boldsymbol{u}\cdot\frac{\boldsymbol{\nabla} s}{s'}\right| \sim \frac{A}{\rho T \lambda_r^2} \sim \left(\frac{l^2}{\lambda_r^2}\right)\frac{v_{\mathrm{c}}}{l} \sim \left(\frac{l^2}{\lambda_r^2}\right)\frac{1}{t_{\mathrm{c}}}, \tag{3.22}$$

where $t_{\mathrm{c}} \sim l/v_{\mathrm{c}}$ is the convective timescale. Within the MLT, this timescale is also given by $t_{\mathrm{c}} \sim 1/\sqrt{|N^2|}$. Note that $l \sim H_p$, and $\lambda_r \sim H_p$ in the outer parts of the convection zone. Above the radius $r_{\mathrm{na,f}}$ calculated in the case of frozen convection the radiative flux is not negligible, so the equation above does not apply. In the parts of the convection zone below this radius and where $t_{\mathrm{c}} \ll P$, which means that the perturbation is governed by diffusion rather than advection, the balance is between $\rho T \boldsymbol{u}\cdot\boldsymbol{\nabla} s$ and $-\boldsymbol{\nabla}\cdot\boldsymbol{F}'_{\mathrm{c}}$. In the opposite regime, in the parts of the convection zone which are governed by advection , $t_{\mathrm{c}} \gg P$ and, as in the case of frozen convection, the balance is between $\partial s'/\partial t$ and $\boldsymbol{u}\cdot\boldsymbol{\nabla} s$, which again implies $\boldsymbol{\nabla}\cdot\boldsymbol{F}'_{\mathrm{c}} \simeq 0$. Therefore, the transition between the two regimes is where $|(\partial s'/\partial t)/s'| \sim 1/(t_{\mathrm{c}})$, the corresponding radius $r_{\mathrm{na,p}}$ is approximately determined by $\sqrt{|N^2|} = m\omega$. In some circumstances (see below) this can correspond to the base of the non–adiabatic zone.

The transition radius discussed above gives the location of the transition from advective to diffusive transport of entropy. In the case that the background is very nearly isentropic on large scales (such that $\boldsymbol{\nabla} s$ is small) this transition may not correspond to a transition to non-adiabatic behaviour. A small entropy gradient will occur where convection is very efficient, and only very slightly superadiabatic. To give a measure of the efficiency of convection, we introduce the ratio

$$f_s = \frac{u_{\mathrm{int}}}{u_{\mathrm{KE}}} \sim \frac{p}{\rho v_{\mathrm{c}}^2} \sim \frac{c_s^2}{v_{\mathrm{c}}^2} \tag{3.23}$$

where $u_{\mathrm{int}}$ is the internal energy density, $u_{\mathrm{KE}}$ is the kinetic energy density of a convecting fluid element, and the squared speed of sound is $c_s^2 \sim \frac{p}{\rho}$. The inverse of this is then a measure of the superadiabaticity of convection (Hotta et al., 2012). A small convective velocity (and therefore a large value of $f_s$) corresponds to the situation where there is only a small buoyant force acting on the convecting fluid element, suggesting

that the background gradient is almost adiabatic and that convection is efficient – when the element arrives and dissipates it will only have transported a small amount of heat as the gradient is so nearly adiabatic, thus we expect the thermal timescale to be much longer than the convective timescale. A large convective velocity (and therefore a small value of $f_s$) will occur if the buoyant force is very strong and the fluid element is propelled quickly – such a fluid element arrives with a lot of excess heat, so the thermal timescale will be approximately equal to the convective timescale. We therefore expect the thermal and convective timescales to be related by $t_{\text{therm}} \sim f_s t_c$. Because this modifies the timescale to be considered when evaluating the location of $r_{\text{na}}$, an alternative approach could be used.

Similar to the approach used in the frozen convection case above (see equation 3.21) we estimate the non-adiabatic radius to be the innermost location at which the convective flux can replace the internal energy of the layer above within one oscillation period. This can be expressed as $u_{\text{int}} \sim F_c A t_{\text{osc}}/V$, where $A$ is the surface area under consideration, $V$ is the corresponding volume and $t_{\text{osc}}$ is the timescale of the oscillation. Above this radius we expect convection to be inefficient, and can then roughly approximate the convective flux as $F_c \sim \rho v_c^3$. As $u_{\text{int}} \sim pAH_p/V$, $V \sim AH_p$ and $t_{\text{osc}} \sim 1/(m\omega)$ this can be combined to give

$$m\omega \sim \frac{\rho v_c^2}{p}\frac{v_c}{H_p} \sim \left(\frac{v_c}{c_s}\right)^2 \frac{1}{t_c} \sim \frac{1}{f_s t_c}. \tag{3.24}$$

This is equivalent to equating the oscillation timescale to the thermal timescale, once the efficiency of convection has been accounted for, as $t_{\text{th}} \sim f_s t_c$. The radius specified by this condition is defined to be $r_{\text{na,p1}}$.

If this is to determine the location of the transition from adiabatic to non-adiabatic behaviour of the perturbations, then the increased thermal timescale must hold for the perturbation as well as for the background – this requires that the small degree of superadiabaticity is maintained for the perturbations as well as for the background. This condition may be approached when the background is approximately isentropic over large scales, as might be expected in the inner regions of the convection zone. However, the increased thermal timescale results in a similarly increased length scale over which the entropy gradient must be small. This is due to the fact that entropy perturbations may diffuse over a scale $H_p$ in time $t_c$, as used to determine the transition at $r = r_{\text{na,p}}$, but this is increased to a scale $f_s H_p$ over a time $f_s t_c$ for the transition at $r = r_{\text{na,p1}}$. If the background is not isentropic over such a scale then the transition to non-adiabatic behaviour may occur below $r_{\text{na,p1}}$.

Figure 3.2 shows that, for $\sqrt{|N^2|} = m\omega$, $r_{\rm na,p}/R = 0.97$ for $M = 1$ M$_\odot$ and $r_{\rm na,p}/R = 0.94$ for $M = 1.4$ M$_\odot$, which is significantly deeper than in the case of frozen convection. In addition we find that $r_{\rm na,p1}/R = 0.998$ for $M = 1$ M$_\odot$ and $r_{\rm na,p1}/R = 0.995$ for $M = 1.4$ M$_\odot$. Therefore non–adiabatic effects are potentially significant in a layer of the convection zone larger than could have been expected. As will be shown below, this has important consequences on the response of the star to the tidal forcing.

#### 3.2.1.3 Relaxed convection

In both the frozen and perturbed convection cases, the convective timescale is smaller than $P/(2\pi)$ in the non–adiabatic surface region (in the case of frozen convection it is even very small compared to $P/(2\pi m)$). Accordingly, we assume that convection relaxes to an equilibrium state in the non–adiabatic region, whereas below $r_{\rm na,f}$ for frozen convection and $r_{\rm na,p}$ for perturbed convection, the response is nearly adiabatic.

### 3.2.2 Illustrative estimates of $|\xi_h|/|\xi_r|$

Here, we focus upon the behaviour of the Lagrangian displacement from the equilibrium position, $\boldsymbol{\xi}$. In particular, we highlight the characteristic dominance of the horizontal displacement in the non–adiabatic surface layers, which is a significant departure from the behaviour expected from the standard equilibrium tide under adiabatic conditions. We argue that such a departure is expected because the strong constraint of hydrostatic equilibrium together with zero variation of the Lagrangian pressure and density perturbations, that is required to obtain the standard equilibrium tide, cannot be satisfied when the perturbation is non–adiabatic. The equilibrium tide approximation only applies for adiabatic perturbations in regions with $N^2 \neq 0$ (see section 1.3).

The radial component, $\xi_r$, is simply output in the solution of the oscillation equations (2.16) - (2.19). Given this complete solution, the horizontal displacement, $\boldsymbol{\xi}_h = \boldsymbol{\xi} - \xi_r \hat{\boldsymbol{r}}$, can be derived either from the linearised continuity equation or the linearised horizontal component of the equation of motion.

#### 3.2.2.1 The radial and horizontal components of the Lagrangian displacement

The linearised continuity equation, with the angular dependence retained:

$$\frac{\partial}{\partial t}\left(\rho' + \boldsymbol{\nabla}\cdot(\rho_0\boldsymbol{\xi})\right) = 0, \tag{3.25}$$

with

$$\rho' = \frac{\rho_0}{\chi_\rho p_0} p' - \frac{\rho_0}{T_0}\frac{\chi_T}{\chi_\rho} T', \tag{3.26}$$

can be rearranged to give an expression for the divergence of the horizontal displacement:

$$\boldsymbol{\nabla}\cdot\boldsymbol{\xi}_h = -\frac{\rho'}{\rho_0} - \frac{1}{\rho_0 r^2}\frac{\partial}{\partial r}\left(r^2\rho_0\xi_r\right). \tag{3.27}$$

The horizontal components of the equation of motion, with the angular dependence retained, give:

$$\boldsymbol{\xi}_h = \frac{1}{m^2\omega^2}\boldsymbol{\nabla}_\perp\left(\frac{p'}{\rho_0} + \Phi_\mathrm{P}\right), \tag{3.28}$$

where $\boldsymbol{\nabla}_\perp$ is the horizontal component of the gradient. As we have mentioned above, $\xi_r$, $p'$, $\rho'$ and $\Phi_\mathrm{P}$ are proportional to $Y_2^{-2}(\theta,\phi)$. However, equation (3.28) shows that this is not the case for $\boldsymbol{\xi}_h$. By introducing $V$ such that $\boldsymbol{\xi}_h \equiv r\boldsymbol{\nabla}_\perp V$, equation (3.27) becomes:

$$V = \frac{r}{\rho_0 l(l+1)}\left[\rho' + \frac{1}{r^2}\frac{\partial}{\partial r}\left(r^2\rho_0\xi_r\right)\right], \tag{3.29}$$

and equation (3.28) becomes:

$$V = \frac{1}{rm^2\omega^2}\left(\frac{p'}{\rho_0} + \Phi_\mathrm{P}\right). \tag{3.30}$$

As $V$ has the same angular dependence as the other quantities with which it is being compared, and is a scalar instead of a vector, it is much easier to use in the analysis than $\boldsymbol{\xi}_h$. We can calculate $\boldsymbol{\xi}_h$ from $V$ by using $V(r,\theta,\phi,t) = V(r)Y_2^{-2}(\theta,\phi)\mathrm{e}^{2\mathrm{i}\omega t}$, with $Y_2^{-2}(\theta,\phi) = 3\sin^2\theta\mathrm{e}^{-2\mathrm{i}\phi}$. Then $\boldsymbol{\xi}_h = r\boldsymbol{\nabla}_\perp V$ yields:

$$\boldsymbol{\xi}_h(r,\theta,\phi,t) = 6V(r)\sin\theta\mathrm{e}^{2\mathrm{i}(\omega t-\phi)}\left(\cos\theta\hat{\boldsymbol{\theta}} - \mathrm{i}\hat{\boldsymbol{\phi}}\right). \tag{3.31}$$

This can be combined with the radial displacement to give the full (complex) vector displacement as:

$$\boldsymbol{\xi}(r,\theta,\phi,t) = 3\sin(\theta)\mathrm{e}^{2\mathrm{i}(\omega t-\phi)}\left[\xi_r(r)\sin\theta\hat{\boldsymbol{r}} + 2V(r)\left(\cos\theta\hat{\boldsymbol{\theta}} - \mathrm{i}\hat{\boldsymbol{\phi}}\right)\right], \tag{3.32}$$

which shows that, when estimating contributions to the displacement vector, $V$ can be compared with $\xi_r$ up to a trigonometric factor and a factor of 2.

#### 3.2.2.2 Numerical calculation of the horizontal displacement

As a check of internal consistency, the values of $V$ calculated from equations (3.29) and (3.30) using the numerical solution of equations (2.16)–(2.19) for a Jupiter mass planet with an orbital period of 4.23 days to determine the right hand sides are compared in Figure 3.3 in the region close to the surface, for both a 1 $M_\odot$ and 1.4 $M_\odot$ stars, for the case of frozen convection. Note that $V$ is not directly specified on the grid by the numerical solution. In both cases the expressions agree very well, with the greatest discrepancy arising at the points where the magnitude of the second derivative is large, due to the numerical evaluation of the derivative in equation (3.29).

#### 3.2.2.3 An illustrative analytic estimate of $V$

An analytical estimate for $V$ can be derived through the second law of thermodynamics given by equation (2.8) and the continuity equation (3.29). The former can be adapted to read:

$$\Delta p - \frac{\Gamma_1 p_0}{\rho_0}\Delta\rho = -\frac{\mathrm{i}(\Gamma_3 - 1)}{m\omega}\boldsymbol{\nabla}\cdot\mathbf{F}'. \tag{3.33}$$

We shall assume hydrostatic equilibrium for the perturbations but non–adiabatic behaviour. This is enough to indicate significant departures from the standard equilibrium tide. Thus, making use of equations (1.18) and (1.19), we obtain:

$$(\xi_r - \xi_{r,\mathrm{eq}})\left(\frac{dp_0}{dr} - \frac{\Gamma_1 p_0}{\rho_0}\frac{d\rho_0}{dr}\right) = -\frac{\mathrm{i}(\Gamma_3 - 1)}{m\omega}\boldsymbol{\nabla}\cdot\mathbf{F}', \tag{3.34}$$

where $\xi_{r,\mathrm{eq}} = -\Phi_\mathrm{P}/g$ is the radial component of the Lagrangian displacement for the standard equilibrium tide (see section 1.3). This implies deviation from the equilibrium tide when the non–adiabatic contributions on the right hand side of equation (3.34) become important. Then we find that, for small $\omega$, $\xi_r$ scales as $|1/\omega|$. The horizontal component can be found from the continuity equation (3.29) which may be rewritten as:

$$V = \frac{r}{l(l+1)}\left(\frac{\rho'}{\rho_0} + \frac{\xi_r}{\rho_0}\frac{d\rho_0}{dr} + \frac{\partial\xi_r}{\partial r} + 2\frac{\xi_r}{r}\right). \tag{3.35}$$

In the limit that $\xi_r$ scales as $|1/\omega|$, $V$ also has that scaling and $\rho'$ may be neglected, assuming a perturbed flux given by the equilibrium tide. If the perturbed flux is not given by the equilibrium approximation, the frequency dependence is likely to be more complex.

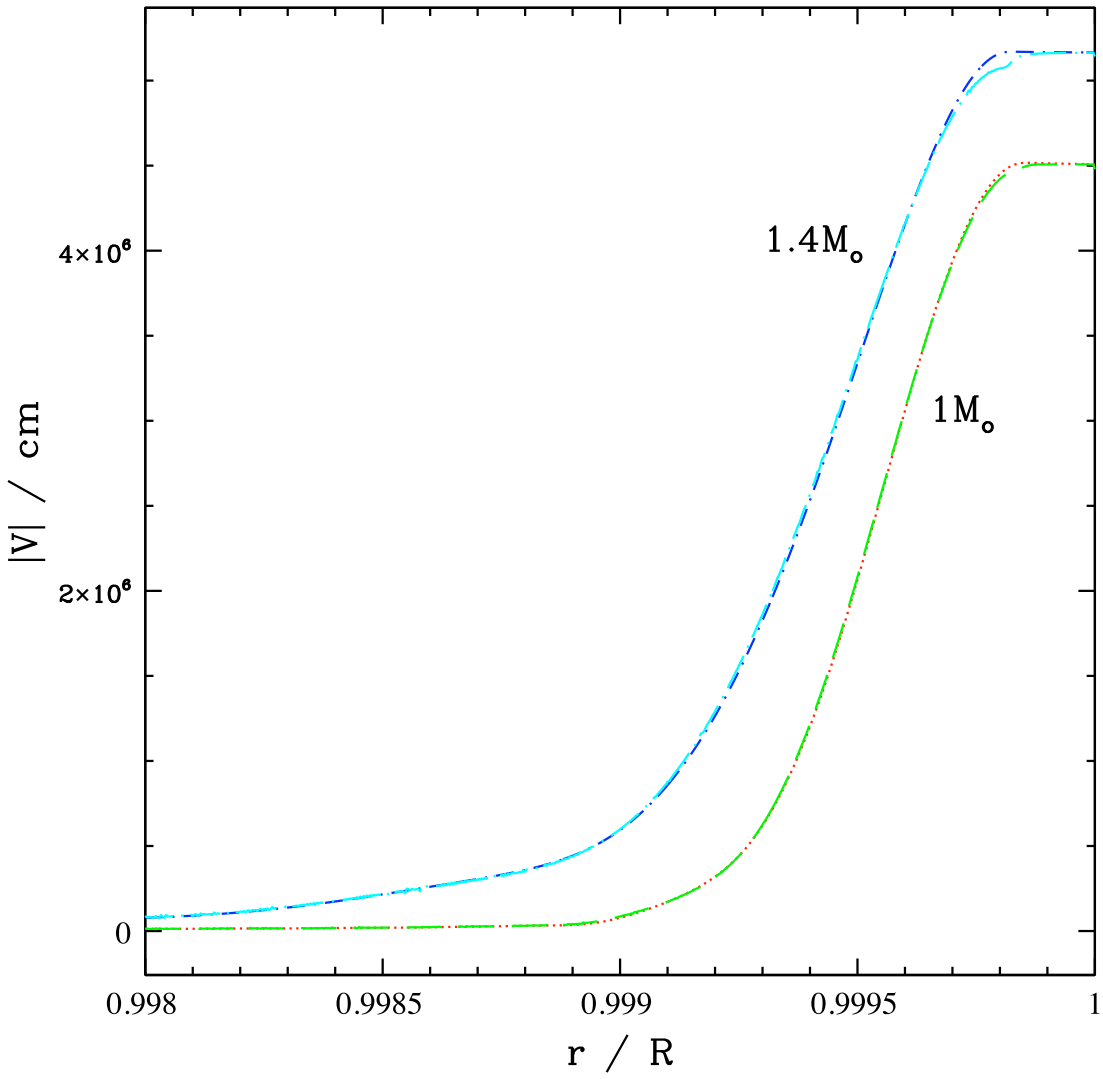


Figure 3.3: Comparison between the values of |V| given by equations (3.29) and (3.30) as a function of $r/R$ near the stellar surface for a Jupiter mass planet in a circular orbit with period 4.23 days, for the case of frozen convection. We note $V_{\rm cont}$ and $V_{\rm eom}$ the values of $V$ given by the continuity equation (3.29) and the equation of motion (3.30), respectively. The red dotted line is $|V_{\rm eom}|$ and the green dashed line is $|V_{\rm cont}|$ for the $1\,M_\odot$ case; the dark blue short dash–dot line is $|V_{\rm eom}|$ and the cyan long dash–dot line is$|V_{\rm cont}|$ for the $1.4\,M_\odot$ case. In both cases, the two expressions agree well, with some small discrepancy at points with significant curvature, due to the numerical evaluation of derivatives in the continuity equation.

As we are interested in the value of $V$ at the surface of the star, we fix $r = R$, the radius of the star. Under the assumption that $\xi_r$ varies on a scale comparable to the density scale height or larger (due to non-adiabatic behaviour causing deviation from the equilibrium tide), we obtain the expression:

$$\frac{V}{\xi_r} \approx \frac{R}{l(l+1)} \frac{1}{\rho_0} \frac{\partial \rho_0}{\partial r}\bigg|_{r=R}. \tag{3.36}$$

In order to make estimates we evaluate the scale height at $r_{\rm na}$, where here $r_{\rm na}$ stands for either $r_{\rm na,f}$ or $r_{\rm na,p}$ depending on whether convection is frozen or perturbed. The scale height actually decreases towards the surface, although by less than an order of magnitude. Therefore, adopting (3.36) with $H_\rho$, being evaluatedj at $r = r_{\rm na}$ is expected to lead to a lower bound for $|V|$, while giving an estimate of the right order of magnitude. Assuming $\xi_r$ remains the same order of magnitude as the equilibrium tide radial displacement $\xi_{r,\rm eq}$, this gives the final relation between $V$ and $\xi_{r,\rm eq}$ to the same level of accuracy as:

$$\frac{V}{\xi_{r,\rm eq}} \gtrsim \frac{R}{l(l+1)H_\rho|_{r_{\rm na}}}. \tag{3.37}$$

This suggests a large ratio $\sim 500$ which is approached in our calculations with frozen convection.

## 3.3 What does nonadiabaticity lead to?

To examine exactly what nonadiabaticity leads to, the numerical solution to the non-adiabatic stellar oscillation equations is set out in this section. The response of a star to the perturbation of a Jupiter–mass planet on a 4.23 day orbit is presented here, primarily for a 1 $M_\odot$ star, but some results are also shown for the case of a star of mass 1.4 $M_\odot$. The results are focussed on the behaviour near the surface of the star, where non–adiabatic effects become important. Throughout this section the perturbed quantities refer to their radial parts, that is, $T'$ stands for $T'(r)$. As pointed out in section 1.2, for any solved–for perturbed quantity, $q'(r)$, which is in general complex, we can form a real quantity that can be written as $q'(r,\theta,\phi,t) = \Re\left[q'(r)Y_2^{-2}(\theta,\phi)e^{2i\omega t}\right]$.

This section has been split into two parts: section 3.3.1 shows the calculation for frozen convection, i.e. under the assumption that the convective flux does not change from its background value and section 3.3.2 shows the results for perturbed convection, i.e. it is assumed that the time scale is short enough for it to relax to a quasi–steady state obtained from MLT. Similar figures have been produced in each case, but the ranges displayed have been adjusted to make the results as clear as possible.

### 3.3.1 Frozen convection

The magnitudes of the perturbed variables are shown for the full extent of the star in Figure 3.4. Within the body of the star, the response to the tidal potential agrees with previous work (Terquem et al., 1998) and oscillations are seen throughout the radiative core, becoming evanescent in the convection zone. Despite the high spatial frequency of the oscillations at the centre of the star, the peaks are still well resolved, as shown in Figure 3.5.

Figure 3.6 shows the real parts of $m\omega\xi_r$ (radial perturbed velocity) and $m\omega V$, which were plotted by Terquem et al. (1998) and therefore allow a comparison to be made. The radial and horizontal displacements are both of similar magnitude to the equilibrium radial displacement $\xi_{r,eq}$ away from the surface (which we expect, as $V_{\rm eq} \approx \xi_{r,\rm eq}$ outside the stellar core). The results shown in Figure 3.6 are in good agreement with those of Terquem et al. (1998), other than the fact that in our case $V$ continues to increase in the convection zone, more closely matching the equilibrium tide approximation (see section 1.3).

However, the surface behaviour is very different to both the equilibrium tide approximation and to the results of Terquem et al. (1998), which did not fully incorporate non–adiabatic effects. Within a thin region at the surface (of a similar width to the strongly superadiabatic convection region together with the overlying radiative zone near the surface of the star) the magnitude of the perturbations varies by orders of magnitude, as shown in Figure 3.7, where the same quantities as illustrated in Figure 3.4 are plotted over the radial range $0.998 < r/R < 1$. This is consistent with the estimated radius $r_{\rm na,f} = 0.9995R$ above which the perturbation is non–adiabatic.

In Figure 3.8, we highlight the behaviour of the radial and horizontal displacements in the surface region in units of the radial displacement predicted by the equilibrium tide approximation, $\xi_{r,\rm eq}$, for both the 1 $M_\odot$ and the 1.4 $M_\odot$ star (more details about the equilibrium tide can be found in section 1.3). At the surface, the radial displacement is suppressed by a factor of $\sim 10$ relative to the adiabatic case, and the horizontal displacement is amplified by a factor of $\sim 100$, which is similar to the estimates provided in section 3.2.2.3 and the appendices of Bunting et al. (2019). In order to investigate the effect of changing the surface boundary condition, we have rerun both the 1 $M_\odot$ case and the 1.4 $M_\odot$ case, replacing the condition $\Delta p = 0$ by the boundary condition given by Pfahl et al. (2008). Results are very similar, apart from $|\xi_r|$ attaining even smaller values at the surface. In the non–adiabatic zone, the horizontal displacement is therefore larger than the radial displacement by a factor

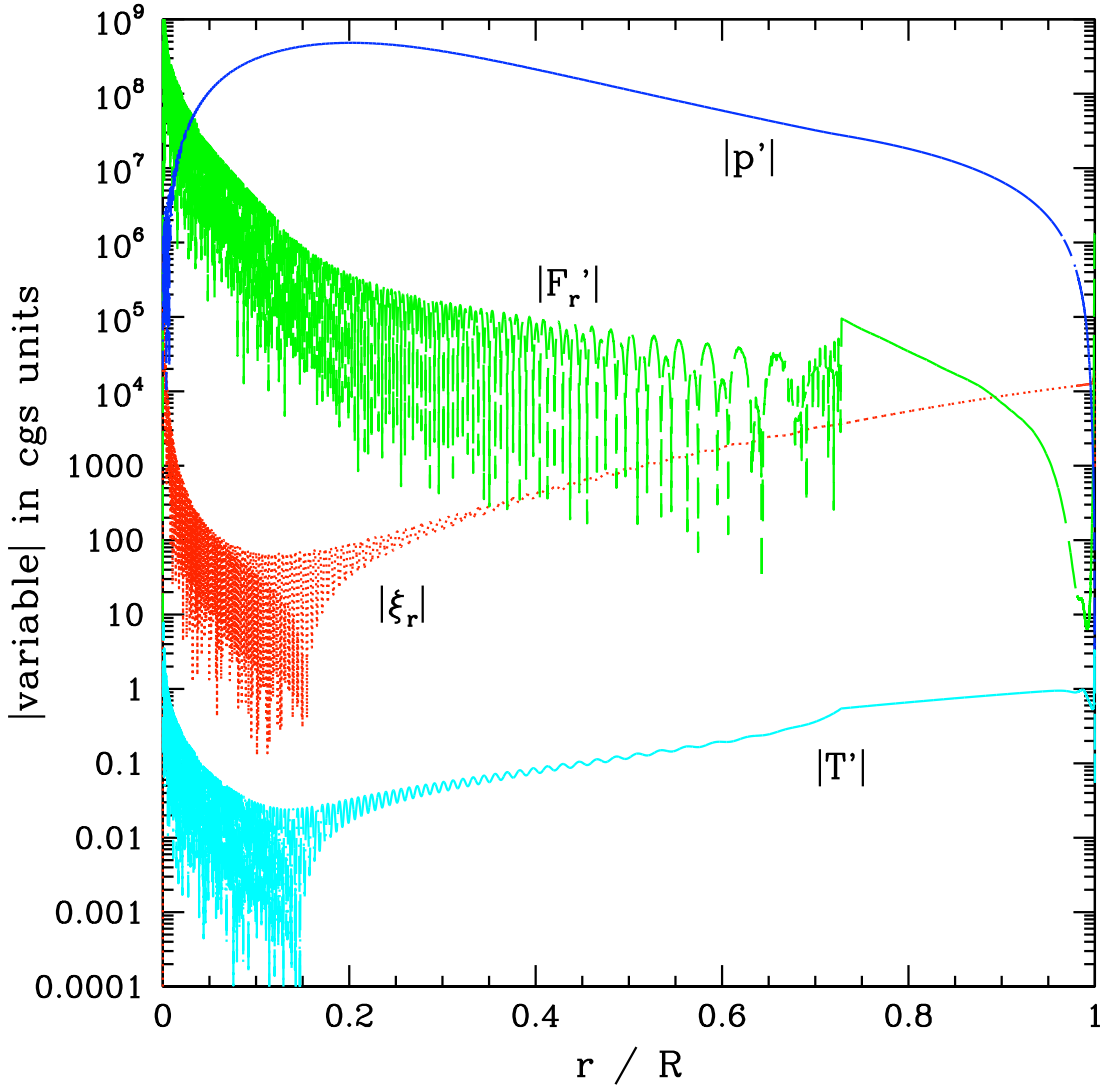


Figure 3.4: This shows, for the case of frozen convection, the magnitude of the four variables which are directly output from the code *versus* $r/R$, for the case $M = 1$ M$_\odot$: $\xi_r$, the radial displacement (red dotted line); $F_r'$, the perturbation to the radial radiative flux (green dashed line); $p'$, the perturbation to the pressure (dark blue short dash-dot line); and $T'$, the perturbation to the temperature (cyan long dash-dot line). The transition in behaviour at $r/R \sim 0.73$ is due to the onset of convection. Behaviour near the surface is examined more closely in Fig. 3.7. Except for a thin surface layer, where non–adiabatic effects are important, the imaginary part is much smaller than the real part for all of these quantities. Note that as the magnitude of quantities is shown on a logarithmic scale, unresolved minima may attain smaller values than indicated.

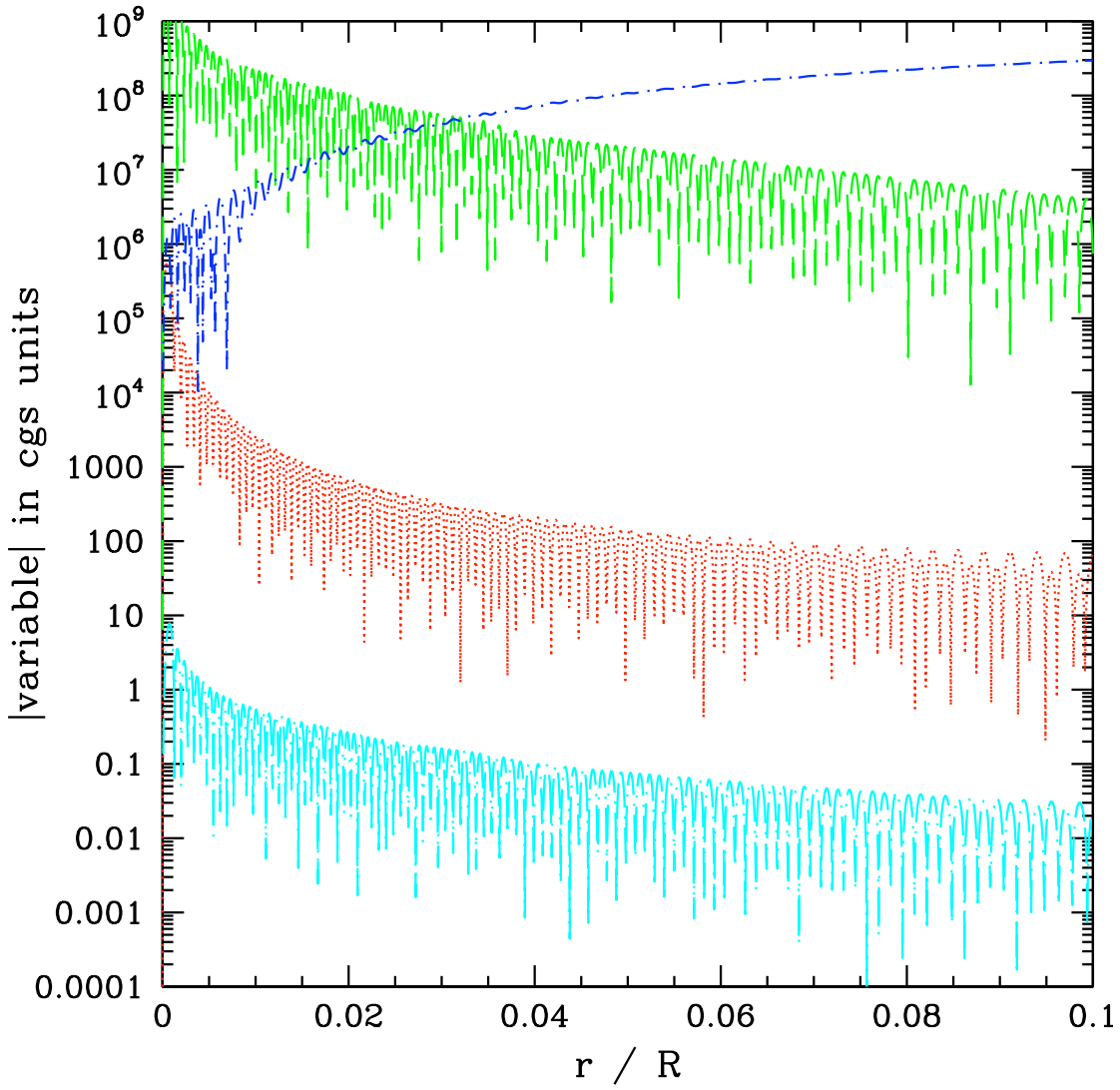


Figure 3.5: The quantities illustrated in Fig. 3.4 are plotted over a narrow radial range, $0 < r/R < 0.1$, for the 1 $M_\odot$ star, for the case of frozen convection, in order to focus on the stellar core. Shown are the magnitudes of $\xi_r$, the radial displacement (red dotted line); $F'_r$, the perturbation to the radial radiative flux (green dashed line); $p'$, the perturbation to the pressure (dark blue short dash–dot line); and $T'$, the perturbation to the temperature (cyan long dash–dot line). The high–frequency spatial oscillations are resolved well even in the core.

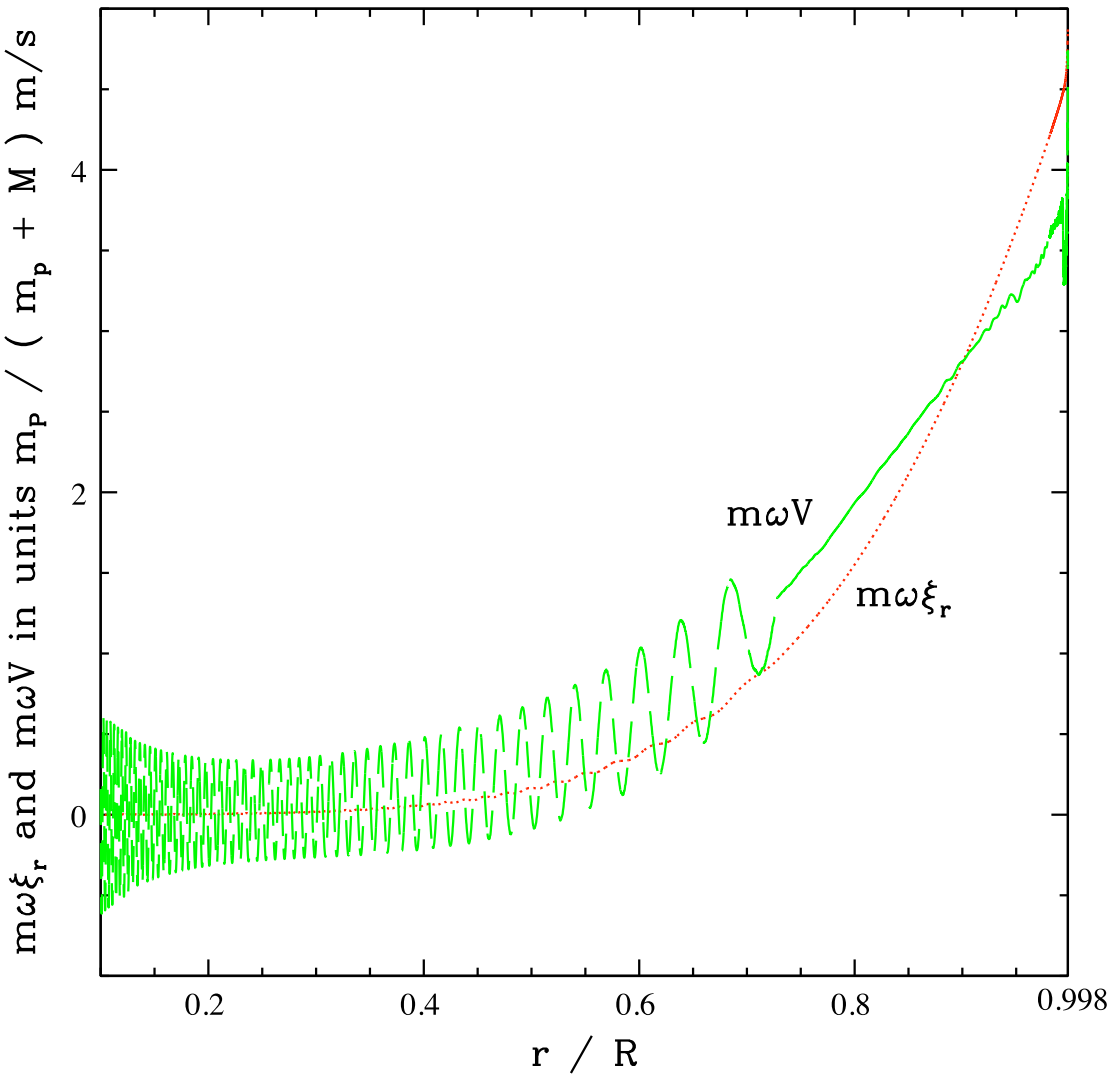


Figure 3.6: This figure shows, for the 1 $M_\odot$ case with frozen convection, the real parts of $m\omega\xi_r$ and $m\omega V$ in units of $[m_p/(m_p+M)]\,\mathrm{m\,s^{-1}}$ for $0.1 < r/R < 0.998$, thereby excluding the thin surface region where non–adiabatic effects are prominent. The red dotted line shows $m\omega\xi_r$, and the green dashed line shows $m\omega V$. The behaviour here is very similar to that shown in Terquem et al. (1998), except for the fact that in our case $V$ continues to increase within the convection region, for $r/R > 0.73$.

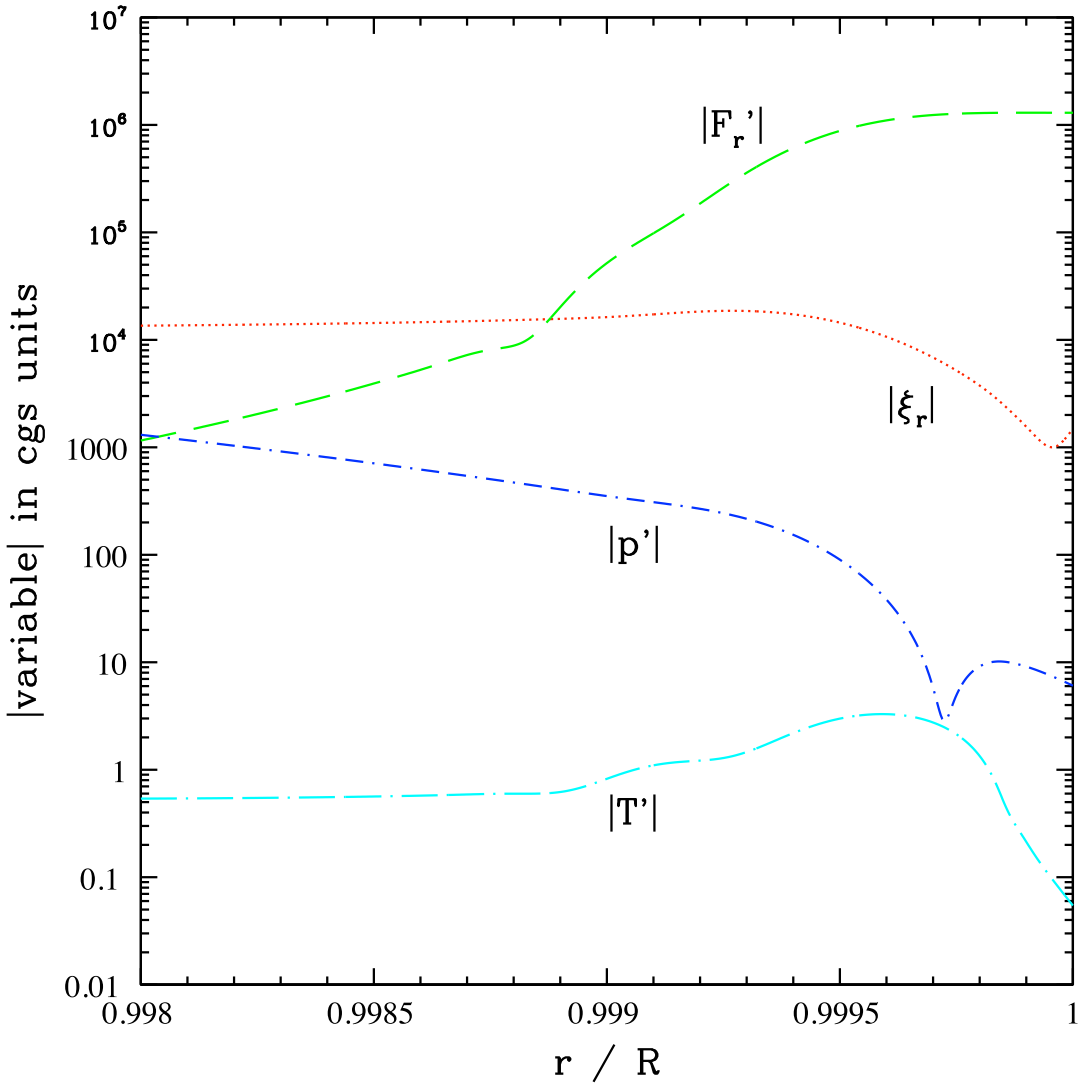


Figure 3.7: The quantities illustrated in Fig. 3.4 are plotted over a narrow radial range, $0.998 < r/R < 1$, for the 1 $M_\odot$ star, with frozen convection, in order to focus on the surface region. Note the change in the range of the $y$–axis. Shown are the magnitudes of $\xi_r$, the radial displacement (red dotted line); $F_r'$, the perturbation to the radial radiative flux (green dashed line); $p'$, the perturbation to the pressure (dark blue short dash–dot line); and $T'$, the perturbation to the temperature (cyan long dash–dot line). The amplitude of the oscillations in the uppermost 0.2% of the star changes rapidly on a small scale. In this region, the imaginary parts of the variables cannot be neglected. This is consistent with the perturbation being non–adiabatic above $r_{\rm na,f} = 0.9995R$.

of $\sim 1000$ or more. The results displayed in Figure 3.8 are consistent with departure from the equilibrium tide arising as a result of non–adiabaticity above $\sim r_{\rm na,f}$.

To illustrate the relationship between the radial and horizontal displacements, taking the angular dependence into account, Figure 3.9 displays the horizontal displacements as vectors, and the radial displacement shown through the colour. The plot displays the surface of one side of the star, covering latitudes from $-90°$ to $90°$, and longitudes from $-90°$ to $90°$ with $(0,0)$ as the sub–planetary point.

The perturbation to the flux in the surface region is shown in Figure 3.10 for both the 1 $M_\odot$ and the 1.4 $M_\odot$ cases. Throughout this region, the perturbation to the flux grows rapidly, and the phase of the perturbation changes on a small scale, highlighting the non–adiabatic nature of this response. At the surface, the imaginary component is dominant, but the real part remains non–negligible, resulting in a phase lag behind the planet of $\sim 40°$.

### 3.3.2 Perturbed convection

We present below the results corresponding to the case when the convective flux is perturbed, for both approaches A and B described in Section 3.1.2.

#### 3.3.2.1 Perturbed convection following approach A

The response throughout the whole star for the 1 $M_\odot$ star, in the case of perturbed convection following approach A, is shown in Figure 3.11. Within the radiative core, the behaviour is oscillatory, transitioning to evanescent behaviour in the convection zone. Despite the high spatial frequency towards the centre of the star, just as in the case of frozen convection described above, the oscillations remain well resolved.

The radial and horizontal displacements are displayed in Figure 3.12, which can be compared with the model shown in Terquem et al. (1998). The horizontal displacement has greater amplitude oscillations within the core, but both the radial and horizontal displacements are centred on the equilibrium tide, except at the very surface of the star.

To highlight the surface behaviour, the variables which are directly solved for are shown over a narrow radial range ($0.95 < r/R < 1$) at the surface in Figure 3.13. Over this range, the response is fairly smooth, apart from the small shifts in $\xi_r$ and $T'$ in the region of the radiative skin. In particular, $F_r'$ is approximately constant, which is expected from the condition that $\boldsymbol{\nabla}\cdot\mathbf{F} \sim 0$ in the upper non–adiabatic layers.

The radial and horizontal displacements in the surface region are shown in Figure 3.14 for a narrow radial range ($0.998 < r/R < 1$), for both the 1 and 1.4 solar

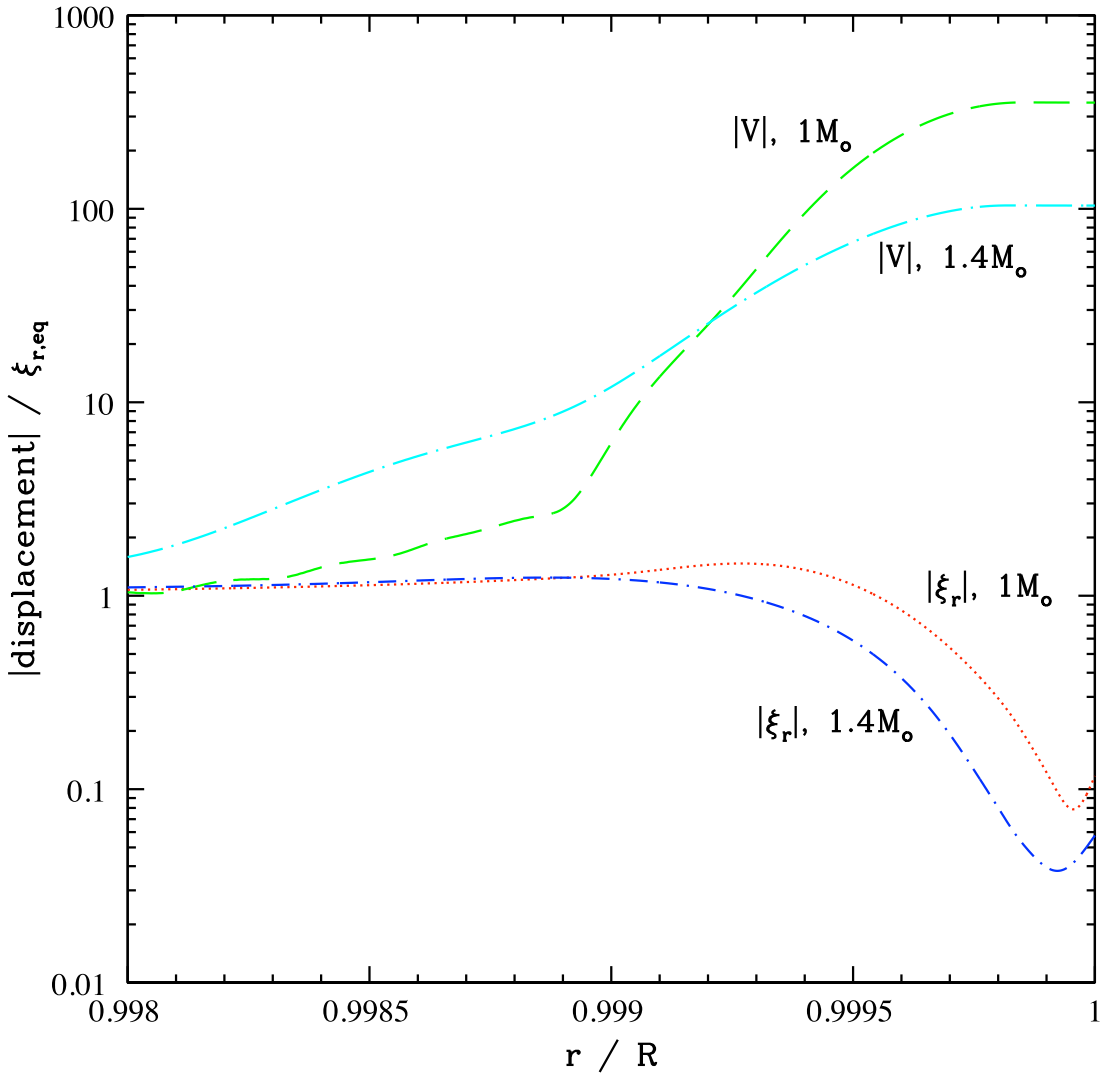


Figure 3.8: The radial and horizontal displacements in the case of frozen convection, scaled by the equilibrium tide radial displacement, $\xi_{r,\mathrm{eq}}$, (given by equation A.3) *versus* $r/R$ near the stellar surface. For the 1 $\mathrm{M}_\odot$ case, the red dotted line indicates $\xi_r/\xi_{r,\mathrm{eq}}$ and the green dashed line $V/\xi_{r,\mathrm{eq}}$; for the 1.4 $\mathrm{M}_\odot$ case, the dark blue short dash–dot line is $\xi_r/\xi_{r,\mathrm{eq}}$, and the cyan long dash–dot line is $V/\xi_{r,\mathrm{eq}}$. The radial displacement is suppressed compared to the equilibrium tide by a factor of $\sim 10$, whereas the horizontal displacement is greater than the equilibrium tide by a factor of $\sim 100$. Whilst the exact amount of suppression or enhancement is different for the two stellar models, both exhibit the same qualitative behaviour. This figure is consistent with departure from the equilibrium tide arising as a result of non–adiabaticity near the surface, although the plots indicate that non–adiabatic effects start to manifest themselves somewhat below $r_{\mathrm{na,f}}$, which is $0.9995R$ for the 1 $\mathrm{M}_\odot$ star and $0.9991R$ for the 1.4 $\mathrm{M}_\odot$ star.

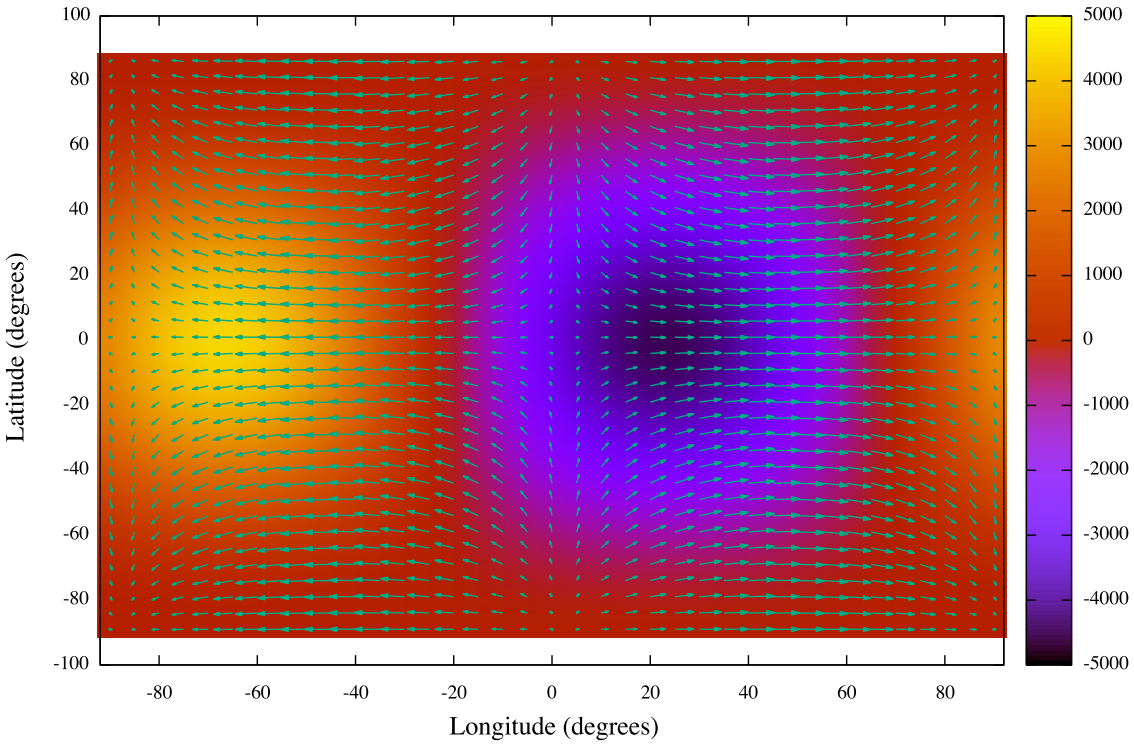


Figure 3.9: This plot illustrates the displacement vector at the surface of the star as a function of latitude and longitude for the $1M_{\odot}$ star under the assumption of frozen convection. The vectors represent the horizontal components of the displacement, magnified by a factor of 330 compared to the map, and the colour denotes the radial component of the displacement, in cm. The longitude range is $-90^{\circ}$ to $90^{\circ}$, and the sub–planetary point is at $(0,0)$, so the plot shows the visible disc of the star, as seen from the planet. Due to the non–adiabatic conditions at the surface, the tidal potential, radial displacement and horizontal displacement are all out of phase with each other. The sub-planetary point and the pattern as a whole moves to the right (increasing longitude) as time passes.

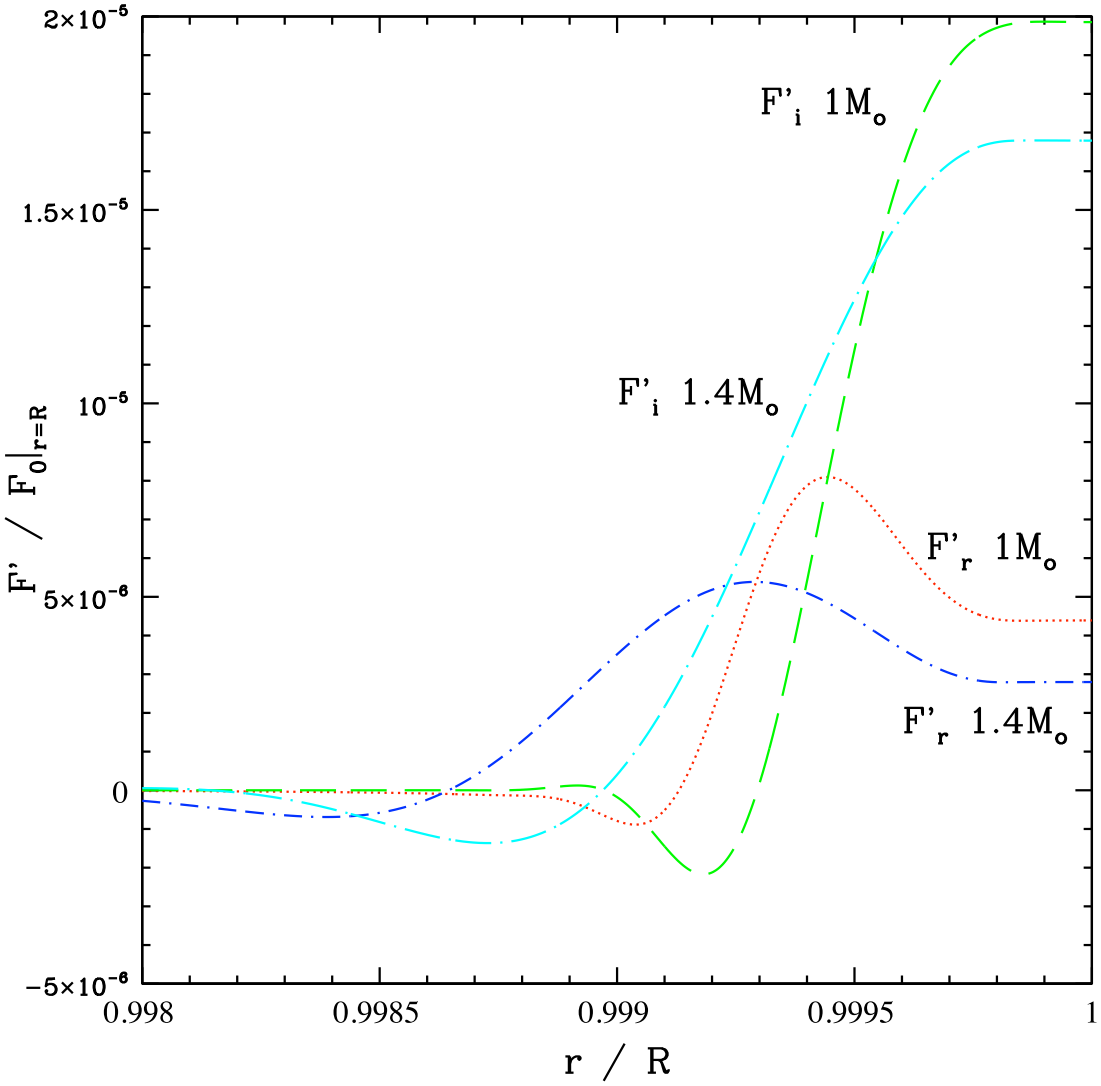


Figure 3.10: The perturbation to the radiative flux in the surface region, in units of the equilibrium flux at the surface, showing both the real and imaginary parts for both the 1 $M_\odot$ and the 1.4 $M_\odot$ stars, with frozen convection. For the 1 $M_\odot$ case, the red dotted line shows the real part, and the green dashed line the imaginary part. For the 1.4 $M_\odot$ case, the dark blue short dash–dot line shows the real part, and the cyan long dash–dot line shows the imaginary part. The imaginary parts grow rapidly in this surface layer, and dominate the perturbation to the flux at the surface, such that the peak flux will lag the planet by $\sim 40°$. The details of this behaviour differ for the two stellar masses, but both show the same qualitative behaviour and demonstrate the importance of non-adiabatic effects.

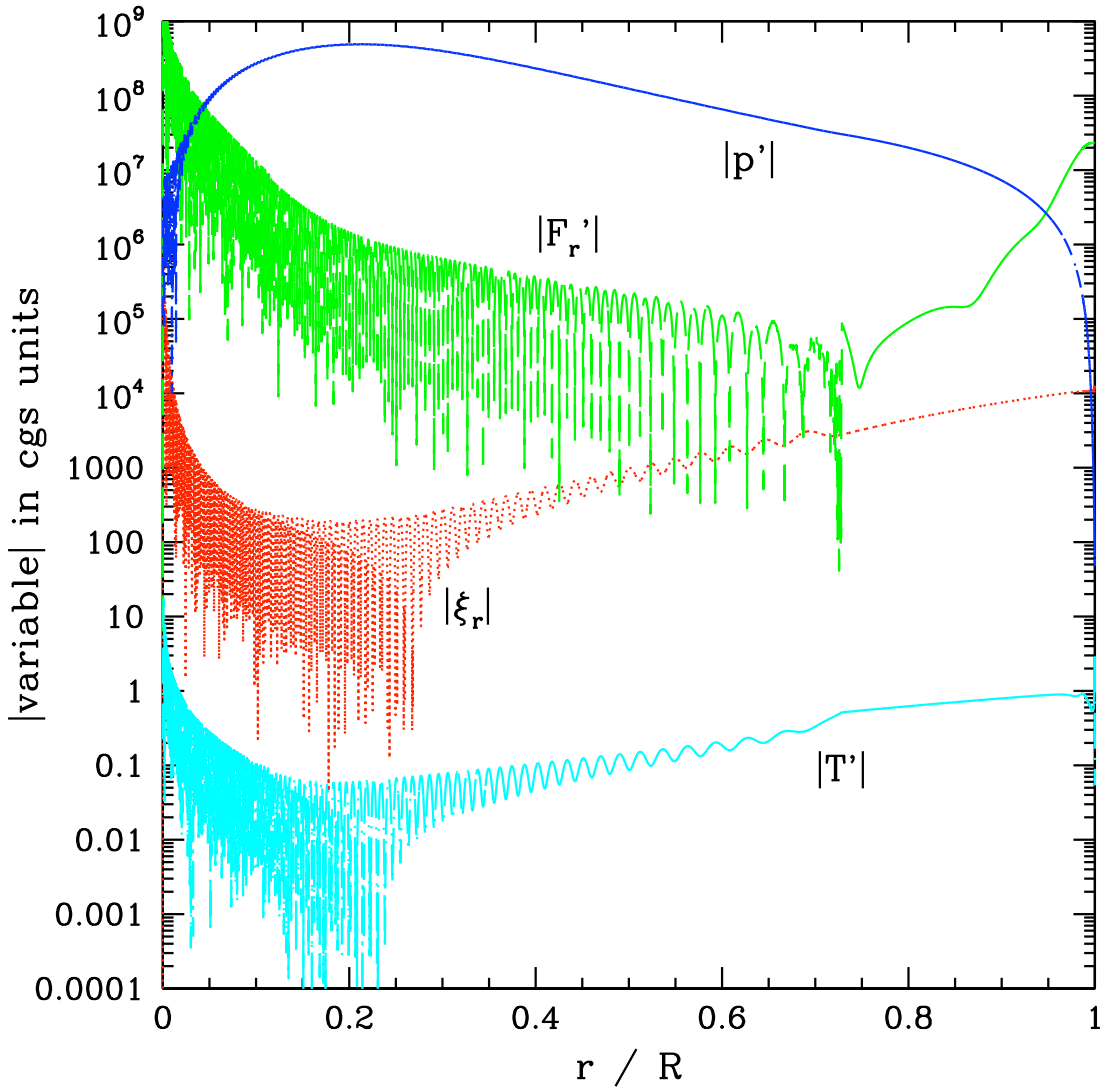


Figure 3.11: This shows, for the case of perturbed convection following approach A, for a star with $M = 1$ $M_\odot$, the magnitude of the four variables which are directly output from the code *versus* $r/R$: $\xi_r$, the radial displacement (red dotted line); $F_r'$, the perturbation to the radial energy flux (green dashed line); $p'$, the perturbation to the pressure (dark blue short dash-dot line); and $T'$, the perturbation to the temperature (cyan long dash-dot line). The transition in behaviour at $r/R \sim 0.73$ is due to the onset of convection. Behaviour near the surface is examined more closely in Fig. 3.13.

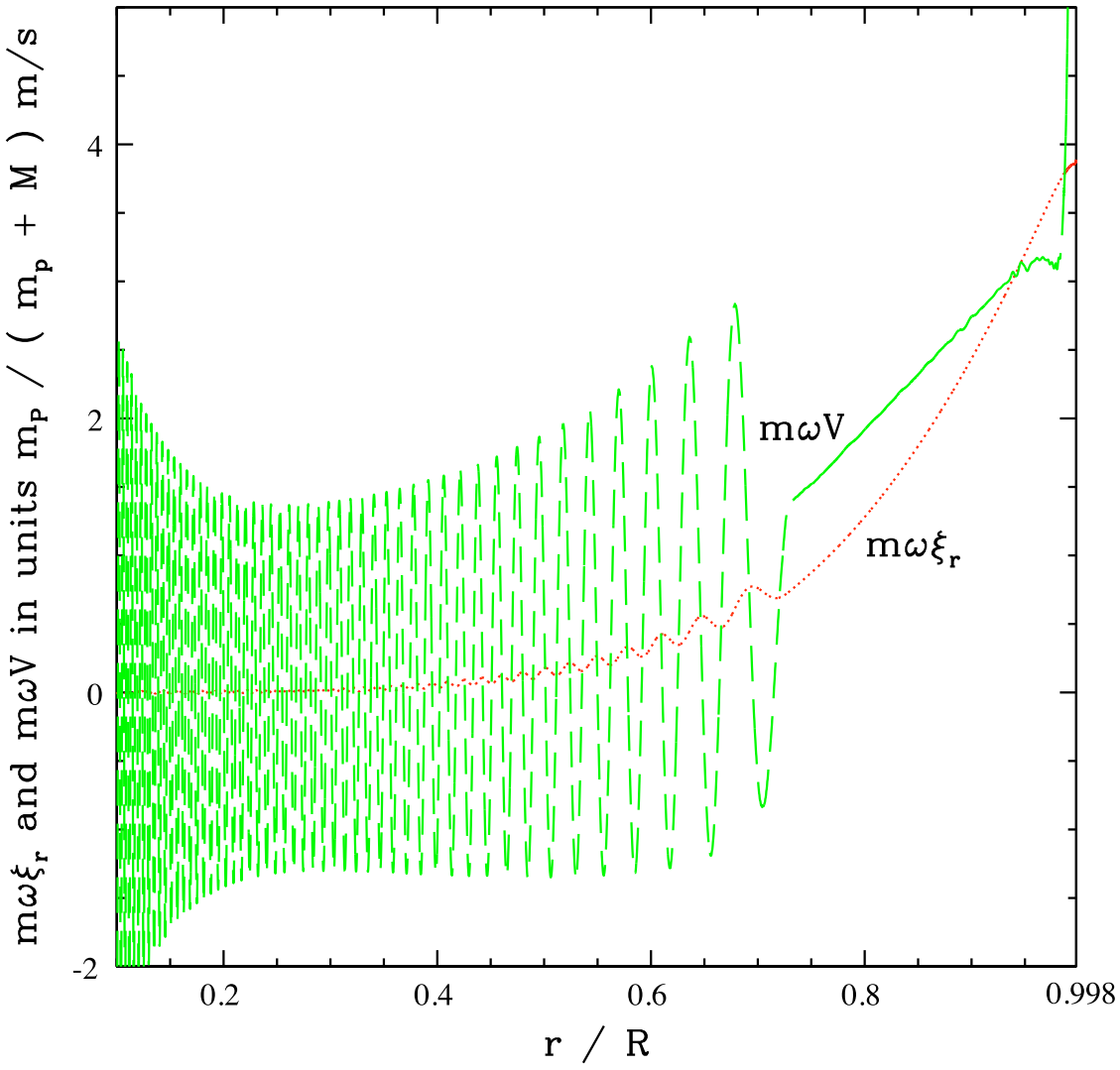


Figure 3.12: This figure shows, for the case of perturbed convection following approach A, for a star with mass $M = 1\ \mathrm{M}_\odot$, the real parts of $m\omega\xi_r$ and $m\omega V$ in units of $[m_p/(m_p+M)]\,\mathrm{m\,s^{-1}}$ for $0.1 < r/R < 0.998$, thereby excluding the thin surface region where non–adiabatic effects are most prominent. The red dotted line shows $m\omega\xi_r$, and the green dashed line shows $m\omega V$. The behaviour here is similar to that shown in Terquem et al. (1998), except for the fact that in our case $V$ continues to increase within the convection region, for $r/R > 0.73$.

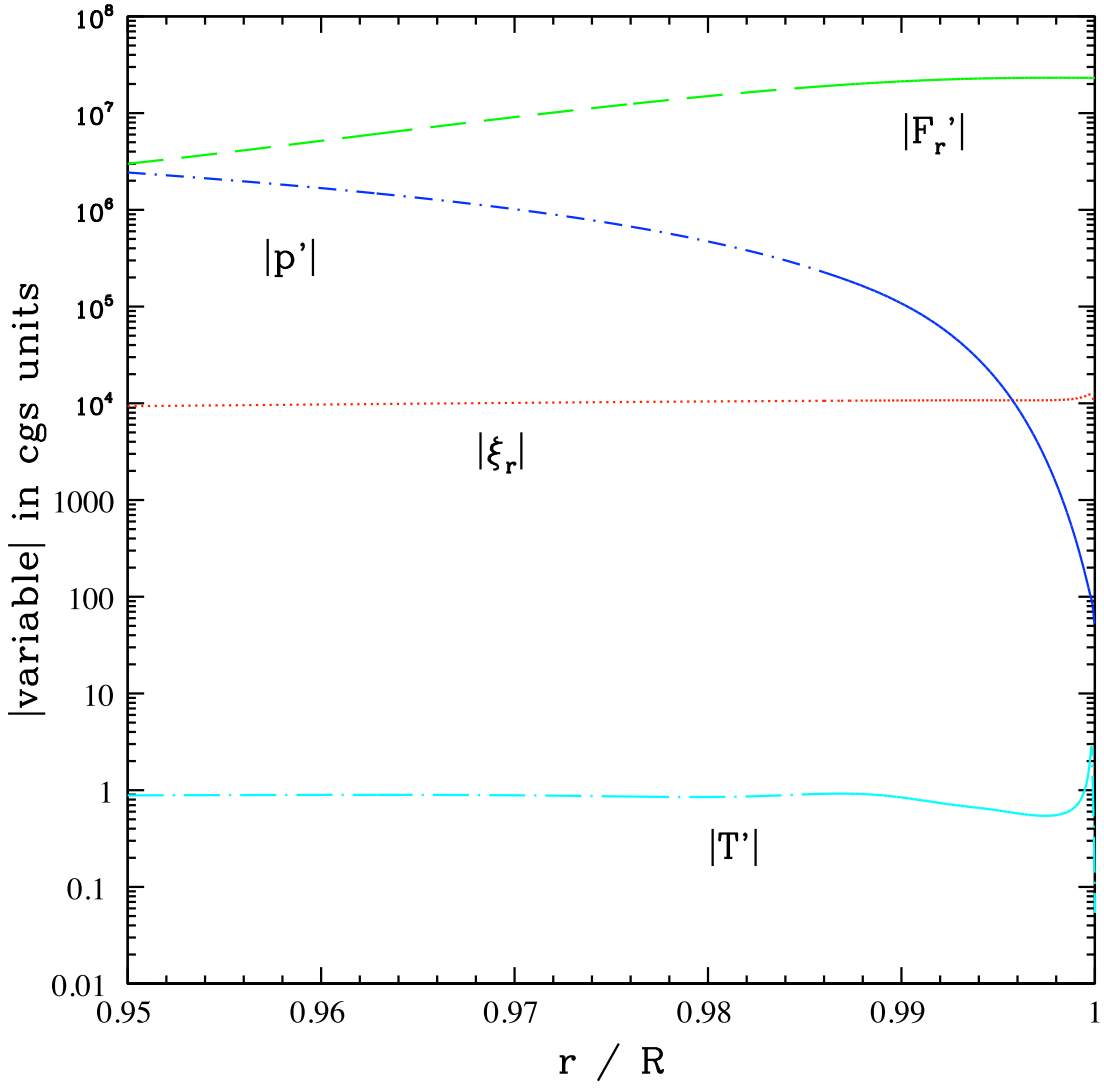


Figure 3.13: The quantities illustrated in Fig. 3.11 are plotted over a narrow radial range, $0.998 < r/R < 1$, for the 1 $M_\odot$ star with perturbed convection following approach A, in order to focus on the surface region. Note the change in the range of the $y$–axis. Shown are the magnitudes of $\xi_r$, the radial displacement (red dotted line); $F_r'$, the perturbation to the radial energy flux (green dashed line); $p'$, the perturbation to the pressure (dark blue short dash–dot line); and $T'$, the perturbation to the temperature (cyan long dash–dot line).

mass stars. The radial displacements remain close to the equilibrium tide values, with small dips at the very surface. These features in $\xi_r$ at the surface correspond to much larger changes in $V$.

Compared to the equilibrium tide, $\xi_r$ at the surface is changed by $\sim 10\%$ for the 1 $M_\odot$ star, and by a factor of 2 for the 1.4 $M_\odot$ star. The horizontal displacement at the surface is a factor of $\sim 30$ greater than the equilibrium tide value for the 1 $M_\odot$ star, and a factor of $\sim 100$ greater for the 1.4 $M_\odot$ star. These values are smaller than in the case of frozen convection.

The location at which $V$ deviates from the equilibrium tide differs in the two mass cases, with the 1.4 $M_\odot$ star showing deviations deeper in the convection zone than the 1 $M_\odot$ star, as seen in Figure 3.15. For the 1 $M_\odot$ star, these deviations originate from around $r = 0.99R$ which is intermediate between $r_{\rm na,p} = 0.97R$ and $r_{\rm na,p1} = 0.998R$ and therefore are most likely due to non–adiabaticity (see discussion in section 3.2.1.2). For the 1.4 $M_\odot$ star, $r_{\rm na,p} = 0.94R$, and the inner edge of the convection zone is at $0.93R$. There is therefore only a narrow layer at the the bottom of the convection zone where the perturbation is adiabatic if $r_{\rm na,p}$ defines the transition. However, in the innermost part of the convection zone there is a region where $|N^2|$ is small and comparable to $m^2\omega^2$ (as shown in Figure 3.2). In Bunting et al. (2019) it is argued that the standard equilibrium tide does not apply in this limit, although it can be argued that when both these quantities are zero, fractional deviations of $\xi_r$ from the equilibrium tide are of order $H_p/r$, which are relatively small here. It may be that the departure from equilibrium tide observed for the 1.4 $M_\odot$ star is due to a combination of these effects and non–adiabatic effects.

The phase relations of the displacement components are indicated in Figure 3.16 for the 1 $M_\odot$ case, showing that the phase difference between both the radial and horizontal components with respect to the planet's orbit is small.

The perturbation to the radial component of the energy flux is displayed in Figure 3.17, showing the growth in $F'$ towards the surface for both stellar masses. In both cases, the imaginary components are of similar size to the real components and cannot be neglected, which shows that non–adiabatic effects are important in this region and result in the phase changing rapidly. In both cases, the plots are consistent with significant perturbations arising in the non–adiabatic regions above $r_{\rm na,p}$.

Whether convection is perturbed using approach A or B, it is found that the radial convective flux perturbation attains an almost constant magnitude in the outer parts of the non–adiabatic zone where the perturbed radiative flux is still negligible. The magnitude of this constant can be estimated by assuming that it can be determined

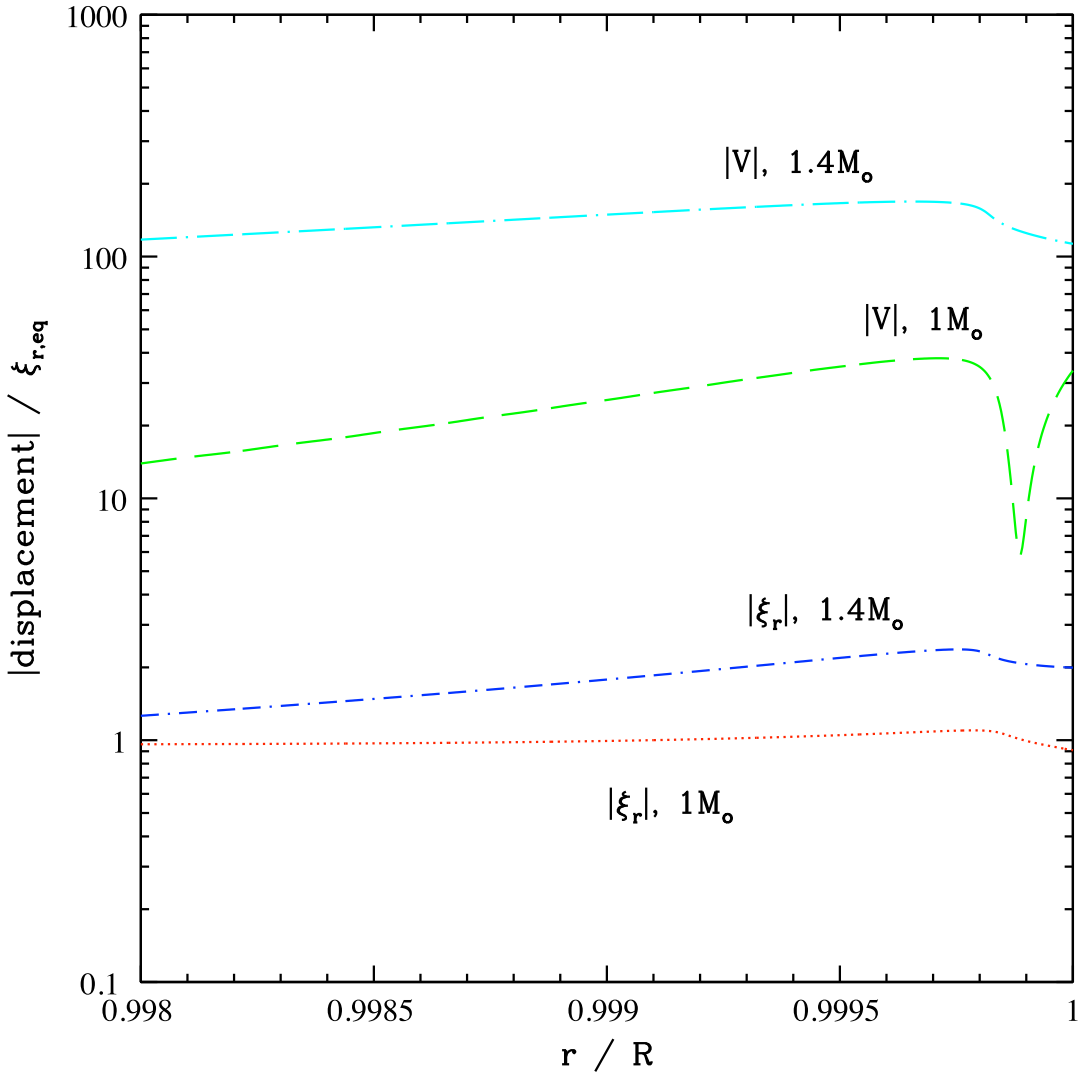


Figure 3.14: The radial and horizontal displacements, scaled by the equilibrium tide radial displacement $\xi_{r,\mathrm{eq}}$, (given by equation A.3) *versus* $r/R$ near the stellar surface, assuming perturbed convection following approach A. For the case of $M = 1$ M$_\odot$, the red dotted line indicates $\xi_r/\xi_{r,\mathrm{eq}}$ and the green dashed line $V/\xi_{r,\mathrm{eq}}$; for the 1.4 M$_\odot$ case, the dark blue short dash–dot line is $\xi_r/\xi_{r,\mathrm{eq}}$, and the cyan long dash–dot line is $V/\xi_{r,\mathrm{eq}}$. The radial displacements remain close to the equilibrium tide values, whereas the horizontal displacements are greater than the equilibrium tide values by a factor of $\sim 30-100$. Whilst the exact behaviour is different for the two stellar models, both exhibit the same qualitative behaviour.

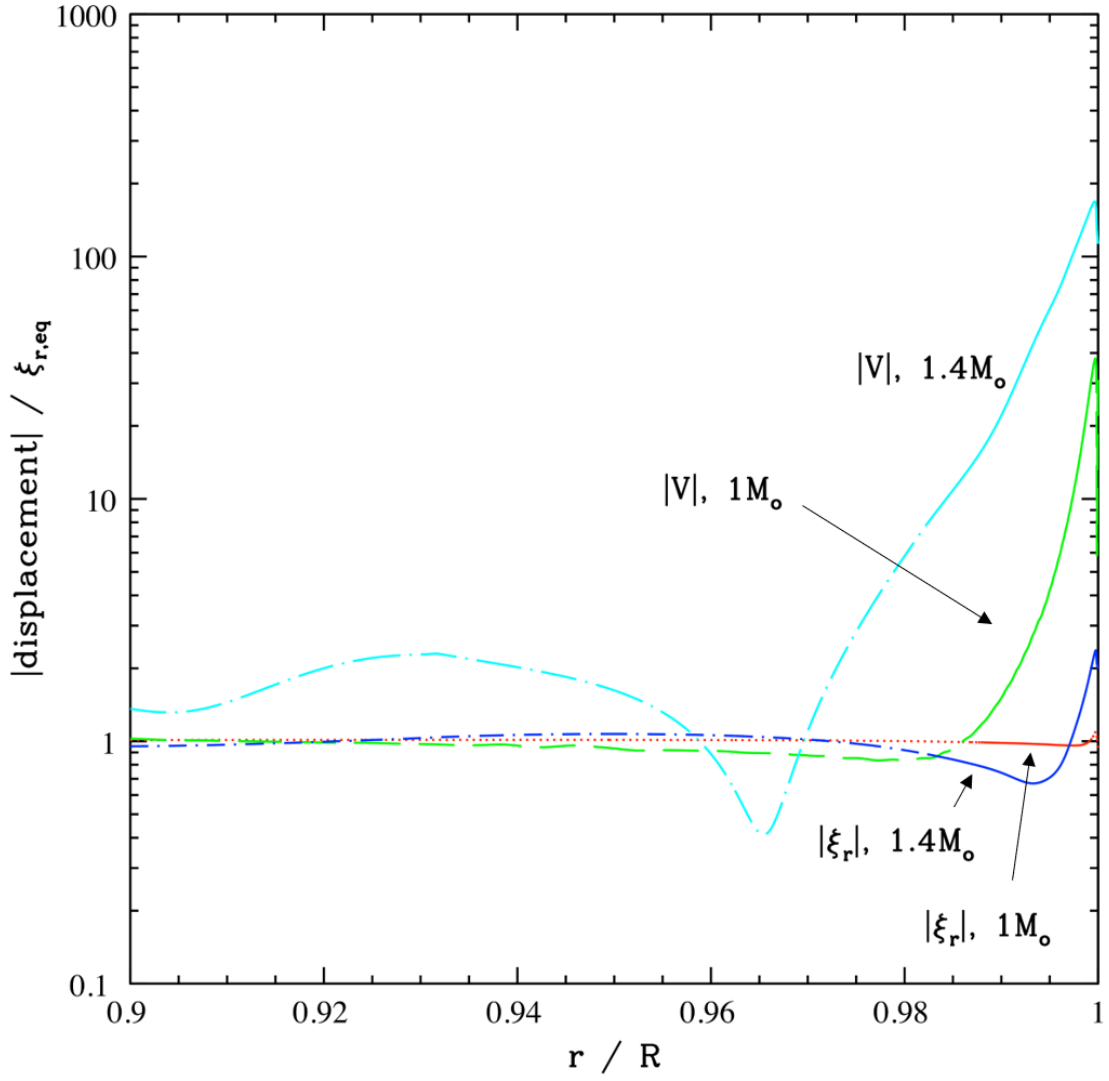


Figure 3.15: Same as Figure 3.14 but over a greater radial extent of the star, showing the departure from the equilibrium tide value. For both stellar masses, the horizontal displacement departs from the equilibrium tide value deeper than the radial displacement. Departure from equilibrium tide for $V$ is due to non–adiabaticity above $r \sim 0.99R$ for the 1 $M_\odot$ star and $0.94R$ for the 1.4 $M_\odot$ star. In the higher mass case, there may be an additional contribution from below $r_{\mathrm{na,p}}$, where the perturbation is adiabatic, due to $m^2\omega^2$ being, although small, larger than $|N^2|$ (see appendix C of Bunting et al. (2019)).

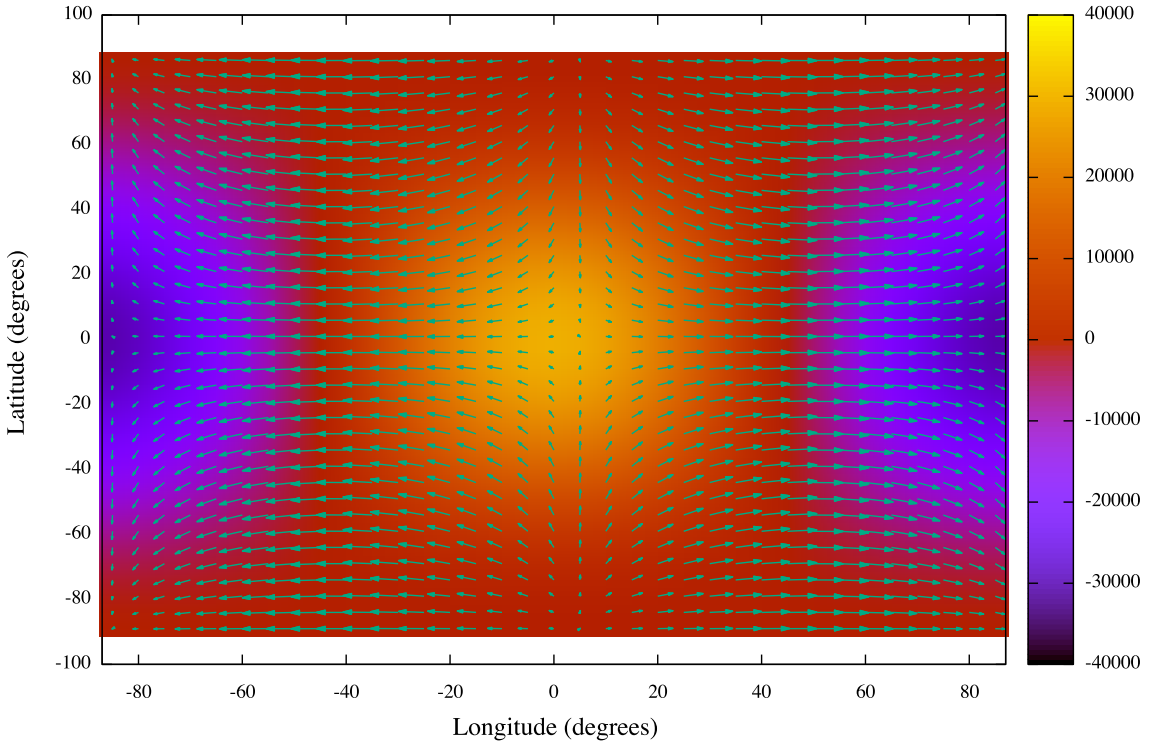


Figure 3.16: This plot illustrates the displacement vector at the surface of the star as a function of latitude and longitude for the $1M_{\odot}$ star, for the case of perturbed convection following approach A. The vectors represent the horizontal components of the displacement, magnified by a factor of 3400 compared to the map, and the colour denotes the radial component of the displacement, in units of cm. The longitude range is $-90°$ to $90°$, and the sub–planetary point is at $(0,0)$, so the plot shows the visible disc of the star, as seen from the planet. As the real parts of the displacements dominate at the surface, the radial and horizontal displacements are in phase with each other, and the planet.

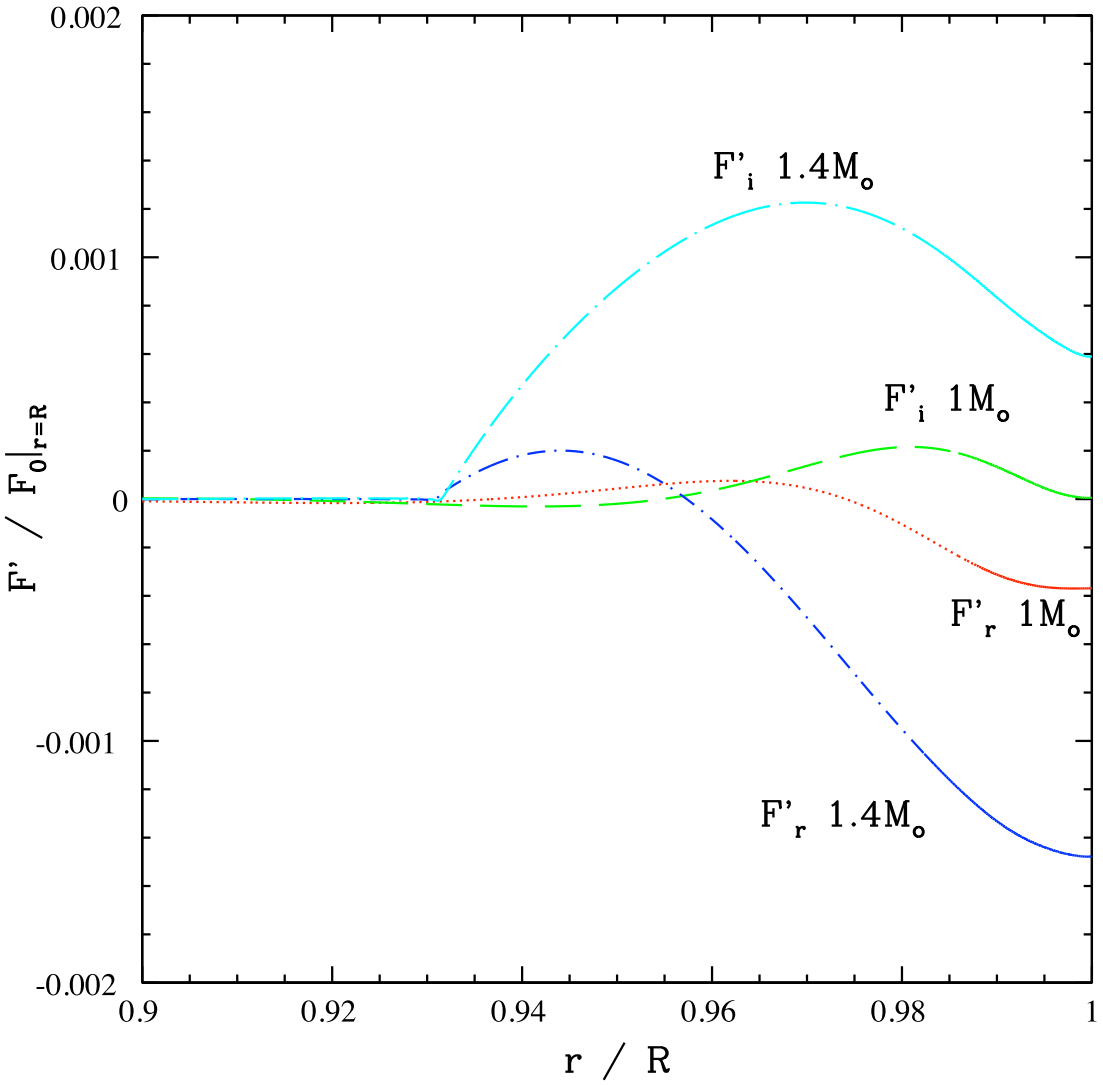


Figure 3.17: The perturbation to the radial component of the energy flux in the outer region of the star, in units of the equilibrium flux at the surface, showing both the real and imaginary parts for both the 1 $M_\odot$ and the 1.4 $M_\odot$ stars, with perturbed convection following approach A. For the 1 $M_\odot$ case, the red dotted line shows the real part, and the green dashed line the imaginary part: significant perturbations occur well before the radiative skin of the star reaching a roughly constant value around $r/R \sim 0.99$. For the 1.4 $M_\odot$ case, the dark blue short dash–dot line shows the real part, and the cyan long dash–dot line shows the imaginary part. The details of this behaviour differ for the two stellar masses, but both demonstrate the importance of non–adiabatic effects through the behaviour of the complex phase.

from the perturbed convective flux for $r$ below but not far from $r_{\rm na,p}$, where it can be assumed that the equilibrium tide applies. To illustrate this we compare the perturbed flux in the convective zone to an estimate for the perturbation to the convective flux which would arise in the case that the behaviour is non-adiabatic, and that the radial displacement is given by the equilibrium tide. We evaluate the perturbation to the flux using approach A, in the case that $\Delta s = 0$ and $\xi_r = \xi_{r,\rm eq}$. Combining this with equation 3.12 gives $F'_{\rm c,eq} = -A\frac{\partial}{\partial r}\left(-\xi_{r,\rm eq}\frac{\partial s_0}{\partial r}\right)$.

These are shown in Figure 3.18, where we plot both the ratio of the magnitude of the radial component of the energy flux perturbation to the surface background value, $|F'/F_0|_{r=R}|$, evaluated using approach A for the perturbed convective flux, and the ratio of the magnitude of the perturbed convective flux, evaluated assuming the equilibrium tide, to the background surface value of the flux, $|F'_{\rm c,eq}/F_0|_{r=R}|$, for the 1 $M_\odot$ star. The left hand panel shows the interval $0.75 < r/R < 0.9998$. A plot comparing these quantities in the non–adiabatic region very close to the surface is shown in the right hand panel. We expect the radiative flux to become significant at the radius $r_{\rm na,f}$ calculated assuming frozen convection, which is $0.9995R$ for the 1 $M_\odot$ star (below $r_{\rm na,f}$, convection is the dominant mode of transport of energy, whether convection is frozen or perturbed). Therefore, the perturbed radiative flux is negligible throughout the range plotted (except very close to the outer edge), so that $F' \simeq F'_{\rm c}$. As can be seen from the left hand panel, the perturbed convective flux constructed from the equilibrium tide does indeed track the perturbed total flux throughout the range plotted. We do not expect the match to be perfect, even below $r/R = 0.97$ where the perturbations are adiabatic, because in this region $|N^2| < m^2\omega^2$ and therefore there is departure from the equilibrium tide (see appendix C of Bunting et al. (2019)). Above $r/R \sim 0.98$ or so, we have $|N^2| \gg m^2\omega^2$ and therefore the convective timescale, over which flux perturbations are smoothed out, is much shorter than the period of the oscillations. In this regime, the perturbed convective flux is approximately constant, as seen in the right hand panel. Although this flux is not strictly constant all the way down to the base of the non–adiabatic region , we see from the the right hand panel that the variations are within a factor 2 only. Just below $r_{\rm na,p}$, the perturbations are adiabatic and therefore the equilibrium tide gives a reasonable estimate, within a factor 5 or so, as can be seen from the figure. Therefore, making the crude approximation that the equilibrium tide approximation holds at $r_{\rm na,p}$ and that the perturbed convective flux is constant above this value of $r$, we can get an estimate of the magnitude of this constant which is correct to within an order of magnitude. This indicates that the magnitude of the perturbed flux may

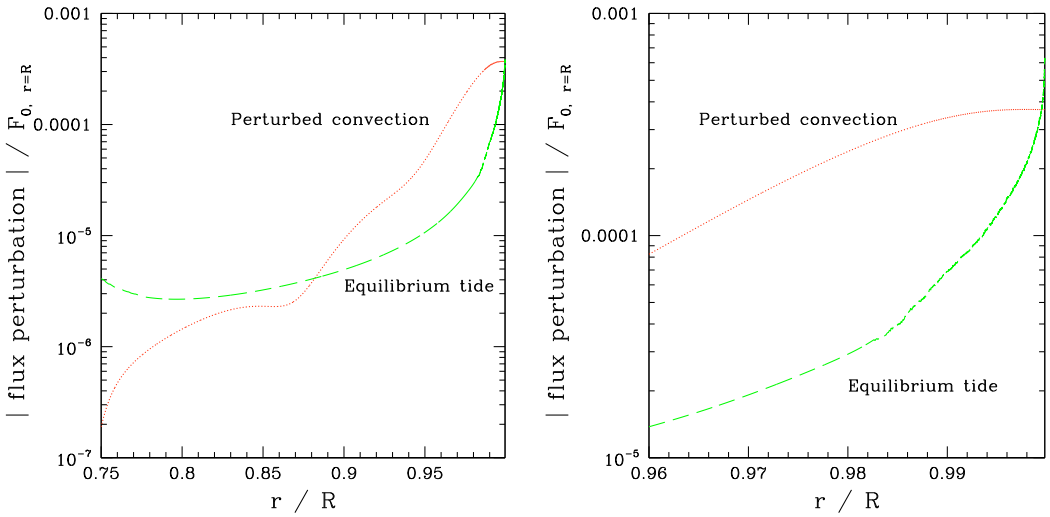


Figure 3.18: The ratio of the magnitude of the radial component of the energy flux perturbation to the surface background value, $|F'/F_0|_{r=R}|$, evaluated using approach A for the perturbed convective flux (dotted red line) and the ratio of the magnitude of the radial component of the perturbed convective flux, evaluated assuming the equilibrium tide, to the surface background value of the flux, $\left|F'_{c,eq}/F_{,0}|_{r=R}\right|$ (dashed green line), for the 1 $M_\odot$ star. The left hand panel shows these quantities for $0.75 < r/R < 0.9998$, and the right hand panel shows them for $0.96 < r/R < 0.9998$ where radiation becomes the dominant energy transport method in the background model.

be understood in a simplified way without reference to the actual components of the Lagrangian displacement, and enables us to check that the numerical values of the convective flux we obtain are correct.

#### 3.3.2.2 Perturbed convection following approach B

Above we have described results for perturbed convection following approach A, for which $A$ in equation (3.10) is unperturbed. We have also performed calculations following approach B in which variations of $A$ are included. These variations include perturbations to the state variables and the convective velocity but not the ad hoc parameters in the MLT Salaris & Cassisi (2008). The results we obtain are similar to those found following procedure A, although details vary. To illustrate this, we show the behaviour of $|F'/F_0|_{r=R}$ for the two calculations in the left hand panel of Figure 3.19 in the range $0.9 < r/R < 1$ for the 1 $M_\odot$ star. In addition, we show $|V|/\xi_{r,eq}$

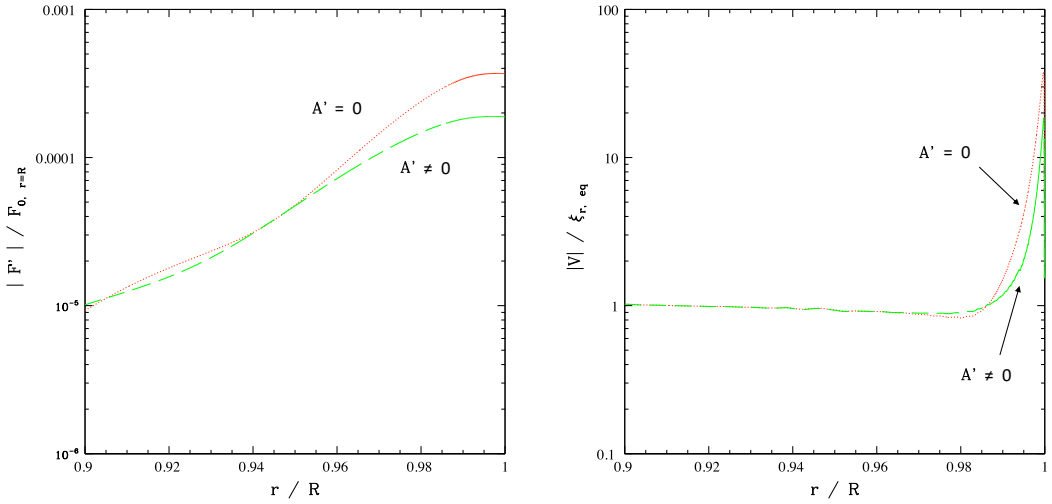


Figure 3.19: $|F'/F_0|_{r=R}|$ (left hand panel) and $|V|/\xi_{r,\mathrm{eq}}$ (right hand panel) *versus* $r/R$ in the range $0.9 < r/R < 1$ for the calculations with perturbed convection for both approach A (red dotted curves) and approach B (green dashed curves) for the 1 $M_\odot$ star.

for the same region in the right hand panel. The results are seen to be qualitatively similar with differences of about a factor of two at $r = R$.

### 3.3.3 Resonance Survey

As indicated in section 1.1, $g$–modes are largely confined to the radiative core and are expected to be excited by the tidal perturbation. Being restricted to the region where they are, to a good approximation, adiabatic and relatively free from dissipation, we expect resonances to be prominent. In order to illustrate these, we perform a resonance survey by calculating the response of a 1 $M_\odot$ star over a fine grid of orbital frequencies spanning the interval $[0.984\omega_0, 1.016\omega_0]$ where $2\pi/\omega_0$ corresponds to the orbital period of 4.23 days for which the calculations presented above were performed. The calculations presented in this section are done for the perturbed convection case using approach A. The kinetic energy of the oscillation is plotted as a function of frequency in Figure 3.20. Resonance spikes in which this quantity increases by up to five orders of magnitude, indicating a high quality factor, are clearly visible. The frequency separation is uniform, as expected for high order $g$–modes, with an interval $\delta\omega_0/\omega_0 \sim 0.005$, indicating an order $\sim 200$.

Snapshots of the response obtained during the resonance search are presented in Figure 3.21. The function $V$ is shown as a function of $r$, both in the region containing the radiative core and in the non adiabatic surface layers, for the forcing frequency

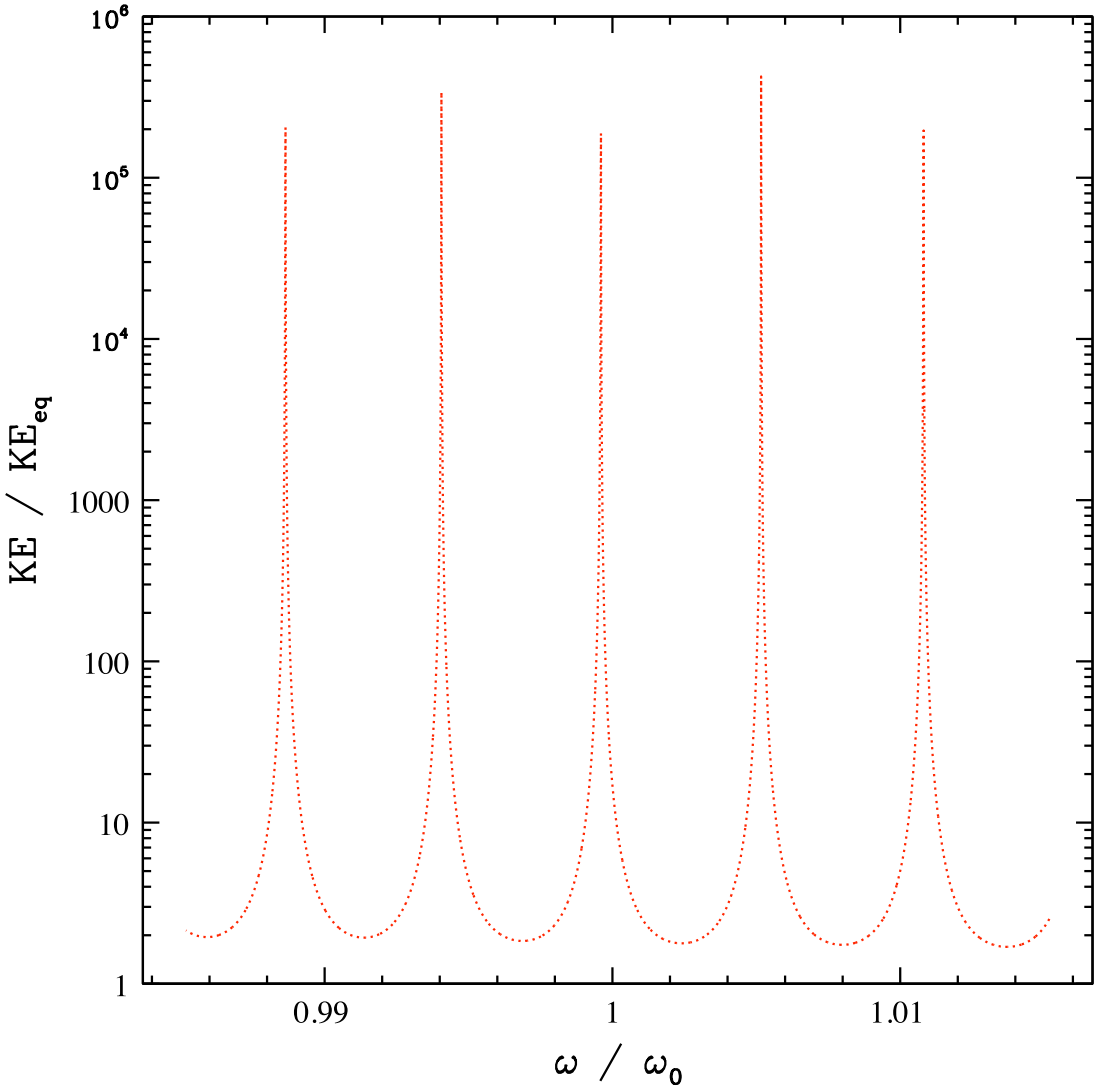


Figure 3.20: This shows the kinetic energy of the oscillation divided by the value corresponding to the equilibrium tide as a function of orbital frequency for a narrow band of frequencies in the neighbourhood of $\omega_0$, with $2\pi/\omega_0$ corresponding to an orbital period of 4.23 days. The forcing frequency is twice the orbital frequency. Prominent resonant spikes are clearly visible. This is for a 1 $M_\odot$ star.

$2\omega_0$, which corresponds to the orbital period of 4.23 days, and a close by forcing frequency of $1.99965\omega_0$, which corresponds to the centre of the nearest resonance. In the latter case, the resonantly excited $g$–mode that is confined to the radiative core can be clearly seen. However, the behaviour of $V$ close to the surface is hardly affected by this, indicating that for the most part the response outside of the radiative core is robust and unaffected by internal resonances.

## 3.4 Discussion: what difference does nonadiabaticity make?

We now discuss the impact that including non-adiabatic effects has on the response of the star, particularly towards the stellar surface. The different approaches used to model the non-adiabatic effects are compared and contrasted, and the most significant results are highlighted.

The behaviour throughout the body of the star (shown in Figures 3.4 and 3.11) largely agrees with previous work, in that the response is oscillatory in the radiative core and evanescent in the convection envelope. In the interior, away from a $g$–mode resonance, the radial displacement follows the expectation from the equilibrium tide approximation well, oscillating around the equilibrium tide value. It may be reasonable to use the equilibrium tide approximation if the average response of the stellar interior is of interest.

Bearing in mind the considerable uncertainties involved in modeling convection, we considered two extreme treatments. Following a MLT approach, we considered the case when the convection was unresponsive and frozen during perturbation and the opposite limit when it was assumed to respond on a time scale short compared to the inverse forcing frequency and so attain a relaxed state. In the latter case, we considered two approaches. In the first, only the entropy gradient was perturbed while the state variables and convective velocity were held fixed. In the second approach, these were allowed to vary. For all of the treatments of convection, the behaviour in the surface region diverges from the expectation from the equilibrium tide approximation. The horizontal displacement greatly increases, and is coupled with a change in the perturbed energy flux.

This is the consequence of the importance of non–adiabatic effects, which are not consistent with the requirements for the standard equilibrium tide to be valid. This is because hydrostatic equilibrium implies zero Lagrangian perturbations to the density

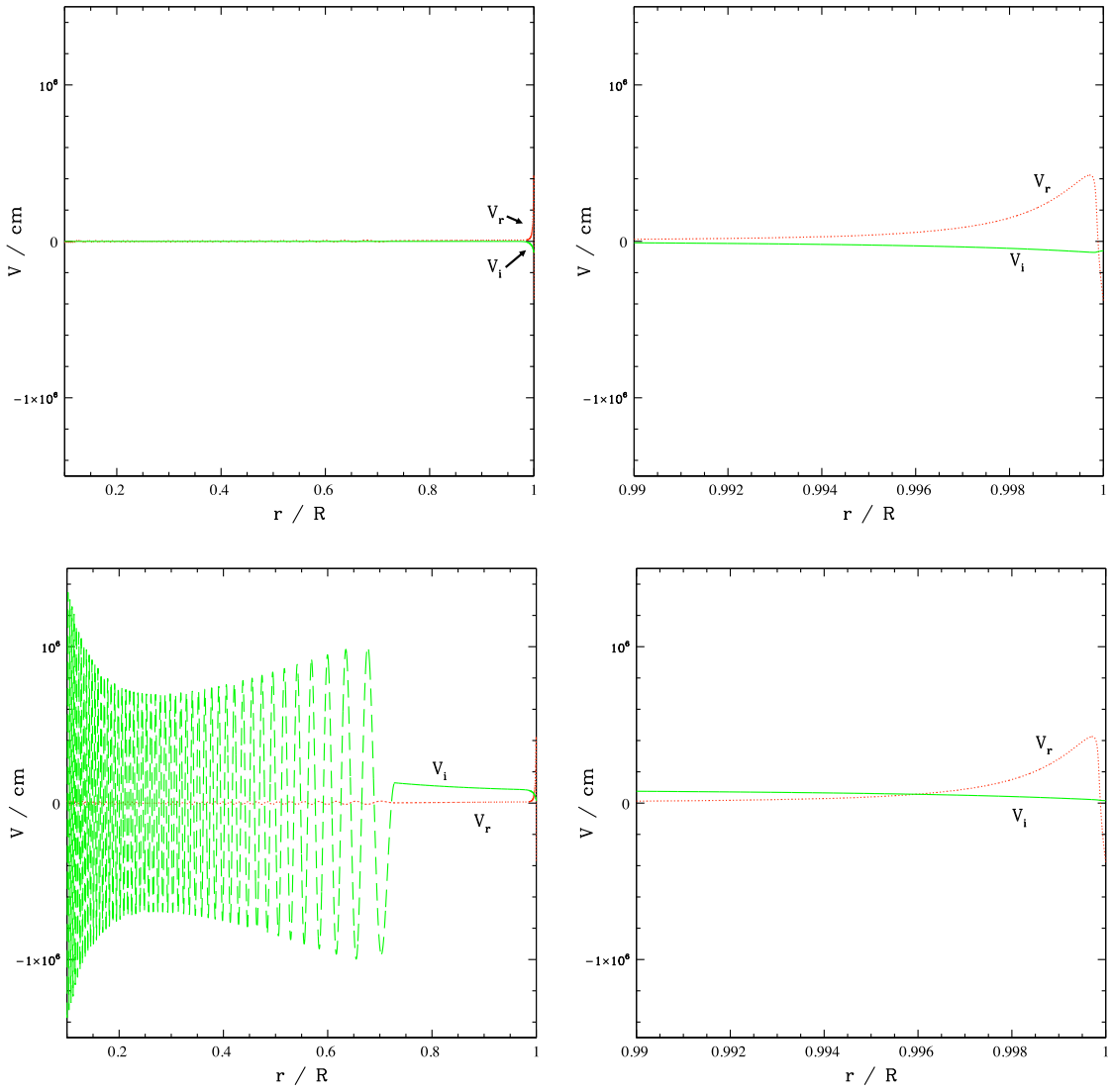


Figure 3.21: This shows snapshots of the response obtained during the resonance search for a 1 $M_\odot$ star, with perturbed convection following approach A. The real and imaginary components of the function $V$ are plotted as a function of $r/R$ for the range $0.1 < r/R < 1$ in the left hand panels and for the range $0.99 < r/R < 1$ in right hand panels. The upper panels correspond to the forcing frequency $2\omega_0$, and the lower panels to a forcing frequency of $1.99965\omega_0$, which corresponds to the centre of the closest resonance, with the forcing frequency being twice the orbital frequency. By comparing the upper and lower right hand panels it can be seen that the behaviour of $V$ close to the surface is almost unaffected by the resonant excitation below.

and pressure, which cannot be achieved when the perturbation is non–adiabatic. As a result, there is a large amplification of the horizontal displacement.

Changing the exact treatment of convection used does produce quantitatively different results, with a factor of $\sim 10$ difference between the values of the horizontal displacement, and between the flux perturbations at the surface. Another significant difference is in the extent of the region over which the perturbations diverge from the equilibrium tide values. In the case of frozen convection the perturbations do not have much scope to grow in the convection zone as the flux cannot be perturbed there, by assumption, and the perturbations are shown to change rapidly over a length scale of a few times the depth of the surface radiative layer once the flux can be perturbed once again. This essentially restricts the depth of the non adiabatic layer, such that the sharp variation occurs within, or very close to, the photosphere.

Adopting a more plausible approximation of perturbed convection smooths out the changes compared to those found using the assumption of frozen convection, as they occur over a greater radial extent of the star instead of being confined to the radiative skin of the star. This results from the fact that the convective flux can be perturbed, and departures from the equilibrium tide become evident once the timescale $|1/N|$ exceeds the timescale of the oscillation (around $r/R \sim 0.97$ for $M = 1$ $\mathrm{M}_{\odot}$). Nonetheless, in this case, the radial displacement remains close to the equilibrium value, with a sudden, but much less pronounced, peak just below the surface, and a phase shift of only around 1 degree at the surface, suggesting that non–adiabatic effects are only weakly evident in the radial displacement. Note that our resonance survey indicated resonant forcing frequencies for which there were large spikes in the kinetic energy of the oscillation, associated with high order $g$–modes confined to the core. However, these were found to have little effect on the solution near the surface. Also, in the absence of special conditions leading to resonance locking, non linear effects and increased dissipation are expected to lead to a low probability of being found in resonance.

In the perturbed convection case the horizontal displacement still significantly deviates from the equilibrium approximation, with a surface magnitude which is greater than the equilibrium approximation by a factor of $\sim 30$ when procedure A was followed for convection. This could be reduced by a factor of three if procedure B was followed instead. On the other hand, we remark that a test carried out where we returned to procedure A but simply increased the convective flux perturbation by a factor of 1.5 (to investigate the inclusion of a perturbation to the convective velocity) showed that surface horizontal displacement increased by a factor of three. The phase

shift of $V$ for procedure B at the surface is also more significant, of $\sim 10$ degrees. These are both potentially testable predictions for observations, as the horizontal displacement could be detected through spectroscopy. The conversion of these behaviours into observable signals is discussed in chapter 4.

The form of the horizontal displacement given in equation 3.30 shows that $V \propto 1/\omega^2$. As the tidal perturbation scales as $D^{-3} \propto \omega^2$, the effect on $V$ from the change in $\omega$ will be counteracted by the change in the tidal perturbation, and we expect that the horizontal displacement will be constant for a given planetary mass, independent of the orbital distance. This has been found to be the case in our numerical solutions. The associated radial velocity signal would therefore be proportional to $\omega$, which is further investigated and discussed in chapter 4.

The perturbation to the flux at the surface is also significantly different between the approximations of frozen and perturbed convection. Both show significantly non–adiabatic behaviour towards the surface, with large magnitudes and non–negligible imaginary parts, although the detailed form does depend strongly upon the treatment of convection. Nonetheless, in the case of perturbed convection, the magnitude of the perturbed energy flux can be estimated in a simple way by evaluating the flux using the equilibrium tide near the base of the non–adiabatic layer (see Fig.3.18).

Deep within the convection zone, $A$ is large and $\partial s_0/\partial r$ (the background entropy gradient) is small, so a very small perturbation to the entropy gradient can produce a large perturbation to the flux. This approximation may then give rise to anomalously large perturbations to the convective flux in this region. Towards the surface, and particularly within the superadiabatic zone, $A$ becomes small, as convection becomes inefficient, and $\partial s_0/\partial r$ is large. Therefore, in this region, the approximation will hold better as errors are less likely to have a significant impact, and the non–adiabatic behaviour of the displacement can be calculated more reliably. Overall, although this model may produce anomalous values in the surface flux due to inaccuracies in modelling convection deep within the convection zone, it is able to model the displacement within the superadiabatic zone and towards the surface reasonably well.

On balance, this investigation shows that, at the surface of a solar-mass star, the equilibrium tide approach falls short of reality. The non-adiabatic effects shown to be present in this chapter match well with the analytic predictions of the non-adiabatic radius, showing that, even if these results are not quantitatively exactly accurate, the underlying fact that non-adiabatic effects have a major impact upon the surface response is expected to hold true. The model used for the convective flux clearly has an impact upon the response of the star, though there are aspects of the response

which appear to be independent of this choice, particularly that $V$ tends towards a constant value, independent of the orbital period, whereas the radial displacement roughly scales with the perturbation. The perturbed flux also seems to scale with the perturbation, although the surface values may be exaggerated by the shortfall of the model used in the deep convective zone.

Whilst the magnitude of the radial displacement is unlikely to result in a large change of observed brightness, the perturbation to the flux may be such that it produces a detectable photometric signal. The increased surface motion due to the large value of $V$ may lead to a spectroscopic signal which is larger than expected under the equilibrium tide approximation. This, and the other impacts of including non-adiabatic effects on potentially observable effects, is explored in detail in the next chapter.

# Chapter 4

# Observables

In order to test the predictions of our models, we must consider the manner in which the predicted behaviour can be observed. In this chapter we set out some different approaches to this. The most straightforward approach of using the disc-integrated signal has been discussed in previous work (Dziembowski (1977); Pfahl et al. (2008); Arras et al. (2012)) and will be outlined in section 4.2, although the details will be left to the appendices (appendix E and appendix F). Alternative methods are introduced in section 4.3, which avoid the need to integrate over the visible disc.

The surface behaviour of a test case model is explored to investigate the change in behaviour as the orbital period of the perturbing body is varied in section 4.4, before the observable signals of some real planetary systems are detailed in section 4.5. These results are then discussed in section 4.6, where the potential usefulness of these predictions is addressed.

## 4.1 A note on coordinates and integrals

Throughout this chapter and the relevant appendices (appendix D to G) we must explicitly deal with two different coordinate systems – one arranged to match the symmetry of the orbital system, which is the coordinate system used in previous chapters, and one based on the direction to the observer, in order to integrate over the visible disc of the star. Therefore we make the two different coordinate systems very explicit throughout this chapter with the subscripts used.

As before, we assume a non–rotating star with polar coordinates $(r, \theta_*, \phi_*)$ centred on the star, with the planetary companion existing in a circular orbit with $\theta_* = \pi/2$. In this frame, the observer is taken to be in the direction given by $(\theta_0, \phi_0)$.

In the observer's frame, described by $(r, \theta_{\rm ob}, \phi_{\rm ob})$, the observer is at $\theta_{\rm ob} = 0$, with $\theta_{\rm ob} < \pi/2$ visible to the observer. The unit vectors associated with these coordinate systems are denoted with a *hat*.

To convert between the two frames, we use the properties of spherical harmonics and Euler angles, guided by Morrison & Parker (1987) and detailed in Appendix D. For integrations over the visible disc we need only keep track of one spherical harmonic (as the integral over $\phi_{\rm ob}$ will eliminate terms with $e^{i\mu\phi_{\rm ob}}$ where $\mu \neq 0$). This allows us to convert the expression of the star's tidal response into the coordinates of the observer's frame, as (eq. [D.5]):

$$\int_0^{2\pi} 3\sin^2\theta_* e^{2\mathrm{i}(\omega t - \phi_*)} \mathrm{d}\phi_{\rm ob} = 3\pi \sin^2\theta_0 (3\cos^2\theta_{\rm ob} - 1) e^{2\mathrm{i}(\omega t - \phi_0)}. \tag{4.1}$$

To account for $\boldsymbol{\xi}_h$ we use the fact that the relation $\boldsymbol{\xi}_h = r\boldsymbol{\nabla}_h V$ is true independent of the orientation of the coordinate system used. This gives the expression for the horizontal displacement, integrated over a ring of constant $\theta_{\rm ob}$, as:

$$\begin{aligned}
&\int_0^{2\pi} \xi_{\theta_{\rm ob}}(r, \theta_{\rm ob}, \phi_{\rm ob}, t) \mathrm{d}\phi_{\rm ob} \\
&\qquad = \Re\left[\frac{\partial}{\partial\theta_{\rm ob}} \int_0^{2\pi} V(r) 3\sin^2\theta_* e^{2\mathrm{i}(\omega t - \phi_*)} \mathrm{d}\phi_{\rm ob}\right], \\
&\qquad = \Re\left[-18\pi V(r) \sin^2\theta_0 \cos\theta_{\rm ob} \sin\theta_{\rm ob} e^{2\mathrm{i}(\omega t - \phi_0)}\right],
\end{aligned} \tag{4.2}$$

where we have retained only the component which will be observed, as the displacement perpendicular to the direction towards the observer does not contribute since $\hat{\boldsymbol{\phi}}_{\rm ob} \cdot \hat{\mathbf{n}}_{\rm ob} = 0$, where $\hat{\boldsymbol{n}}_{\rm ob}$ is the unit vector towards the observer.

## 4.2 Conventional approaches to tidal signals

We here outline the conventional approach to detecting tidal signals, both photometrically and spectroscopically. Further details can be found in Dziembowski (1977).

### 4.2.1 Luminosity variation

The observed luminosity is given by

$$L = \int\int h \bar{F} \hat{\boldsymbol{n}}_{\rm ob} \cdot \hat{\boldsymbol{n}} \mathrm{d}S \tag{4.3}$$

where $h$ is the limb-darkening (note that this is wavelength dependent), $\bar{F}$ is the emergent flux, equal to $\boldsymbol{F} \cdot \hat{\boldsymbol{n}}$, $\hat{\boldsymbol{n}}$ is the unit vector normal to the surface, and $\mathrm{d}S$ is the surface area element.

In order to evaluate the first order change in luminosity, each of these terms must be evaluated as a function of perturbations to the equilibrium state, which will result in first order changes in luminosity due to limb–darkening, flux, surface normal, and surface area, corresponding respectively to $\Delta L_{\rm h}$, $\Delta L_F$, $\Delta L_n$, and $\Delta L_S$. Full details of the derivation can be found in appendix E.

The equilibrium luminosity is given by

$$L_0 = \int_0^{2\pi}\int_0^{\frac{\pi}{2}} h_0 \bar{F}_0 \hat{\boldsymbol{r}}\cdot\hat{\boldsymbol{n}}_{\rm ob}\mathrm{d}S_0, \tag{4.4}$$

where the subscript 0 indicates that it is the equilibrium value. The integral is calculated in the observer's frame, so that $\hat{\boldsymbol{r}}\cdot\hat{\boldsymbol{n}}_{\rm ob} = \cos\theta_{\rm ob}$. We have: $h_0 = c(1-u+u\hat{\boldsymbol{r}}\cdot\hat{\boldsymbol{n}}_{\rm ob})$, where $u$ parametrises the limb darkening and $c$ normalises it, such that $\int_0^1 \mu h \mathrm{d}\mu = 1$, with $\mu = \cos\theta_{\rm ob}$ (for Eddington limb-darkening, as used here, $c = 5/2$ and $u = 3/5$ (Dziembowski, 1977)); $\bar{F}_0 = \boldsymbol{F}_0\cdot\hat{\boldsymbol{r}}$ where $\boldsymbol{F}_0$ is the vector equilibrium radiative flux at the surface (equal to $F_0\hat{\boldsymbol{r}}$, where $F_0$ is its magnitude); $\hat{\boldsymbol{r}}$ is the radial unit vector, which is the surface normal for the equilibrium case; $\mathrm{d}S_0 = R^2\sin\theta_{\rm ob}\mathrm{d}\theta_{\rm ob}\mathrm{d}\phi_{\rm ob}$, where $R$ is the equilibrium radius of the star.

The explicit expression for the equilibrium luminosity is then found to be

$$L_0 = 2\pi R^2 F_0, \tag{4.5}$$

where the factor of 2 comes from the definition of the normalisation of the limb darkening.

The first order perturbations are calculated by expanding the four terms in the integrand into their equilibrium and first order terms, as detailed in Appendix E, resulting in the following expressions:

$$\Delta L_h = \Re\left[\frac{12\pi}{5} RcuF_0\left[V(R)-\xi_r(R)\right]\sin^2\theta_0 \mathrm{e}^{2\mathrm{i}(\omega t-\phi_0)}\right], \tag{4.6}$$

$$\Delta L_F = \Re\left[\frac{3\pi}{4}R^2 c\left(1+\frac{u}{15}\right)\left[F_r'(R)+\xi_r(R)\frac{\mathrm{d}F_0}{\mathrm{d}r}\right]\sin^2\theta_0\sin^2\theta_0 \mathrm{e}^{2\mathrm{i}(\omega t-\phi_0)}\right], \tag{4.7}$$

$$\Delta L_n = \Re\left[\frac{9\pi}{2} Rc\left(1-\frac{7u}{15}\right)F_0\left[V(R)-\xi_r(R)\right]\sin^2\theta_0 \mathrm{e}^{2\mathrm{i}(\omega t-\phi_0)}\right], \tag{4.8}$$

$$\Delta L_S = \Re\left[\frac{3\pi}{2} Rc\left(1+\frac{u}{15}\right)F_0\left[\xi_r(R)-3V(R)\right]\sin^2\theta_0 \mathrm{e}^{2\mathrm{i}(\omega t-\phi_0)}\right], \tag{4.9}$$

which can be combined to give the fractional total change in luminosity as:

$$\frac{\Delta L}{L_0} = \Re\left[\frac{3}{8}c\left(1+\frac{u}{15}\right)\left(\frac{\Delta F_r}{F_0}-4\frac{\xi_r(R)}{R}\right)\sin^2\theta_0 \mathrm{e}^{2\mathrm{i}(\omega t-\phi_0)}\right]. \tag{4.10}$$

where:

$$\Delta F_r = F_r'(R) + \xi_r(R)\frac{\mathrm{d}F_0}{\mathrm{d}r}(R).$$

Whilst the individual effects may involve the horizontal components of displacement, as noted by Heynderickx et al. (1994) they cancel out exactly to first order.

### 4.2.2 Radial velocity variation

The periodic change in shape of the star results in a periodic change in the velocity of any given surface element. Projecting this along the observer's line of sight gives the radial velocity (RV) which is proportional to the shift in wavelength caused by the motion (for the very non-relativistic motions considered here). Expressing this formally gives

$$\mathrm{v_{RV}} = -\dot{\boldsymbol{r}}\cdot\boldsymbol{n}_{\mathrm{ob}}, \tag{4.11}$$

where $\boldsymbol{r}$ is the vector from the centre of the star to the surface element in question.

To first order in perturbed quantities, this becomes

$$\mathrm{v_{RV}} = -\dot{\boldsymbol{\xi}}\cdot\boldsymbol{n}_{\mathrm{ob}} = \Re\left(-2\mathrm{i}\omega\boldsymbol{\xi}\cdot\boldsymbol{n}_{\mathrm{ob}}\right). \tag{4.12}$$

This can be encapsulated by a single curve by integrating over the disc, weighted by the luminosity, as done by Dziembowski (1977):

$$\mathrm{v_{disc}} = \frac{\iint \mathrm{h}\hat{\boldsymbol{r}}\cdot\hat{\boldsymbol{n}}_{\mathrm{ob}}\bar{\mathrm{F}}_0\mathrm{v_{RV}}\mathrm{dS}}{\iint \mathrm{h}\hat{\boldsymbol{r}}\cdot\hat{\boldsymbol{n}}_{\mathrm{ob}}\bar{\mathrm{F}}_0\mathrm{dS}} = \frac{1}{2\pi\mathrm{R}^2}\int\int \mathrm{h}\hat{\boldsymbol{r}}\cdot\hat{\boldsymbol{n}}_{\mathrm{ob}}\mathrm{v_{RV}}\mathrm{dS}, \tag{4.13}$$

which can be analytically solved.

Evaluating this integral gives the final expression for the disc–integrated radial velocity as:

$$\mathrm{v_{disc}} = \Re\left\{-\frac{4}{5}\mathrm{i}\omega\mathrm{c}\left[\left(1-\frac{\mathrm{u}}{16}\right)\xi_{\mathrm{r}}(\mathrm{R})+3\left(1-\frac{3u}{8}\right)V(R)\right]\sin^2\theta_0\mathrm{e}^{2\mathrm{i}(\omega\mathrm{t}-\phi_0)}\right\}. \tag{4.14}$$

It is worth noting the dependencies on the orientation of the system: $\sin^2\theta_0$ differs from the $\sin\theta_0$ dependence in standard RV detections, and $\phi_0$ introduces a phase difference, as expected, but non–adiabaticity at the surface (exhibited by non–zero imaginary components of variables) can also lead to a phase difference.

Alternatively, the full spectrum of the line–broadening can be computed by numerically integrating over the visible disc to calculate the luminosity as a function of radial velocity. This enables the time–dependent line–broadening to be evaluated, and a non–trivial signal is present at all orientations of the system (although, for a

face–on system, the signal is time–independent). This can be written as a sum of the equilibrium luminosity contributed by all of the surface elements within a certain range of the radial velocity in question:

$$\frac{\mathrm{d}L(\mathrm{v})}{\mathrm{d}\mathrm{v}} = \frac{1}{\Delta\mathrm{v}} \sum_{\mathrm{v}-\frac{\Delta\mathrm{v}}{2}}^{\mathrm{v}+\frac{\Delta\mathrm{v}}{2}} h \cos\theta_{\mathrm{ob}} \bar{F}_0 \mathrm{d}S_0 \tag{4.15}$$

where $\Delta\mathrm{v}$ is the width of the bin and the surface area element, $\mathrm{d}S_0 = R^2 \sin\theta_{\mathrm{ob}} \mathrm{d}\theta_{\mathrm{ob}} \mathrm{d}\phi_{\mathrm{ob}}$, is calculated in the observer's frame. This is further discussed in section 4.3.2.

## 4.3 Alternative methods of observation

Above, we have described the standard methods used for detecting the tidal signal at the stellar surface. In this section, we set out alternative methods which would provide opportunities to deduce further information about the oscillations, and present some potential signals. Further details can be found in Appendix G.

### 4.3.1 Signal during transit

As the planet occludes part of the stellar disc, comparing the signal at a point during transit to the signal during the secondary eclipse (when the planet is blocked from view by the star) provides the opportunity to isolate the signal originating from a given location on the stellar surface. This enables the horizontal and radial displacements to be disentangled, as the relative contributions to the RV signal from $\xi_r$ and $V$ vary differently across the face of the stellar disc, with $V$ and $\xi_r$ being more prominent at the edges and towards the centre, respectively.

As the planet crosses the disc, the RV signal at a particular radial velocity will be reduced, with the reduction in brightness depending on the limb–darkening and how much of the rest of the disc is also producing a signal at the same radial velocity.

During a transit, we can approximate $\theta_0 \approx \pi/2$ and, by taking the midpoint of the transit to occur at $t = 0$, $\phi_0 \approx 0$, enabling an analytical approximation for the value of $\mathrm{v}_{\mathrm{RV}}$ as a function of position on the stellar disc. Practically, a slowly rotating star will result in the Rossiter-McLaughlin effect, over which the tidal signal will be superimposed (as a very rough estimate, the Rossiter-McLaughlin effect may give a signal on the order of tens of metres per second, and the tidal signal may be around a few metres per second). Approximating the motion of the planet as a constant then gives an analytical expression for the value of $\mathrm{v}_{\mathrm{RV}}$ blocked as a function of time. More details can be found in Appendix G.2.0.1.

This method could also be applied to the luminosity variation in order to calculate the extra change in brightness due to blocking that part of the perturbed flux signal, although this contribution would be a factor of $F'/F_0$ smaller than the transit signal, so would be very difficult to detect.

### 4.3.2 Time–dependent line broadening

The differential motion of the stellar surface produces an inhomogeneous broadening effect (Cunha et al., 2007). Throughout the oscillation, the shape of the broadening will change, depending on $\xi_r$, $V$ and the inclination. Some example line–shapes are shown in Figure 4.1, for three different phases of the planet's orbit.

As a constant line–broadening would be indistinguishable from other sources of constant line–broadening (such as Doppler broadening due to the non–zero temperature at the stellar surface), we would only expect to be able to discern a periodically changing line–width, due to the change in line–shape from the surface motion.

This can be calculated by integrating the flux over the visible surface to find the total flux emitted at each radial velocity. This has been done numerically, and produces a line–shape which is sharply peaked at $\mathrm{v}_{\mathrm{disc}}$. The strange and non–constant shape makes it difficult to accurately describe the broadening effect with a single parameter. Because the peak is so sharp, using the Full Width at Half Maximum focusses only on a small region and neglects the wider broadening where the bulk of the flux is. Instead, the Inter-Quartile Range (IQR) has been used, to give the width of the range of radial velocities over which the central 50% of the luminosity is emitted. Over the course of the oscillation the line–shape changes symmetrically such that the IQR of the line–shape with peak at $q$ is equal to the IQR of the line–shape with peak at $-q$. This gives rise to an oscillating IQR, with period equal to $P/4$.

As observations of stellar linewidths will also be impacted by other sources of broadening, such a thermal broadening and pressure broadening, the lineshapes given in in Figure 4.1 would act as broadening kernels, and would be convolved with the lineshape arising due to other sources of broadening, potentially smearing out this effect somewhat.

## 4.4 Results for test cases

In order to understand the implications and limitations of these tidal oscillations more generally, the test cases used in chapter 3 are explored as examples here. Extreme

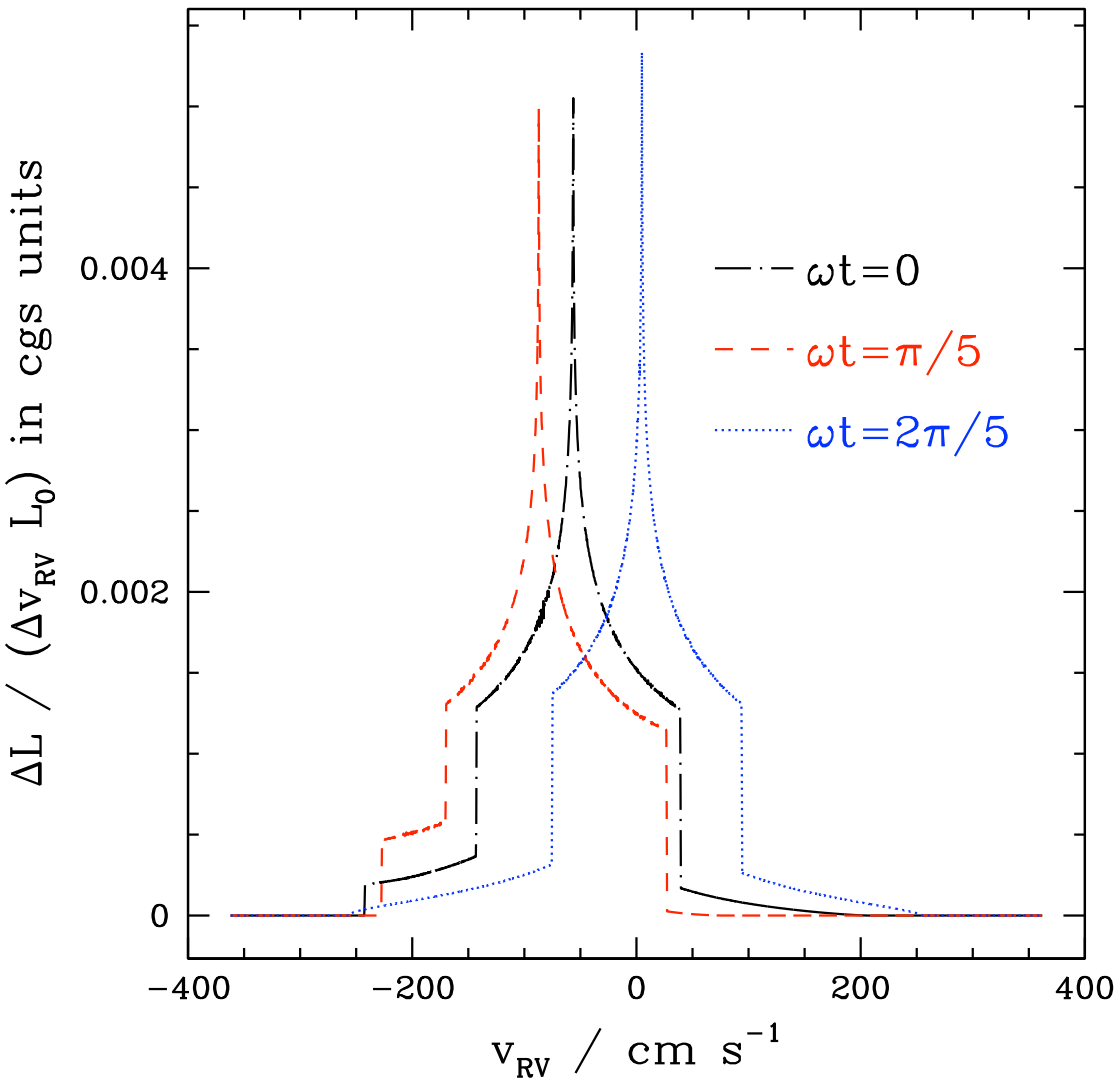


Figure 4.1: The line–shape for the case of CoRoT-17 is shown here for three different phases of the planet's orbit. The shape of the broadening is clearly non-Gaussian in each case, with an asymmetric shape. The sharp central peak means that the use of the Full Width Half Maximum as a measure of broadening does not accurately convey the change in the line–shape, as it accounts only for a small amount of the total brightness. Instead the inter-quartile range (IQR) is used, to track the range of radial velocities over which the central 50% of the flux is emitted. The time-dependent line–broadening of CoRoT-17 is discussed further in section 4.5.6.2.

cases are used to show where this approach may break down, and why, and general relationships are also demonstrated.

### 4.4.1 Long period behaviour

#### 4.4.1.1 Perturbed convection

As the period of the orbit increases, the proportion of the convection zone in which $|N|^2 \ll (m\omega)^2$ decreases, and the transition into the super–adiabatic region occurs deeper in the star. This gives rise to increasingly large deviations in $\xi_r$ from the equilibrium tide displacement within the convection zone, but does not produce a significant change in the response of the displacement at the very surface – that is, $\xi_r \approx \xi_{r,eq} \propto P^{-2}$ and $V$ remains approximately constant there. This holds up to very long periods of $\sim 100$ days.

The perturbation to the flux depends on the forcing frequency, with the magnitude of the response, both within the convection zone and at the very surface, proportional to $P^{-2}$. This holds from periods of a couple of days up to periods of hundreds of days.

At long periods, the wavelength of the spatial oscillations in the stellar core becomes very small. As a result of this, resolving the oscillations computationally becomes difficult. The presence of a thick convection zone may reduce the impact that these unresolved oscillations have on the surface response, which is suggested by the fact that the surface response remains consistent with the expected behaviour even once the core is very poorly resolved. Resolution issues become apparent in the centre of the star in this model for orbital periods above $\sim 20$ days, and become apparent at $r = 0.5R$ for periods above $\sim 100$ days.

#### 4.4.1.2 Frozen convection

In this case, the behaviour within the body of the star is fairly similar to that obtained when convection is perturbed, but the surface response is very different. The frozen convection case displays much larger changes over a thin surface region of the star, resulting in $|\xi_r|$ being suppressed by around a factor of 10 compared to $\xi_{r,eq}$. On the other hand, $|V|$ is still constant, but at a much larger value than in the perturbed convection case. This value agrees well with the prediction for the low–frequency limit in the non–adiabatic case which is $|V/R| = m_p/(4m^2M)$, where $M$ is the stellar mass, $m_p$ is the planet's mass and $m = 2$ (Bunting et al., 2019).

The surface value of the flux is reduced by an order of magnitude by freezing convection, compared to the perturbed convection case. Within the convection zone,

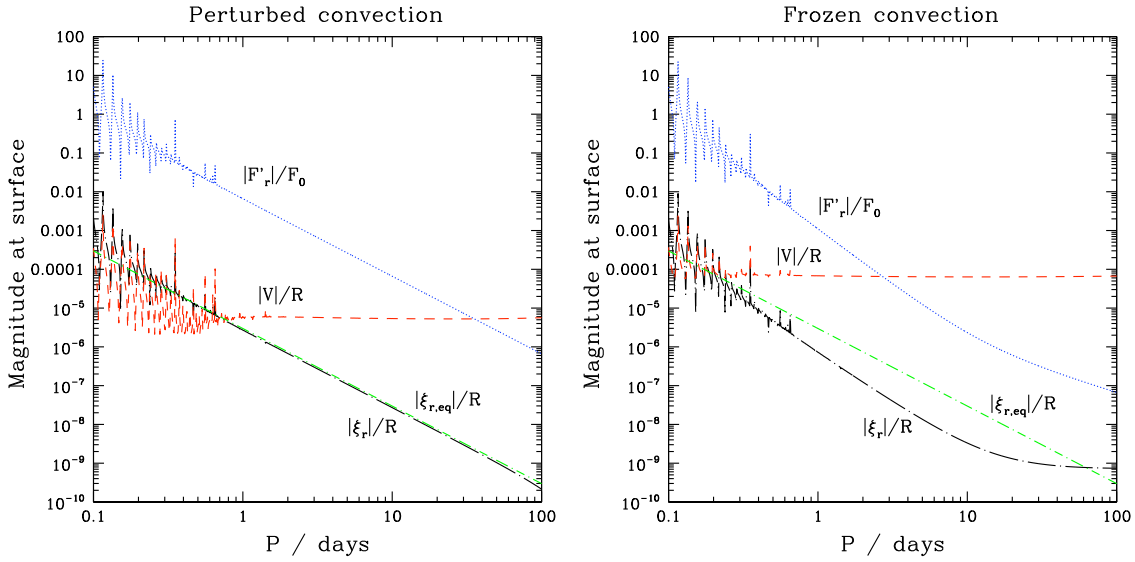


Figure 4.2: The magnitude of the radial displacement $|\xi_r|/R$ (long dashed–dotted black curve), horizontal displacement $|V|/R$ (dashed red curve), equilibrium tide radial displacement $|\xi_{r,\mathrm{eq}}|/R$ (short dashed–dotted green curve), and flux perturbation $|F_r'|/F_0$ (dotted blue curve), as a function of the orbital periods $P$ in days, in logarithmic scale. The left panel shows the results for a star with perturbed convection, and the right panel shows the results for the case of assuming frozen convection. Both cases show a constant $|V|$. In the perturbed convection case, $|F_r'|$ and $|\xi_r|$, like $\xi_{r,\mathrm{eq}}$, are proportional to $P^{-2}$. In the frozen convection case and for periods less than 10 days, $\xi_r$ and $F_r'$ are roughly proportional to $P^{-3}$. For periods of less than a day, resonances become prominent, and the background scaling is somewhat obscured. There are some differences between the two cases – the perturbed convection value of $\xi_r$ closely matches the equilibrium tide, whereas the frozen convection $\xi_r$ is suppressed by about an order of magnitude; the frozen convection $F_r'$ is approximately an order of magnitude smaller than for the perturbed convection case; and $V$ attains a constant value which is an order of magnitude larger in the frozen convection case than in the perturbed convection case.

the assumption of frozen convection causes the flux to be greatly suppressed before growing over a very small scale when approaching the thin radiative skin, as opposed to growing over a large scale throughout the convection zone as in the perturbed convection case.

The results for both perturbed and frozen convection are illustrated in Figure 4.2.

### 4.4.2 Short period behaviour

At very short periods, the Brunt–Väisälä frequency in the radiative core can become comparable to the oscillation frequency. When this occurs, the behaviour of $\xi_r$ in the core can deviate significantly from the equilibrium tide as opposed to oscillating around it as in the reference case with $P = 4.23$ days. This deviation then persists throughout the convection zone and produces surface behaviour which doesn't resemble the equilibrium tide prediction, as seen in Figure 4.2. This would have an impact on the behaviour of this system at periods of $\sim 0.3$ day or less.

At such short periods, the assumption of small perturbations can break down. In the very centre of the star, $F'$ can become large such that it is no longer negligible compared to the background flux when considering the stellar structure. This can occur in this model for periods up to $\sim 0.8$ day. Whilst this is primarily a consideration at the centre of the star, large deviations can occur in the radiative skin at the surface for orbital periods up to $\sim 0.3$ day.

### 4.4.3 Resonances

Whilst resonances do have a significant effect on the response of the stellar interior (such that the assumption of small perturbations may no longer be valid when very close to resonance), the response at the surface is much less pronounced. When going through a resonance, the RV signals for orbital periods of a couple of days change by $\sim 10\%$, whilst the photometric signals change by around $\sim 1\%$. Resonances for this system are therefore not likely to greatly impact the observed signals, in the unlikely event that an on–resonance system is found.

For periods in the range 1–10 days, the resonances are very narrow, with a quality factor $\sim 10^5$ around $P \approx 4$ days. As the period decreases, the resonances become less sharp, and have a more prominent impact for periods less than a day, and particularly once $\xi_r \sim V$, as seen in Figure 4.2.

The choice of model for the convective flux does not affect the location or quality factor of resonances, as it is the radiative zone which acts as the resonant cavity.

The effect at the surface is changed, however, as the extent to which this resonant cavity is isolated from the surface depends on how the response within the convective zone is modelled. By freezing convection, any deviation from equilibrium present at the base of the convection zone is maintained throughout the convection zone and is able to produce greater deviations from equilibrium in the thin radiative skin at the surface. By contrast, including a perturbation to the convective flux allows the non–equilibrium behaviour of the radiative zone to be attenuated before reaching the surface.

### 4.4.4 General trends

The calculation of the response of the star is expected to be valid within the limits stated above. For orbital periods between 1 and 20 days, the system is well modelled, with the results likely to hold for longer periods up to 100 days. The change in the amplitude and phase of the response when the orbital period is varied yields a change in the the observable signals. Here we describe some general behaviours.

Figures 4.3 and 4.4 show the disc–integrated radial velocity, $\mathrm{v}_{\mathrm{disc}}$, calculated using equation (4.14). As can be seen on these figures, $|\mathrm{v}_{\mathrm{disc}}| \propto P^{-1}$, which is a result of the signal being dominated by $V$, which remains fairly constant. The phase shift of the response is similarly constant, and does not change as the period increases further.

At short periods $|\xi_r| \sim |V|$ is approached, and $V$ is no longer dominant. At this point, $V$ starts to deviate from the expected constant value, and scales roughly as $P^{-2}$, just as the radial displacement does. This change in scaling is reflected in the scaling of the RV signal, which goes as $|v_{\mathrm{disc}}| \propto P^{-3}$. However, as these very short periods, the presence of wider resonances somewhat obscures the background scaling relation.

At $P = 1$ day both the equilibrium tide and the perturbed convection model predict an amplitude of $\sim 100$ cm s$^{-1}$, whilst the frozen convection model predicts an amplitude of $\sim 1400$ cm s$^{-1}$. The phase for the equilibrium tide and perturbed convection models are however significantly different, with the signals being almost in anti–phase with each other. At $P = 2$ days, the equilibrium tide prediction is reduced to $\sim 15$ cm s$^{-1}$, whilst the responses including convection are both reduced by a factor of two, at $\sim 60$ cm s$^{-1}$ for perturbed convection and $\sim 760$ cm s$^{-1}$ for frozen convection.

As the orbital period increases further, the disparity between the equilibrium tide prediction and those including convection widens further, with the amplitude of the equilibrium tide prediction at $P = 8$ days being less than 1 cm s$^{-1}$, compared to $\sim 16$

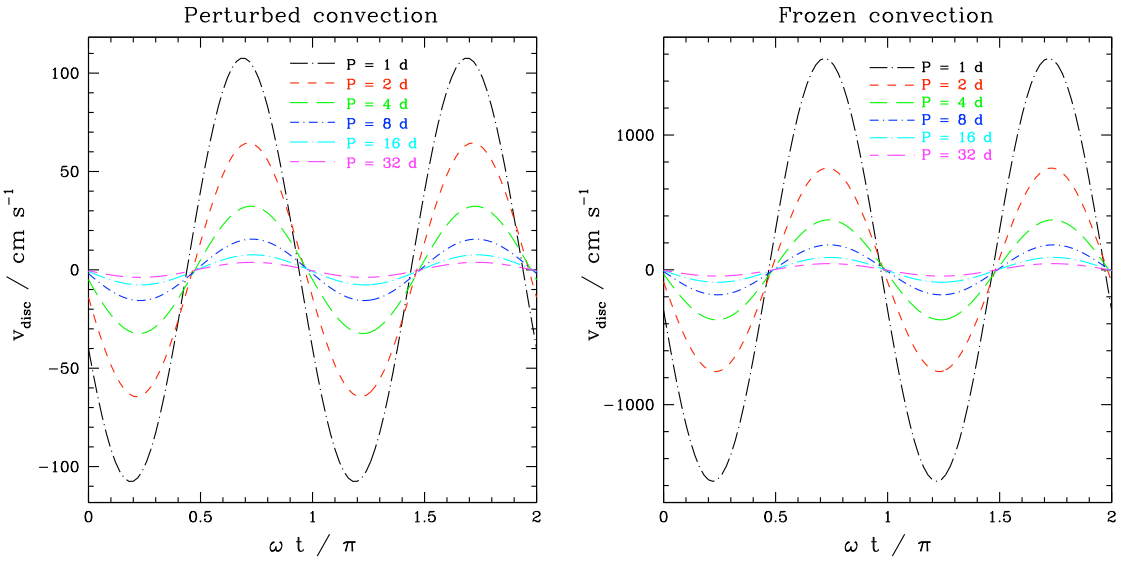


Figure 4.3: The disc–integrated radial velocity $v_{disc}$ (in units of cm $s^{-1}$) is shown against orbital phase $\omega t/\pi$ for a range of orbital periods for the case of perturbed convection (on the left) and frozen convection (on the right). From the largest to the smallest amplitude, the different curves correspond to $P$=1, 2, 4, 8, 16 and 32 days. In both cases, the amplitude scales as $P^{-1}$, which is different than the scaling corresponding to the equilibrium tide prediction. This is a due to $V$ dominating the signal, as it is much larger than $\xi_r$, and being constant. This will lead to RV signals which are larger than predicted by the equilibrium tide , particularly at longer orbital periods. As the orbital period changes, the phase of the RV signal remains fairly constant. At short periods however, $\xi_r$ becomes comparable to $V$ and the phase is no longer constant. Comparing the two convection models shows that the frozen model produces a signal which is an order of magnitude larger than predicted by the perturbed convection model. This follows directly from the constant value of $V$ being an order of magnitude larger in the frozen convection case.

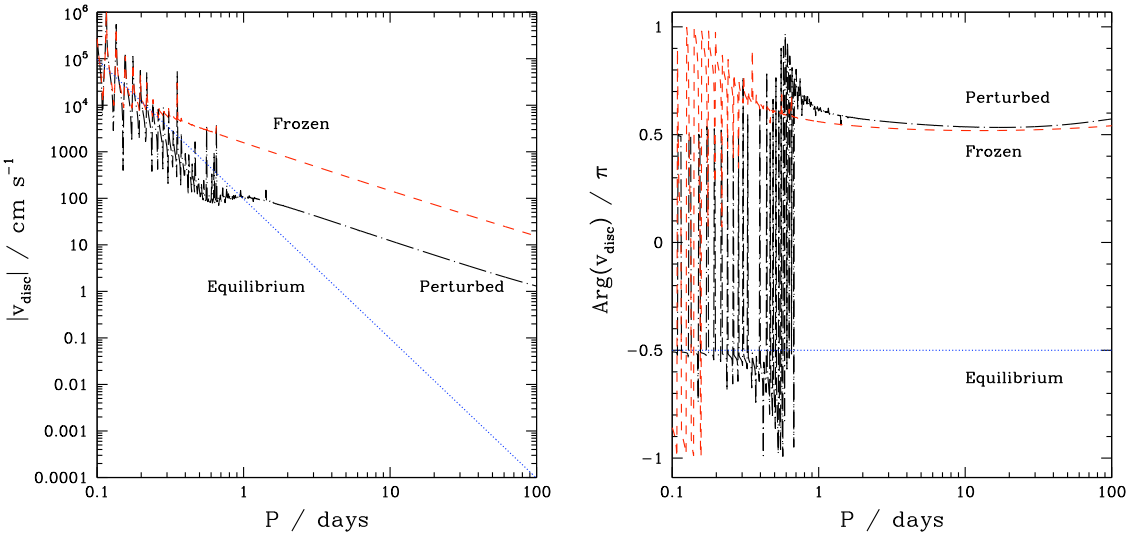


Figure 4.4: The magnitude (left panel) and phase (right panel) of the disc–integrated radial velocity $v_{disc}$ is shown against orbital period for a Jupiter–mass planet orbiting a solar–mass star, comparing three models: frozen convection (dashed red line), perturbed convection (dashed dotted black line), and the equilibrium tide (dotted blue line). For periods greater than $\sim 1$ day, the frozen and perturbed convection models both scale as $P^{-1}$, whereas the equilibrium tide scales as $P^{-3}$. This leads to large deviation in the predicted signal amplitude for long period orbits: at $P = 10$ days the equilibrium tide prediction is $|v_{disc}| = 0.1\,\mathrm{cm\,s^{-1}}$, whereas the perturbed convection and frozen convection models are larger than this by a factor $10^2$ and $10^3$, respectively. At short periods, once $|\xi_r| \sim |V|$, resonances become significant, and the scaling of $v_{disc}$ changes to follow the equilibrium tide scaling (as $\xi_r$ scales as $\xi_{r,eq}$). The phase of the signals remains fairly consistent for orbital periods greater than 1 day, with resonances clearly present below that value. The perturbed and frozen convection models are $\pi$ out of phase with the equilibrium tide prediction.

cm $s^{-1}$ for the perturbed convection case, and 190 cm $s^{-1}$ for the frozen convection case.

As changing the model used for convection does not affect the scaling of the response with orbital period, the frozen convection case consistently predicts an amplitude which is larger by an order of magnitude than the prediction from the perturbed convection case.

Figure 4.5 shows the fractional change in luminosity, $\Delta L/L_0$, calculated using equation (4.10). In the perturbed convection case, the photometric signal scales with the perturbation, and so is proportional to $P^{-2}$, as can be seen on the figures. For the frozen convection case, and for periods under 10 days, the scaling with $P$ is steeper than this, being closer to $P^{-3}$.

At very short periods, both models with perturbed or frozen convection predict extremely large values of $\Delta L/L_0$. The assumption of small perturbations is clearly no longer valid there, and the calculation of $F'$ in this regime may not be reliable, as mentioned in section 4.4.2. To test the effect of the perturbed flux on the photometric signal, we compare, in Figure 4.6, $\Delta L/L_0$ obtained from equation (4.10) with this quantity calculated by setting $F'_r = 0$ and keeping only the contribution from $\xi_r$. If the perturbed flux were overestimated in our model, the realistic value of the change in luminosity would probably be bracketed by these two estimates. As can be seen from the figure, the perturbed flux $F'_r$ totally dominates the change in luminosity, which is larger by a factor of a few hundred when $F'_r$ is taken into account compared to the case where only $\xi_r$ contributes.

In the perturbed convection case, the amplitude of the brightness variation is proportional to $P^{-2}$ in both the calculations with and without $F'_r$. For the frozen convection case and for periods under 10 days, the scaling of the amplitude is closer to $\propto P^{-3}$, although the calculation only including $\xi_r$ is slightly shallower than the full calculation.

The transit depth of a planet of similar radius to Jupiter would be $\sim 1$ per cent, which is a similar order of magnitude to the amplitude of the signal for $P = 1$ day for the perturbed convection model (including $F'_r$ in the brightness calculation). At $P = 4$ days, the amplitude of the tidal signal is a factor of $\sim 25$ smaller than the transit depth, at $\sim 400$ ppm. The frozen convection model predicts an amplitude of $\sim 0.1$ per cent at $P = 1$ day, and $\sim 20$ ppm at $P = 4$ days. This order of magnitude difference between the two models of convection is maintained as the orbital period changes. This is due to the fact that, within the convection zone, the assumption of frozen convection causes the flux to be greatly suppressed before growing over a very

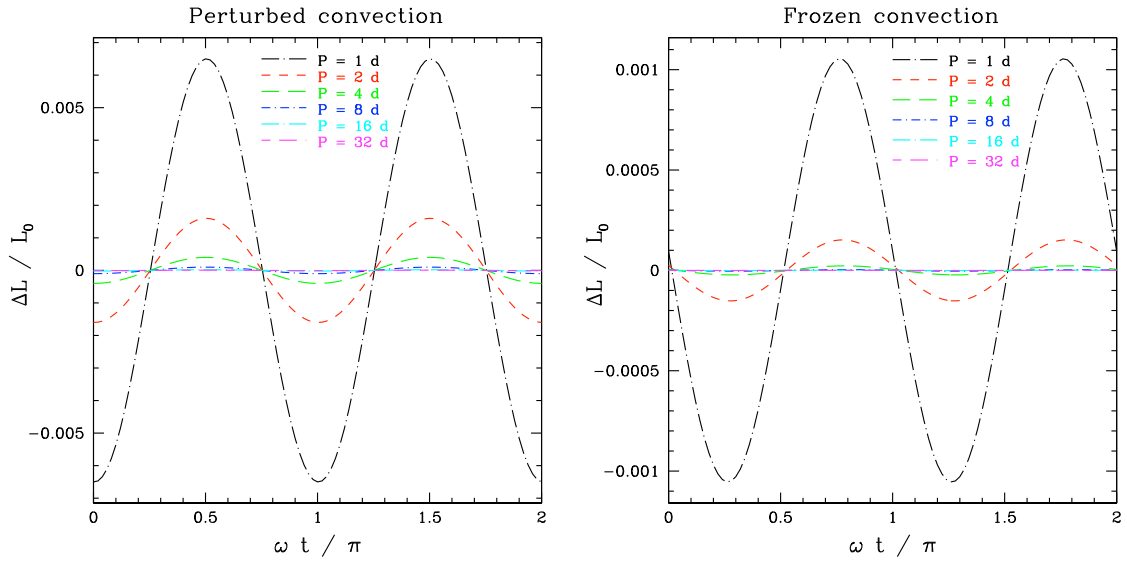


Figure 4.5: The photometric signal as a fraction of total luminosity, $\Delta L/L_0$, is shown against orbital phase for a range of orbital periods for both the perturbed convection model (left panel) and the frozen convection model (right panel). From the largest to the smallest amplitude, the different curves correspond to $P$=1, 2, 4, 8, 16 and 32 days. In both models, the phase remains fairly constant over this range of periods. In the perturbed convection case, the amplitude scales as $P^{-2}$, whereas in the frozen convection case the amplitude scaling is closer to $P^{-3}$. The perturbed convection model produces a prediction which is a factor of $\sim 5$ greater than the frozen convection model and, at very short periods, has a large peak–to–peak amplitude, being $\sim$ 1 per cent at $P = 1$ day, which is comparable to the transit depth of a planet of similar size to Jupiter. Because of the scaling with $P$, this quickly drops to a very small signal for long period orbits, being $\sim 100$ ppm at $P = 8$ days.

small scale when approaching the thin radiative skin. By contrast, in the perturbed convection case, the flux grows over a large scale throughout the convection zone.

This difference in the change in luminosity between the frozen and perturbed convection models is still present when only $\xi_r$ contributes to $\Delta L/L_0$, as can be seen in Figure 4.6, although its is smaller than when $F_r'$ contributes. When only $\xi_r$ contributes, the signal at $P = 1$ day has an amplitude of $\sim 10$ ppm in the perturbed convection model, and $\sim 3$ ppm in the frozen convection model. At $P = 4$ days, these are reduced to 0.6 and 0.1 ppm respectively, where the frozen convection model has slightly deviated from the $P^{-2}$ scaling.

The phase of the luminosity variations does not vary hugely with orbital period, with the perturbed convection model predicting that the real component of the luminosity variation will dominate at all orbital periods. The frozen convection case differs from this, with the imaginary component dominating at long period orbits for the signal from $F_r'$, with the signal from $\xi_r$ gradually changing in phase as the orbital period changes.

### 4.4.5 The effect of stellar mass

A more massive star of 1.4 $M_\odot$ was also investigated, as the stellar structure changes non–linearly with mass, leading to changes in the behaviour of the oscillations both throughout the star and at the surface. Structurally, the primary difference is the distribution of convective regions – there is a small convective region at the centre of the star, and the outer convective region is significantly thinner than in the 1 $M_\odot$ case (its base is at $r = 0.94R$ compared to $r = 0.73R$ in the lower mass star), as shown in Figure 3.2.

Computationally, the presence of the small convective core gives rise to resolution issues at the inner boundary of the radiative zone, which leads to an unphysically large response at that point in the star for short period orbits. However, since the very centre of the star is convective, short–wavelength spatial oscillations are eliminated in that region, contrary to the lower stellar mass case.

The star's response to a resonance is also affected. Changing the resonant cavity affects the location and spacing of the resonances, though they still have a similarly high quality factor. The response at the surface is much more sensitive to the presence of a resonance in the 1.4 $M_\odot$ case, as the thinner outer convective region means that the surface is much less insulated from the resonating radiative zone. In this case, a resonance can give an order of magnitude increase in both the RV and photometric signals.

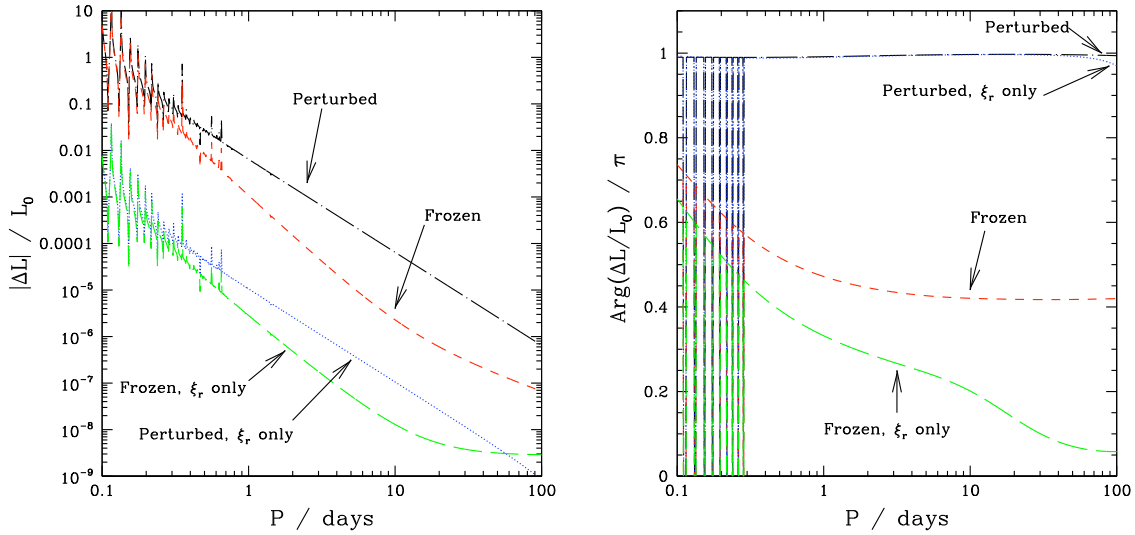


Figure 4.6: The magnitude (left panel) and phase (right panel) of the photometric signal $\Delta L/L_0$ is shown against orbital period for a Jupiter–mass planet orbiting a solar–mass star. The four different curves correspond to the full photometric signal and perturbed convection (dashed dotted black lines) or frozen convection (small dashed red lines) and to the signal arising from $\xi_r$ only and perturbed convection (dotted blue lines) or frozen convection (long dashed green lines). In the perturbed convection case, the magnitude is proportional to $P^{-2}$, whereas for the frozen convection case, and for periods under 10 days, the scaling with $P$ is steeper than this, being closer to $P^{-3}$. For periods under 1 day, resonances are seen to have a significant effect. Outside of this region, the full signal from the frozen model is an order of magnitude smaller than that from the perturbed convection model. At very short periods, both models predict unreasonably large values, and the assumption of small perturbations is clearly no longer valid there. The signals arising only as a result of $\xi_r$ show a similar relationship, but are smaller than the full signal by a factor of $10^2 - 10^3$ (with the magnitude of the full signal being $\sim 10^{-2}$ and that of the signal due only to $\xi_r$ being $\sim 10^{-5}$ at $P = 1$ day). The phase of the signals arising from the perturbed convection model remain constant outside of the resonances. By contrast, the frozen convection model does exhibit some change in phase as both the real and imaginary components are of roughly similar size, with some variation as the orbital period changes.

Table 4.1: The parameters of the modelled systems, as derived from observations. Listed are the name of the system, the stellar mass M in solar mass, the planet's mass $m_p$ in Jupiter masses, the stellar radius $R$ in solar radius, the age of the system in Gyr, the orbital semi–major axis $a$ in au, the orbital period $P$ and the rotational period $P_{\rm rot}$ in days. Other than the rotational periods, the data were taken from Arras et al. (2012). Rotational periods came from Alsubai et al. (2017) (Qatar 5), Howarth & Morello (2017) (KOI-13), Brown et al. (2011) (WASP-19 and WASP-18), and Csizmadia et al. (2011) (CoRoT-17, although this number is uncertain it was found to be "typical of a main-sequence slow–rotating star").

| System | $M$ ($M_\odot$) | $m_p$ ($M_J$) | R ($R_\odot$) | age (Gyr) | a (au) | P (d) | $P_{\rm rot}$ (d) |
|---|---|---|---|---|---|---|---|
| WASP-19 | 0.97 | 1.17 | 0.99 | 11.5 | 0.016 | 0.79 | 10.5 |
| WASP-18 | 1.24 | 10.11 | 1.36 | 0.63 | 0.020 | 0.94 | 5.6 |
| KOI-13 | 1.72 | 9.28 | 1.74 | ? | 0.063 | 1.76 | 1.06 |
| Qatar 5 | 1.13 | 4.32 | 1.08 | 0.53 | 0.041 | 2.88 | 12.1 |
| CoRoT-17 | 1.04 | 2.43 | 1.59 | 10.7 | 0.046 | 3.77 | 20 |

In general, for a given period, the photometric response is a factor of 3 smaller than in the 1 $M_\odot$ case, whilst the RV signal is approximately an order of magnitude greater. The change in luminosity $\Delta L$ still scales with the perturbation, and is proportional to $P^{-2}$ in the perturbed convection case. Other than for very short periods, $V$ is constant, and dominates the RV signal, so that $v_{\rm disc} \propto P^{-1}$, as in the 1 $M_\odot$ case.

## 4.5 Application to observed systems

We now model some specific systems in order to produce specific predictions. Table 4.1 lists the key parameters of the systems, which have been approximately recreated in the model. These cases were chosen in order to show the behaviour of observable signals over a range of system parameters. Since the eccentricity of these systems is negligible, the semi–major axis $a$ is equal to what has been called the separation $D$ in this work.

Each of the systems, except KOI–13, exhibits a rotational period which is at least a factor of 4 larger than the orbital period, such that the approximation of a non–rotating star is not unreasonable.

The details of the response are given in Table 4.2, which gives the surface behaviour, and how it converts into disc–integrated observables assuming a perfectly edge–on orbit (which is approximately true, as all five systems were discovered by transit).

Table 4.2: The results of the model applied to the real systems, for both the perturbed convection and frozen convection cases. The columns, from left to right, give the system in question, the radial equilibrium displacement $\xi_{r,\mathrm{eq}}$ at the surface, the radial displacement $\xi_r$ at the surface, the tangential displacement $V$ at the surface, the orbital radial–velocity (RV) semi–amplitude $K_{\mathrm{orb}}$, the disc–integrated RV velocity $\mathrm{v}_{\mathrm{disc,eq}}$ in the equilibrium tide case, the disc–integrated RV velocity $\mathrm{v}_{\mathrm{disc}}$ for the full solution, and the fractional change in disc–integrated luminosity $\Delta L/L_0$ (semi-amplitude), respectively.

| System | $10^{-3}\times\xi_{r,\mathrm{eq}}$ (cm) | $10^{-3}\times\xi_r$ (cm) | $10^{-3}\times V$ (cm) | $K_{\mathrm{orb}}$ (m s$^{-1}$) | $\mathrm{v}_{\mathrm{disc,eq}}$ (m s$^{-1}$) | $\mathrm{v}_{\mathrm{disc}}$ (m s$^{-1}$) | $\times\Delta L/L_0$ (ppm) |
|---|---|---|---|---|---|---|---|
| WASP-19, perturbed | 440 | $(400-9\mathrm{i})$ | $-(460+103\mathrm{i})$ | 260 | $-2.7\mathrm{i}$ | $-0.46+1.25\mathrm{i}$ | $(-14000+250\mathrm{i})$ |
| WASP-19, frozen | 440 | $-(70+190\mathrm{i})$ | $-(5770+2170\mathrm{i})$ | 260 | $-2.7\mathrm{i}$ | $-9.7+24.9\mathrm{i}$ | $(-400+5000\mathrm{i})$ |
| WASP-18, perturbed | 5800 | $(5460-190\mathrm{i})$ | $-(1700+1580\mathrm{i})$ | 1800 | $-29\mathrm{i}$ | $-5.9+0.1\mathrm{i}$ | $(-130000+4000\mathrm{i})$ |
| WASP-18, frozen | 5800 | $-(820+1950\mathrm{i})$ | $-(52400+15600\mathrm{i})$ | 1800 | $-29\mathrm{i}$ | $-0.59+1.9\mathrm{i}$ | $(-500+35300\mathrm{i})$ |
| KOI-13, perturbed | 2000 | $-(604+4\mathrm{i})$ | $-(52500+80\mathrm{i})$ | 1000 | $-5.25\mathrm{i}$ | $-0.14+92.5\mathrm{i}$ | $(-40+90\mathrm{i})$ |
| KOI-13, frozen | 2000 | $-(430+20\mathrm{i})$ | $-(49100+340\mathrm{i})$ | 1000 | $-5.25\mathrm{i}$ | $-0.6+86\mathrm{i}$ | $(-20+170\mathrm{i})$ |
| Qatar 5, perturbed | 120 | $(109-3\mathrm{i})$ | $-(1170+440\mathrm{i})$ | 570 | $-0.20\mathrm{i}$ | $-0.52+1.32\mathrm{i}$ | $(-3500+90\mathrm{i})$ |
| Qatar 5, frozen | 120 | $-(9+10\mathrm{i})$ | $-(18100+1400\mathrm{i})$ | 570 | $-0.20\mathrm{i}$ | $-1.6+21.3\mathrm{i}$ | $(40+180\mathrm{i})$ |
| CoRoT-17, perturbed | 230 | $(220+9\mathrm{i})$ | $-(840+607\mathrm{i})$ | 320 | $-0.32\mathrm{i}$ | $-0.58+0.71\mathrm{i}$ | $(-3300+130\mathrm{i})$ |
| CoRoT-17, frozen | 230 | $-(20+26\mathrm{i})$ | $-(16300+1700\mathrm{i})$ | 320 | $-0.32\mathrm{i}$ | $-1.6+15.6\mathrm{i}$ | $(40+250\mathrm{i})$ |

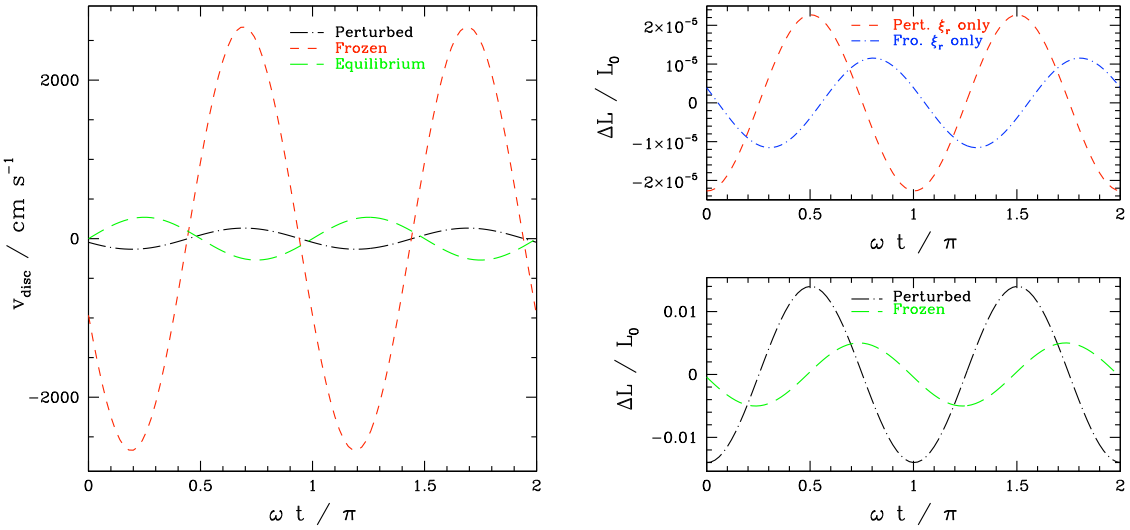


Figure 4.7: WASP–19: the left panel shows the RV signal in units of cm s$^{-1}$ for the cases of perturbed convection (black dot-dash line), frozen convection (red dash line), and the equilibrium tide (green long dash line); the right panels show the luminosity variation. These quantities are plotted against the orbital phase. The top right panel shows the luminosity variation resulting only from the change in $\xi_r$ for the perturbed convection case (red dash line) and the frozen convection case (blue dot-dash line). The bottom right panel shows the complete luminosity variation, including the flux perturbation, for the perturbed convection case (black dot-dash line) and the frozen convection case (green dash line).

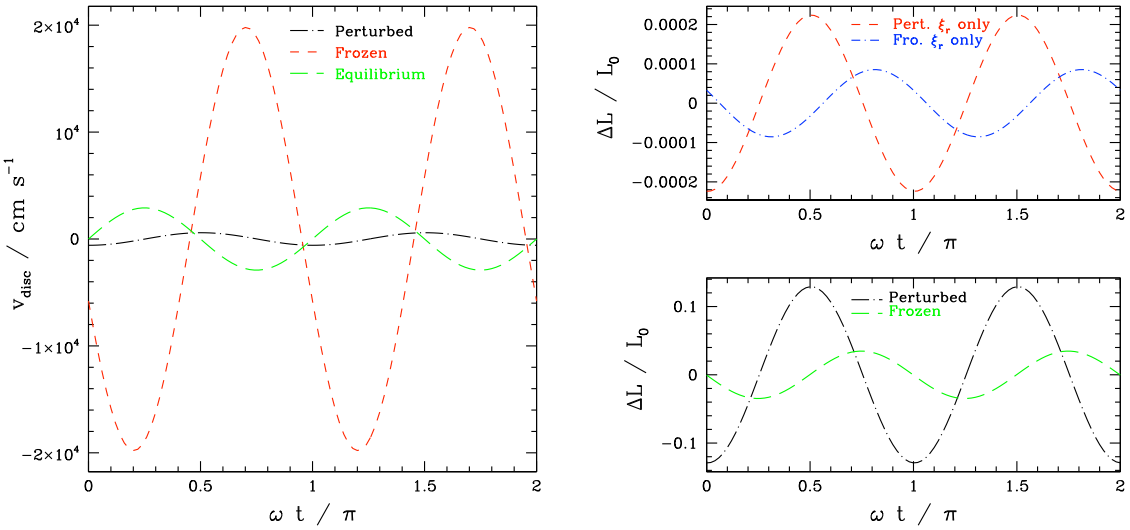


Figure 4.8: Same as Figure 4.7 but for WASP–18.

### 4.5.1 WASP–19

Results for this system are displayed in Figure 4.7. This system has a very short period orbit, such that $\xi_{r,\mathrm{eq}} \sim |V|$ for the perturbed convection model. The predicted RV signal for this case is a factor of two smaller than the equilibrium tide prediction, and is almost in anti–phase with it as a result of the fact that $V \approx -V_{\mathrm{eq}}$. Therefore, the radial and tangential components of the displacement counteract each other, reducing the disc–integrated signal.

The frozen convection case is dominated by a large value of $V$, and is approximately an order of magnitude greater than the equilibrium tide prediction. The phase matches the perturbed convection prediction, and is therefore also in anti–phase with the equilibrium tide prediction.

The luminosity variation predicted is very large, with an amplitude of $\sim 1$ per cent for both the perturbed and frozen convection cases, which is the order of magnitude of the transit depth for a Jupiter analogue. Calculating the brightness variation arising only from $\xi_r$, that is to say neglecting the contribution from $F_r'$, predicts amplitudes which are smaller by a factor of $\sim 10^3$. In both cases, the perturbed convection case is dominated by the real component, whereas the frozen convection case is dominated by the imaginary component. The arguments therefore differ by a factor of $\pi/2$, giving a clear phase difference in the observable signal.

### 4.5.2 WASP-18

Results for this system are displayed in Figure 4.8. The very massive, short period planet gives rise to a large equilibrium tide RV response of $\sim 30$ m s$^{-1}$. This is a factor of $\sim 5$ greater than the perturbed convection model's response ($\sim 6$ m s$^{-1}$), though it is still around an order of magnitude smaller than the frozen convection model's prediction ($\sim 200$ m s$^{-1}$). As the stellar model used here has a resonance close to the oscillation frequency, the values given in Table 4.2 for this system could vary significantly for a small change in the orbital period modelled, and if on resonance could give very large values.

The perturbation to the flux within the star is very large in both the perturbed and frozen convection models, being $\sim 0.13$ and $\sim 0.04$, respectively. This would likely break the assumption of small perturbations, and therefore this model – particularly the prediction for the luminosity variation – may not be reliable.

If the contribution from only $\xi_r$ is taken into account, the luminosity variation is still fairly large ($\sim 10^{-4}$). The perturbed convection model prediction is similar to the expectation from the equilibrium tide, as $\xi_r \approx \xi_{r,\mathrm{eq}}$. The frozen convection prediction is smaller by a factor of 2, and is phase shifted compared to both the equilibrium tide and the perturbed convection prediction.

### 4.5.3 KOI-13

The system KOI–13 involves a very massive planet on a short period orbit around a massive star. Although the equilibrium tide is large, the horizontal displacement is larger still by more than an order of magnitude. This results in a large RV signal, but the structure of the star towards the surface (a radiative envelope, with a couple of thin convective regions towards the very surface) seems to make the response difficult to model, and very sensitive to the orbital frequency. Moreover, the rotation period of the star is greater than the orbital period of the planet, and the system is likely in a 5:3 spin–orbit resonance (Szabó et al., 2012). Given the large rotation period, this system cannot be expected to be reliably modelled within the assumptions we have made.

### 4.5.4 Qatar 5

Results for this system are displayed in Figure 4.9. The Qatar 5 system has a star which is very similar to the Sun in terms of structure, with a fairly massive planet on a short period orbit. As the orbital period is varied, the surface displacement behaves in

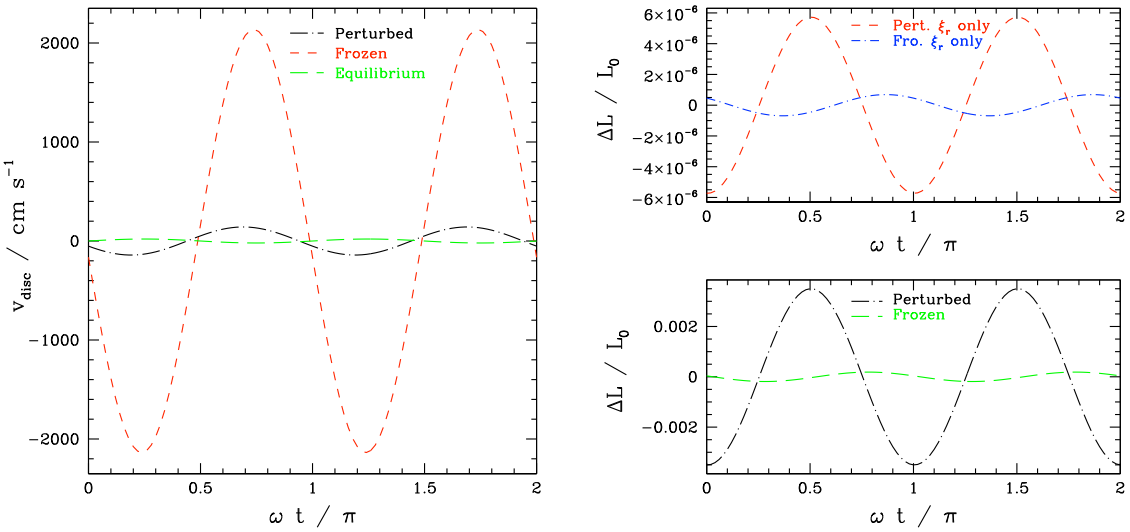


Figure 4.9: Same as Figure 4.7 but for Qatar 5.

a way similar to what what described in section 4.4. In the perturbed convection case, the radial displacement tracks the equilibrium tide well, whilst the frozen convection prediction is an order of magnitude smaller. In both cases, the tangential displacement is fairly insensitive to the forcing frequency. At the orbital period of the real system, we expect a greater RV signal than predicted by the equilibrium tide as a result of the tangential displacement being increased by a factor of $\sim 10$ for the perturbed convection case, and $\sim 100$ for the frozen convection case. The frozen convection amplitude of 20 m s$^{-1}$ would be much more easily detectable than the equilibrium tide prediction, and even the perturbed convection prediction of 2 m s$^{-1}$ is potentially detectable.

The luminosity variation $\Delta L$ for the perturbed convection model is an order of magnitude greater than, and out of phase with, the same quantity for the frozen convection model. This applies whether or not $F_r'$ is taken into account in the calculation of $\Delta L$. The phase difference could be used to distinguish between the perturbed and frozen convection models.

### 4.5.5 CoRoT–17

The star in the CoRoT–17 system is similar to an aged Sun, which has expanded. The increased stellar radius would be expected to lead to a greater response to the tidal potential. The star maintains a radiative core surrounded by a convective envelope, with a thin radiative skin at the very surface. The radial displacement once

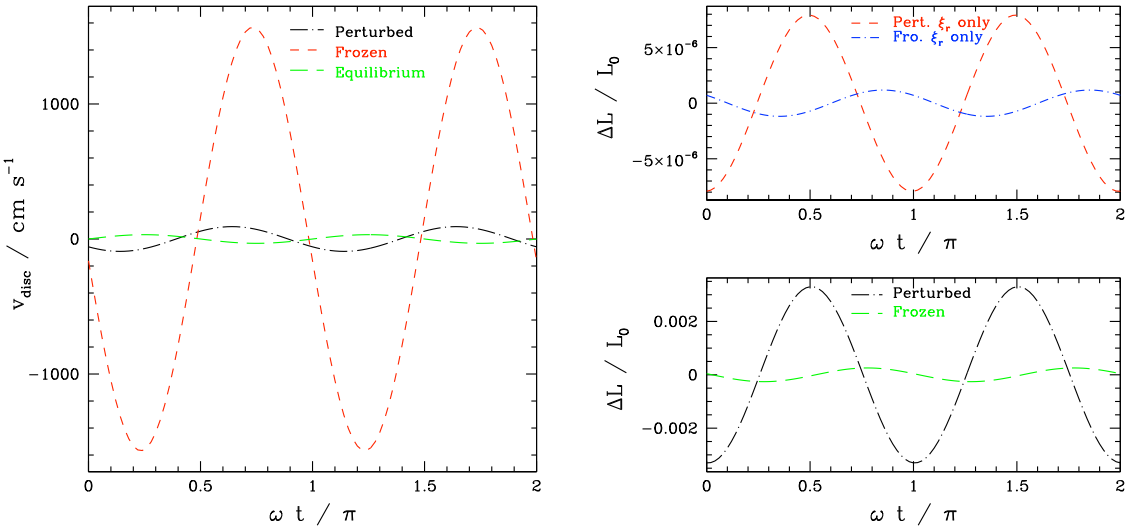


Figure 4.10: Same as Figure 4.7 but for CoRoT–17.

again closely tracks the equilibrium tide prediction, whilst the tangential displacement remains fairly insensitive to the orbital period.

The large radius of the star gives a large prediction for the equilibrium radial displacement, given the comparatively long period orbit. The perturbed convection case matches this prediction fairly well, giving rise to a fairly small discrepancy between $\xi_r$ and $V$: only a factor of $\sim 5$. The frozen convection model predicts a much greater discrepancy, as the radial displacement is an order of magnitude smaller than the equilibrium tide prediction, and the horizontal displacement is a factor of $\sim 16$ greater than the perturbed convection model's prediction.

Overall, this results in a RV prediction from the perturbed convection model which is a factor of $\sim 3$ greater than the equilibrium tide prediction ($\sim 90$ cm s$^{-1}$ compared to $\sim 30$ cm s$^{-1}$). On the other hand, the frozen convection model predicts a signal a factor of $\sim 50$ greater than the equilibrium tide, at $\sim 16$ m s$^{-1}$. Each of the three cases has a different phase, which could help to distinguish between the different behaviours.

The photometric variation is very similar to that of Qatar 5 b, with the perturbed convection case predicting a luminosity variation which is an order of magnitude greater than the frozen convection prediction, whether including $F_r'$ or just $\xi_r$. The prediction taking $F_r'$ into account should be detectable, at $\sim 10^{-3}$, and is three orders of magnitude greater than the prediction which includes $\xi_r$ only, which would be very difficult to detect.

### 4.5.6 Non–disc–integrated signals

#### 4.5.6.1 Signals during transit

The profiles for the radial velocity signal blocked by the planet over the course of a transit are shown in Figure 4.11. This shows only the value of the radial velocity blocked against time, and not the depth of the transit at that value of $v_{RV}$.

The curves in Figure 4.11 show the predictions for the perturbed convection model and the equilibrium tide prediction applied to WASP-18, Qatar 5 and CoRoT-17. In each case the perturbed convection curves are significantly different to the equilibrium tide prediction, whilst similarities between the different systems are apparent.

The deviation from the equilibrium tide comes from the difference in $V$ from the equilibrium tide prediction, as in each of these systems the imaginary component of $V$ is not negligible, and the magnitude of $V$ differs from $\xi_{r,\mathrm{eq}}$ (for WASP-18 it is smaller than expected, for the other two systems it is significantly larger than expected). If time-resolved spectra are able to detect signals such as these, the radial velocity signal originating from a specific, known point on the stellar surface could be isolated. This would enable the profile of the radial velocity along the path of the transit to be broken down into its spatial components in order to separate the radial and tangential contributions and directly exposing the form of the oscillations.

#### 4.5.6.2 Time-dependent line broadening

The potential range of time-dependent line broadening signals are initially explored for CoRoT–17 as an example system. This is shown in Figure 4.12, where some extreme cases have been plotted as examples, as well as the unchanged calculation for CoRoT–17, to provide context, called "Full calculation" in the figure. This reference case is dominated by $V$, and this is taken as the reference value, $V_{\mathrm{ref}}$, in order to keep the signals all of a similar scale. The case where $\xi_r = V_{\mathrm{ref}}$, "Equal parts", imitates the equilibrium tide case, where $V$ and $\xi_r$ are expected to be of equal magnitude. "Only V" refers to the calculation where $\xi_r$ is set to 0, only keeping the tangential motion as a source of line–broadening – emulating the extremely long–period orbit case where the signal is totally dominated by $V$. The final curve, "Rescaled $\xi_r$", gives the oscillation of the IQR for the case that $\xi_r = V_{\mathrm{ref}}$ and $V = 0$, to demonstrate the shape of the broadening resulting from the radial component of the displacement.

The difference in constant offset of the IQR would not differentiate between these signals, as the background broadening would be indistinguishable from it. The oscillating signal, however, could become detectable owing to its time-dependence and

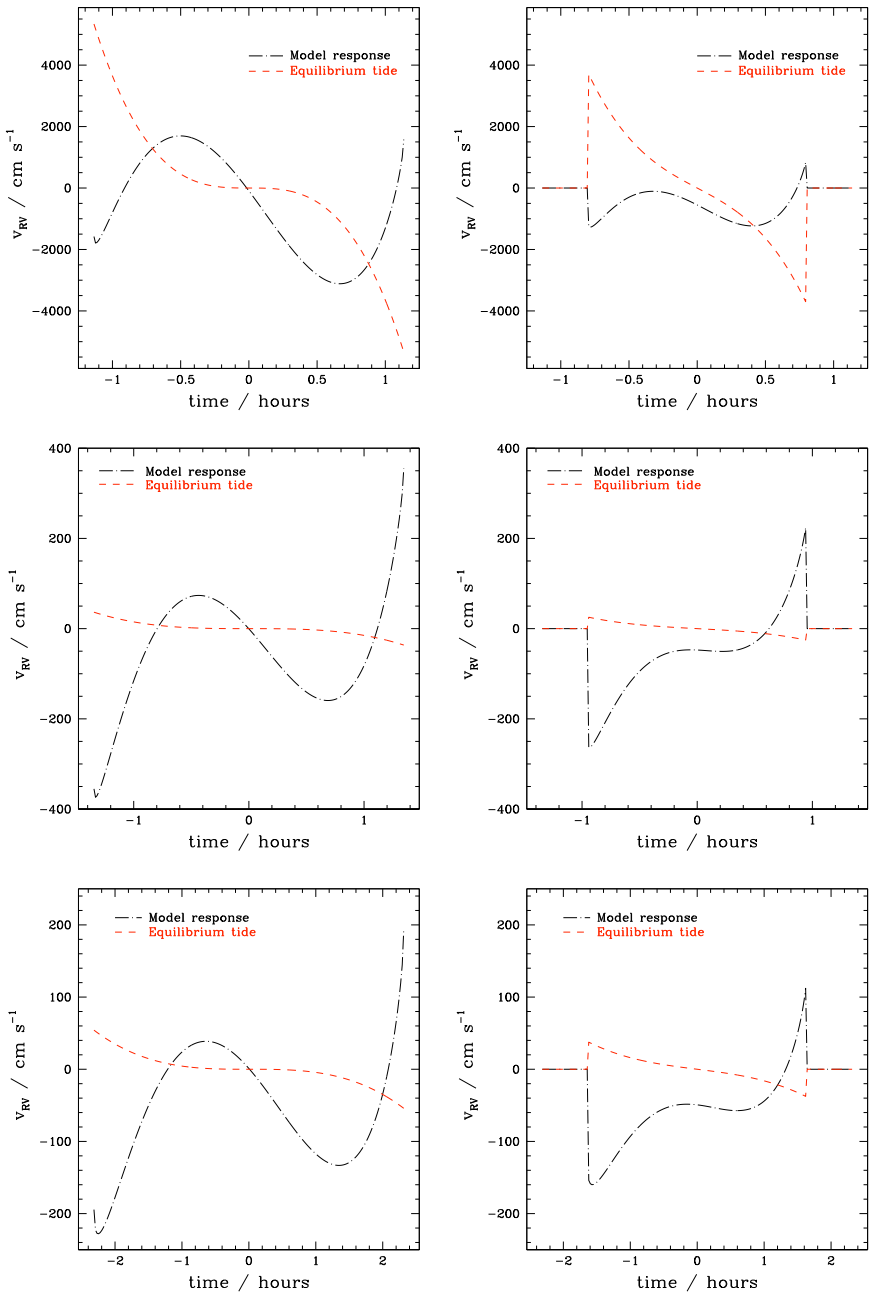


Figure 4.11: This figure shows the radial velocities blocked by the planets over the course of a transit, causing a dip in brightness at the corresponding location in the line–shape, for the perturbed convection model applied to WASP-18 (top), Qatar 5 (middle) and CoRoT-17 (bottom). The left column shows the case that the planet is transiting exactly edge-on, such that the blocked portion of the star is at $\theta_* = \pi/2$. The right column shows the case that the system is not exactly edge-on, such that the portion of the star that is blocked is at $\theta_* = \pi/4$. The contrast between the equilibrium tide and the modelled response (with perturbed convection) is significant in each case. The diversity of possible curves is also apparent.

having a long coherence length (as long as the planet's orbit and the stellar structure are unaffected).Comparing these extreme examples it is clear that different combinations of $\xi_r$ and $V$ produce different signals, with the "Equal parts" case producing a significantly larger signal than any other. In each case the signal is non-zero, and therefore, for a large enough displacement at the surface, some kind of time-dependent broadening signal would be expected, and observing its shape could give information about the nature of the oscillation.

The predicted peak-to-peak amplitude for the oscillation for the "Full calculation" case is approximately 7 cm, which is a very small signal to detect, although it would be expected that for systems with more massive planets on shorter-period orbits that this signal could be significantly larger.

The time-dependent variation in the line–width is shown in Figure 4.13 for the four systems we have been exploring, in the "Full Calculation" case as described above. Note that the sub-figures all have different scales on the y-axis, but that the variation is around $\sim 10\%$ of the constant value in each case. The amplitude of the variation correlates loosely with the magnitude of $v_{\mathrm{RV}}$, although the exact relationship does depend on the relationship between $\xi_r$ and $V$.

In each case the line–width varies periodically, with a period equal to $P/4$, and appears to be roughly sinusoidal. This may be a result of choosing to use the IQR as the single parameter by which to describe the shape, as the exact change in shape will differ in each case. Nevertheless, this simple description highlights the periodic change in broadening, and gives a sense of the magnitude of the variation over time.

## 4.6 Discussion

The response of a star being perturbed by a nearby companion may be significantly different to that predicted by a simple equilibrium approximation, due to the presence of non–adiabatic behaviour towards the stellar surface. This could lead to observable signals which greatly differ from those predicted from the equilibrium tide.

At the surface, the horizontal displacement is found to tend to a constant value, independent of the orbital period. For long orbital periods, where the horizontal displacement dominates over the radial displacement, this results in the magnitude of the radial velocity scaling as $P^{-1}$, instead of $P^{-3}$ for the equilibrium tide. Therefore, for long orbital periods, the radial velocity is much greater than expected from the equilibrium tide.

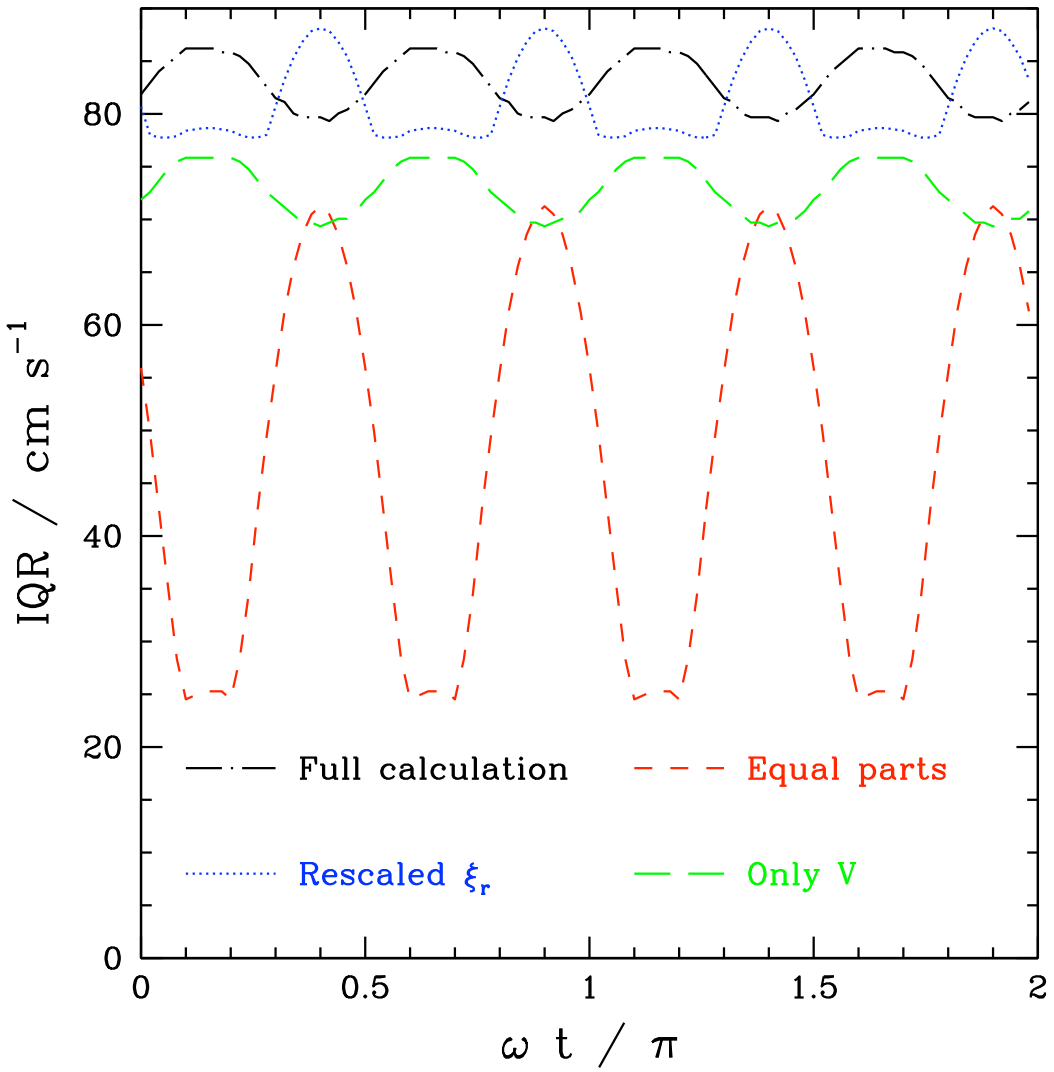


Figure 4.12: The inter-quartile range (IQR) of the line-broadening (in cm s$^{-1}$) resulting from CoRoT-17 b is shown against orbital phase. The unchanged calculation for CoRoT-17 is plotted to provide context, called "Full calculation" in the figure. The reference case is dominated by $V$, and this is taken as the reference value, $V_{\rm ref}$, in order to keep the signals all of a similar scale. The case where $\xi_r = V_{\rm ref}$, "Equal parts", imitates the equilibrium tide case, where $V$ and $\xi_r$ are expected to be of equal magnitude. "Only V" refers to the calculation where $\xi_r$ is set to 0, only keeping the tangential motion as a source of line-broadening – emulating the extremely long-period orbit case where the signal is totally dominated by $V$. The final curve, "Rescaled $\xi_r$", gives the oscillation of the IQR for the case that $\xi_r = V_{\rm ref}$ and $V = 0$, to demonstrate the shape of the broadening resulting from the radial component of the displacement. All signals oscillate with a period of $P/4$, but with different magnitudes. The difference in the constant offset of this oscillation would not be observable, as it would be taken to be part of the constant background line-broadening.

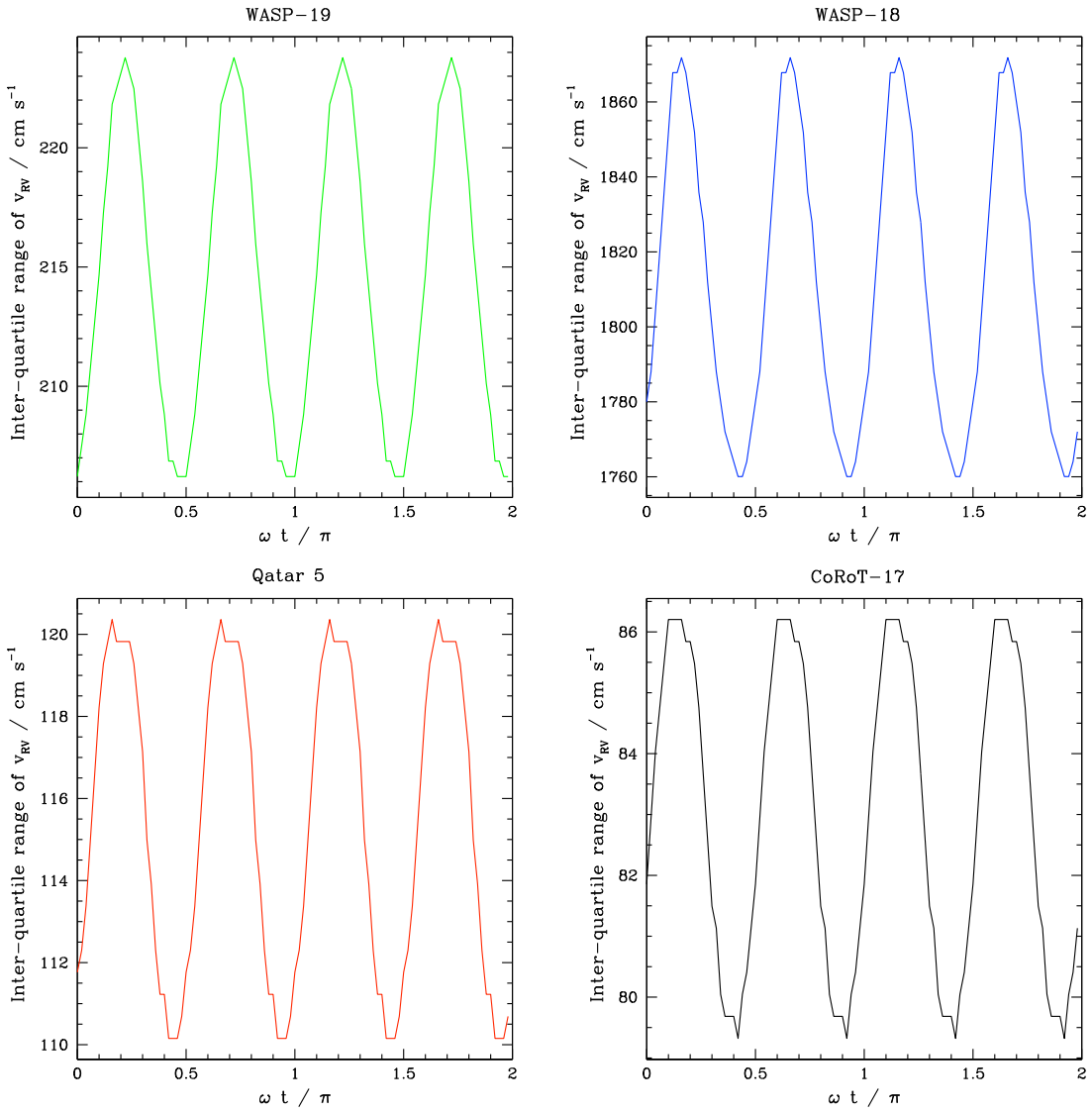


Figure 4.13: This figure shows the time-dependent variation in line-broadening by plotting the inter-quartile range (IQR) of the radial velocity – showing the width of the range of velocities over which the central 50% of the brightness is emitted. In each case the IQR oscillates about a constant value with a period of $P/4$. In each case the amplitude of the oscillations is $\sim 10\%$ of the constant value. Whilst this constant background broadening would not be distinguishable from other sources of constant broadening, the periodicity of the variation could make it possible to detect the variation in broadening.

This constant value is attained for orbital periods where $|\xi_{r,\mathrm{eq}}| \lesssim |V|$, and therefore breaks down for ultra–short period planets. For those, the predicted RV signal may be smaller than expected from the equilibrium tide, and the scaling with period reverts to roughly match the $P^{-3}$ of the equilibrium tide. The phase of the RV signal is also generally found to differ from the equilibrium tide, as the RV signal is dominated by the real and negative component of $V$, leading to a signal which is roughly inverted compared to the equilibrium tide.

The photometric variation is found to have the same scaling as predicted by the equilibrium tide, being proportional to $P^{-2}$, which holds whether $F_r'$ is taken into account or not in the calculation of the luminosity change. If $F_r'$ is included, the magnitudes predicted can become very large, which are likely to be overestimates of the real signal. If only the contribution from the radial displacement is included, the luminosity variation is smaller by three orders of magnitude. In this case, the perturbed convection model matches well with the equilibrium tide prediction, as $\xi_r \approx \xi_{r,\mathrm{eq}}$, though the frozen convection prediction is several times smaller than this. For very short period orbits, the value of $F_r'$ is likely inaccurate, as it can become large and the assumption of small perturbations in the model would no longer be valid. The phase of the prediction using perturbed convection matches the equilibrium tide prediction (whether $F_r'$ is included or not), though the frozen convection case does not – this could potentially be used to distinguish between the two models using observations.

Near resonances the response of the stellar surface can depend strongly on the orbital frequency of the companion. In order to correctly capture this resonant behaviour, the resonant frequencies of the model must match those of the real star. As the resonances depend upon the structure of the star as a whole, matching the stellar model to the real resonant frequencies can be difficult, particularly if the stellar properties are not tightly constrained. In general, we would still expect deviation from the equilibrium tide near resonances. Whilst this is unlikely to be observed for periods greater than a day, where resonances are very narrow, it could be seen at very short periods, where the resonances are wider.

Whilst the above behaviours are found to be common to both the frozen convection and perturbed convection models, the specific predictions made for a system depend strongly upon the choice of model used for the convective flux. Both models have different virtues, with the frozen convection approach providing a baseline comparison without complicating the model by perturbing a process as non–linear and non–local as convection. However, the artificial suppression of the stellar response within the

convection zone does give rise to very large gradients in a thin region just below the surface, once the radiative flux begins to become significant. The perturbed flux approach was designed to describe the behaviour in the superadiabatic zone towards the top of the convective zone, and therefore is well suited to model the non–adiabatic effects in the region where convection becomes inefficient. Deep in the convection zone, this approach may not be applicable, as the entropy gradient is very shallow and errors may accumulate, giving rise to overly large flux perturbations at the surface. Overall, it is likely that both approaches fall short of reality, but they can be used to provide insight into the range of possible behaviours, and the dependence of the stellar response on the model of convection, whilst highlighting the deviation from the equilibrium tide.

The planets modelled in this work with periods under one day exhibited similar behaviour. Both WASP–19 and WASP–18 produced RV signals that were smaller than predicted by the equilibrium tide in the perturbed convection model, whilst the frozen convection model predicted a signal much larger than $v_{RV,eq}$. If observed, this signal would therefore enable the different models to be distinguished from each other. The predictions for the photometric variation were also very large, with the signal taking the perturbed flux into account on the order of $1-10$ per cent. If the flux were overestimated and the change in luminosity were mainly due to the radial displacement, the signal would still be potentially detectable, at $10-10^2$ ppm. In fact, the signal arising for WASP-18 b from $\xi_r$ only, in the perturbed convection case, agrees reasonably well with the $\sim 190$ ppm semi-amplitude given in Shporer et al. (2019).

A radial velocity signal at twice the orbital frequency has been detected for WASP–18 b (Triaud et al., 2010). This was attributed to a non–zero eccentricity, although this explanation was disputed by Arras et al. (2012) who favoured the tidal oscillation as the source. Later, work by Maciejewski et al. (2020a) has suggested that the tidal signal has an amplitude of $\sim 18$ m s$^{-1}$, which is smaller than predicted by the equilibrium tide by a factor of two, and approximately a factor of three larger than the perturbed convection prediction in this work. The phase of the observations more closely matches the equilibrium tide prediction, with very little or no offset compared to the orbital motion RV signal.

For the longer period planets, Qatar 5 and CoRoT–17, the perturbed convection model predicts signals $\sim 1$ m s$^{-1}$, with the prediction from the frozen convection model being an order of magnitude larger. Both values are larger than the RV signal expected from the equilibrium tide. The photometric variation from the flux is around

0.1 per cent, and would therefore be expected to be observable, whilst the signal arising only from the radial displacement would be much more difficult to detect, at $\sim 1$ ppm. Measurements in the detection of both Qatar 5–b (Alsubai et al., 2017) and CoRoT–17 b (Csizmadia et al., 2011) do not constrain either the photometric variation or the RV signal to the level where either of these signal would be clearly visible.

The tidal RV signal is effectively a second order effect of the planet, compared to the first order effect which is used in the radial velocity method for detecting exoplanets as described in as described in section 1.4.1. We would expect the amplitude of the tidal signal to be much smaller than the orbital radial velocity amplitude. In the equilibrium tide case we would expect this disparity to increase sharply as the orbital distance increases, as we would expect $\frac{v_{RV}}{K_{orb}} \propto (\frac{R}{D})^4$. For the non-adiabatic case, where the RV response is dominated by a constant $V$, this scaling would change, giving the ratio as $\frac{v_{RV}}{K_{orb}} \propto \frac{R}{D}$, although the constant of proportionality would also be expected to change (Bunting et al., 2019). As a result, detecting tidal RV signals for planets with orbital periods of more than a few days may be more achievable than previously thought.

The benefit of detecting both RV signals is clearest when a transit is not observed, and the orbital inclination is unknown. In that case the planetary mass is unknown, although $m_p \sin(i)$ will have been determined from $K_{orb}$. It may then be possible to infer a value for $m_p \sin^2(i)$ from the tidal signal, breaking the degeneracy between $m_p$ and $i$.

A comparison between the magnitude of the photometric variation to the transit depth is not so straightforward, as the mechanisms are not as linked as in the RV case. Moreover, the transit depth is independent of the orbital separation. The primary limitation of the transit method – that the planet must pass between the star and the observer – is not so strictly relevant to the tidal signal. In the transit method the transit depth drops rapidly to 0 as the inclination of the system deviates from this arrangement by more than a small angle, $\delta\theta \approx \frac{R}{D}$, such that only a small fraction of systems will be observed (see section 1.4.2 for more details). The magnitude of the tidal signal depends on $\sin^2(\theta_0) = \cos^2(\delta\theta)$, and will be maximised for a system which is viewed exactly edge-on. However, $\delta\theta$ can vary between $\pm\pi/4$ with the observed magnitude being at least 50 per cent of the maximum value. Therefore the proportion of orientations with amplitudes above this threshold is equal to $1/\sqrt{2} \approx 0.7$. As a result, if a system produces a large photometric signal, it would be plausible to observe such a system over a wide range of inclinations, which gives rise to the

possibility of photometrically detecting non-transiting planets, just as discussed in Faigler & Mazeh (2011).

If a planet is already well characterised within a system, accurately modelling the tidal signals could still be worthwhile. On top of providing an independent mass estimate as a check, the second order signals arising due to the known planet could be modelled and removed from the observations in order to make detecting other planets within the system easier. This might be particularly important for a less massive planet within the Hot Jupiter's orbit, such as observed by (Huang et al., 2020).

The non–disc–integrated methods for observing these tidal oscillations could provide useful insight into the nature of the tidal oscillations themselves, as the signal during transit and the time–dependent broadening both give signals which depend separately on $\xi_r$ and $V$. Detecting the signal during transit would require spectra to be taken quickly, and with a short cadence, which would be best suited for nearby, bright stars. In order to build up the SNR it would also be useful to capture many transits, and therefore a short period orbit would be preferable. The time–dependent broadening signal would be difficult to detect due to the many other sources of line–broadening, with a comparatively small variation. However, the long coherence length expected from the tidal signal could be taken advantage of by using observations taken over a long time in order to average out the other sources of broadening, and detect the coherent underlying variation, small though it is.

Whilst it may be simple to show that a system is deviating from the equilibrium tide, more work would be required in order to investigate the scaling of the behaviour with orbital period, amongst other parameters. Future work would be required in order to make testable predictions for systems which could be observed, and particularly for distinguishing between the non–adiabatic models and the equilibrium tide approximation.

Observations of the photometric signal arising from a tidal perturbation would give very useful constraints on the model used for the convective flux, and would help improving the model as a whole.

# Chapter 5

# Conclusion

Over the course of this thesis we have shown the importance of including non-adiabatic effects in modelling the response of a star to a tidal perturbation, particularly at the stellar surface. The behaviour within the body of the star is not significantly changed by the inclusion of non-adiabatic effects, however, and does not seem to deviate significantly from the equilibrium tide. In a region close to the surface, where the thermal timescale is similar to or less than the oscillation timescale, we expect that non-adiabatic behaviour will be present. The work here builds upon previous work (such as Terquem et al. (1998)), as the fully non-adiabatic stellar oscillation equations are solved to model the response of the star, without needing to assume that non-adiabatic effects are small.

The exact location at which non-adiabatic effects become apparent, as well as the quantitative response at the surface, depend upon the model used to perturb the convective flux. We describe the perturbation to the convective flux using a model which assume the flux perturbation arises due to the perturbation to the entropy gradient. This is expected to be most significant in the upper convective region (where convection becomes inefficient). Although the model is necessarily a greatly simplified approach to convection, it allows a simple, local approach to the perturbed convective flux which is expected to well describe the behaviour in the region where non-adiabatic effects are most prevalent. It may fall short in the deep convective zone, however, giving rise to anomalously large values for the perturbation to the flux at the surface. Investigating this, and methods to overcome this, would be a topic for future work. Previous work has been done to model the flux perturbation in a tidally perturbed star (Pfahl et al. (2008); Fuller (2017)) although this has assumed that convection remains efficient throughout the entire convection zone, effectively suppressing non-adiabatic effects in the upper convection zone and in the radiative skin.

Whilst the method used in this thesis has some shortcomings, it does avoid enforcing an adiabatic response by providing a plausible model for the perturbation to the flux. This enables the potential impact of non-adiabatic effects to be explored. Observations of tidally-induced photometric variations could be used to distinguish between the contribution from the flux perturbation and the radial displacement. This would enable different models for the convective flux perturbation to be compared and improved.

The divergence of the horizontal displacement from the equilibrium tide prediction at the stellar surface has been shown to be a robust result, as the behaviour is present regardless of the choice of model for the perturbed convective flux. This aligns well with the analytical estimate which predicts that $V$ will be constant, independent of the orbital period of the perturber (as long as the condition that $\xi_{r,eq} \lesssim V$ holds true, which is valid for periods greater than $\sim 1$ day). Calculating the observable signal arising from the surface motion, as done by Dziembowski (1977), this leads to a change in the predicted scaling with orbital period, $P$, as the equilibrium tide gives $|v_{\mathrm{RV}}| \propto P^{-3}$, whilst the non-adiabatic solution gives $|v_{\mathrm{RV}}| \propto P^{-1}$ as the motion is dominated by the constant $V$.

The observable signals were discussed through the lens of specific systems, based on those previous modelled by Arras et al. (2012) where the equilibrium tide approximation was used to give predictions for the radial velocity variation. The equilibrium tide predictions we calculate here agree well with those given in Arras et al. (2012), allowing for a small discrepancy in the exact stellar model used. However, the non-adiabatic behaviour we find at the stellar surface suggests that the observable signals may be significantly different from the predictions based on the equilibrium tide. In particular, planets with orbital periods of a few days, such as Qatar 5 b and CoRoT–17 b, may produce much larger signals than would otherwise be expected. Conversely, planets with ultra–short period orbits, such as WASP–19 b and WASP–18 b, are expected to have lower RV amplitudes than predicted by the equilibrium tide. Observations of systems such as these would enable the scaling of the RV tidal signal with orbital period to be investigated, such that the influence of non-adiabatic effects at the surface could be detected.

Non–disc–integrated methods could be used to give clear evidence of deviation from the equilibrium tide, and to separate the contributions from the radial and horizontal displacements, either using the RV signal during a transit or by observing the time–dependent line–broadening signal, as initially alluded to by Robinson et al.

(1982). This would enable the surface behaviour to be more deeply investigated, such that models for convection could be more precisely compared against reality.

The work done here could also be further generalised to include stellar rotation and non-zero eccentricity to enable the tidal signals of a wider range of systems to be modelled. Stellar binaries could also be modelled, enabling two sources of oscillations to be observed simultaneously.

Observations of tidally induced variation, both photometric and spectroscopic, could be used to constrain the parameters of observed systems, including providing an independent estimate of the planetary mass if the system is already constrained. If a system is not already well–constrained, the tidal RV signal could be used to break the mass–inclination degeneracy. Photometric variation could also be used to detect non-transiting planets outright. Attributing such a signal unambiguously to a planetary perturber may be difficult owing to the various potential sources of stellar variability, although the tidal signal would be expected to remain coherent for an effectively indefinite length of time, such that sources of noise would be expected to become incoherent, enabling the tidal signal to be detected.

Overall, the equilibrium tide approximation has been shown to be inadequate when applied to the stellar surface, and the importance of non-adiabatic effects has been demonstrated. Accurate modelling of this would enable new avenues of investigation and characterisation of exoplanets, potentially using only one method of observation, or even data which already exist.

# Appendix A

# The horizontal displacement and the equilibrium tide

Expressing the horizontal displacement as $\boldsymbol{\xi}_\perp = r\boldsymbol{\nabla}_\perp V$, where $V$ has the same dependences upon $\theta$ and $\phi$ as the other variables under consideration (see section 3.2.2), gives the continuity equation as:

$$\rho' + \frac{1}{r^2}\frac{\partial}{\partial r}\left(r^2\rho_0\xi_r\right) - \rho_0\frac{l(l+1)V}{r} = 0, \tag{A.1}$$

where we have used the fact that $V \propto Y_l^{-m}(\theta,\phi)$ such that $\nabla_\perp^2 V = -l(l+1)V/r^2$. Using $\Delta\rho = 0$, this can be rearranged and simplified to give

$$V = \frac{r}{l(l+1)}\left(2\frac{\xi_r}{r} + \frac{\partial\xi_r}{\partial r}\right). \tag{A.2}$$

To examine the behaviour towards the surface, we use the approximation that $g = GM/r^2$, where $G$ is the gravitational constant, and $M$ is the stellar mass. This approximation is increasingly valid as we approach the surface due to the low density of surface material. Combining this with the expression for $\Phi_\mathrm{P}$ gives the radial displacement as:

$$\xi_r = \frac{m_\mathrm{P} r^4}{4MD^3}. \tag{A.3}$$

This then gives the horizontal displacement function as:

$$V \approx \frac{3m_\mathrm{P} r^4}{2l(l+1)MD^3}, \tag{A.4}$$

which, combined with the fact that $l = 2$, gives the result that $V = \xi_r$ towards the surface. Importantly, the scale of variation of these quantities is of the order of the radius.

As mentioned already, this was derived under the assumptions of hydrostatic equilibrium, applying in the limit $m\omega \to 0$, and that either the perturbations are adiabatic or the Lagrangian variation of the density and pressure are zero with $N^2 \neq 0$. However, a different situation arises when both $m^2\omega^2$ and $N^2$ are small and tend to zero simultaneously. This is potentially significant in convection zones in which the convective heat transport is efficient as in the inner solar convective envelope. This is explored in the appendices of Bunting et al. (2019).

# Appendix B

# Stellar Oscillation Equations

This is a record of the basic equations from which the non-adiabatic non-radial oscillation equations are derived. Overall the process is fairly simple – the equations are linearised assuming small perturbations to the spherically symmetric, time-independent equilibrium state. This appendix details that process.

## B.1 Assumptions

The following assumptions are adopted in order to derive a set of governing equations for the forced response problem:

1. Time independence of the background: the equilibrium state of the star changes on a timescale much longer than the period of the oscillations.

2. Spherical symmetry: the equilibrium structure of the star is spherically symmetric, parametrised only as a function of radius. This is assumed to apply after horizontal averaging in convection zones.

3. Non-rotating star: this approximation is valid if the rotational period of the star is much longer than the orbital period of the planet.

4. Cowling approximation: the perturbation to the gravitational potential of the star is neglected, which is justified in the outer regions of the star which has low density and in the inner parts of the star where the wavelength of the oscillatory response is small.

5. Small perturbations: the departures from equilibrium are everywhere small such that the linear regime is a valid approximation.

## B.2 Linearising

To study effects of infinitesimal perturbations to the system, the variables are expanded into their equilibrium and perturbed components, such as $q = q_0 + q'$, for some variable, $q$. The equilibrium quantities themselves satisfy the fluid equations, so cancel out. Terms which are second order in perturbed quantities are taken to be negligible, because the perturbation is assumed to be small. This leaves only terms which are linear in perturbed quantities.

Looking at the perturbed velocity in particular, and recalling that the equilibrium state is taken to be static, we see that $\boldsymbol{u} = 0 + \boldsymbol{u}'$. We can re-express this in terms of $\boldsymbol{\xi}$, the displacement from equilibrium ($\boldsymbol{\xi} = \boldsymbol{r} - \boldsymbol{r}_0$). Relating the Lagrangian and Eulerian descriptions of the perturbed velocity gives:

$$\Delta \boldsymbol{u} = \boldsymbol{u}' + (\boldsymbol{\xi} \cdot \boldsymbol{\nabla})\boldsymbol{u}_0 \longrightarrow \Delta \boldsymbol{u} = \boldsymbol{u}', \tag{B.1}$$

which shows that the perturbed velocity is the same in both the Eulerian and Lagrangian descriptions.

We can then use this to relate the displacement to the perturbed velocity, as

$$\Delta \boldsymbol{u} = \boldsymbol{u}(\boldsymbol{r}_0 + \boldsymbol{\xi}) - \boldsymbol{u}(\boldsymbol{r}_0) = \frac{d\boldsymbol{r}}{dt} - \frac{d\boldsymbol{r}_0}{dt} = \frac{d}{dt}(\boldsymbol{r} - \boldsymbol{r}_0) = \frac{d}{dt}\boldsymbol{\xi}, \tag{B.2}$$

and as $\Delta \boldsymbol{u} = \boldsymbol{u}'$, we can also say that $\boldsymbol{u} = \frac{\partial \boldsymbol{\xi}}{\partial t}$.

## B.3 Continuity equation

The continuity equation is a result from the conservation of mass, and can be expressed as

$$\frac{\partial \rho}{\partial t} + \boldsymbol{\nabla} \cdot (\rho \, \boldsymbol{u}) = 0, \tag{B.3}$$

where $\rho$ is the density. This is linearised to

$$\frac{\partial}{\partial t}\left(\rho' + \boldsymbol{\nabla} \cdot (\rho_0 \boldsymbol{\xi})\right) = 0, \tag{B.4}$$

using the fact that the equilibrium quantities are time-independent to bring the partial time derivative outside the brackets.

## B.4 Momentum equation

This equation arises from examining the forces acting on a fluid element, given as

$$\rho\left(\frac{\partial}{\partial t}+\boldsymbol{u}\cdot\boldsymbol{\nabla}\right)\boldsymbol{u}=\rho\boldsymbol{f}-\boldsymbol{\nabla}p-\rho\boldsymbol{\nabla}\Phi+\boldsymbol{\nabla}\cdot\hat{\Pi}, \tag{B.5}$$

where $p$ is the pressure, , $\Phi$ is the gravitational potential, $\boldsymbol{f}$ is the EM and external forces per unit volume, and $\hat{\Pi}$ is the viscous stress tensor. In this case, $\boldsymbol{f}$ and $\hat{\Pi}$ may be neglected, as the fluid is almost an ideal gas, is charge neutral, and the only external influence is gravitational, which is taken into account by $\Phi$.

Linearising this, we use the Cowling approximation to use the substitution $\Phi = \Phi_0 + \Phi_P$. This gives

$$\rho_0\frac{\partial^2\boldsymbol{\xi}}{\partial t^2}=-\boldsymbol{\nabla}p'-\rho_0\boldsymbol{\nabla}\Phi_P-\rho'\boldsymbol{\nabla}\Phi_0. \tag{B.6}$$

## B.5 Energy equation

This equation arises from considering the release and flux of energy and can be expressed as

$$\rho T\left(\frac{\partial}{\partial t}+\boldsymbol{u}\cdot\boldsymbol{\nabla}\right)s=\rho\left(\varepsilon_N+\varepsilon_\nu\right)-\boldsymbol{\nabla}\cdot\boldsymbol{F}, \tag{B.7}$$

where $s$ is the specific entropy, $\varepsilon_N$ is the specific nuclear energy generation rate, $\varepsilon_\nu$ is the specific rate of release of heat due to viscosity, and $\boldsymbol{F}$ is the total energy flux.

In linearising, we neglect both $\varepsilon_N$ and $\varepsilon_\nu$, as we expect the nuclear energy generation rate to be insensitive to the small perturbations (and nuclear energy generation will only occur in a small region at the core, where oscillations are expected to be smallest) and we are neglecting viscosity still, resulting in

$$\rho_0 T_0\frac{\partial}{\partial t}\left(s'+\boldsymbol{\xi}\cdot\boldsymbol{\nabla}s_0\right)=s-\boldsymbol{\nabla}\cdot\boldsymbol{F}. \tag{B.8}$$

## B.6 Energy flux

These equations are necessary to relate variables to each other, particularly in terms of gradients of equilibrium quantities.

First, we have the express the radiative flux, $\boldsymbol{F}_{\text{rad}}$ using the radiative diffusion equation (see section 3.1.1) as

$$\boldsymbol{F}_{\text{rad}} = -K\boldsymbol{\nabla}T, \tag{B.9}$$

where $K = \frac{4ac_*}{3\kappa\rho}T^3$, where $a = \frac{4\sigma}{c_*} = 7.5657 \times 10^{-15}$ erg cm$^{-3}$ K$^{-4}$ is the radiation density constant ($\boldsymbol{\sigma}$ is the Stefan-Boltzmann constant), $c_*$ is the speed of light (the subscript-asterisk is to differentiate it from the sound speed) and $\boldsymbol{\kappa}$ is the opacity.

Linearising will give us

$$\boldsymbol{F}'_{\text{rad}} = -K'\boldsymbol{\nabla}T_0 - K_0\boldsymbol{\nabla}T' \tag{B.10}$$

and

$$\frac{K'}{K_0} = 3\frac{T'}{T_0} - \frac{\kappa'}{\kappa_0} - \frac{\rho'}{\rho_0}. \tag{B.11}$$

We must also find a relation for the change in opacity, the change in density, and the change in specific entropy, in terms of the variables of state which we are most interested in. For the most part, this means expressing total derivatives in terms of $p$ and $T$, but not always – this is largely dictated by the derivatives which are available through MESA.

For the opacity, we express it as $\kappa = \kappa(\ln(\rho), \ln(T))$, which gives us

$$d\kappa = \left(\frac{\partial\kappa}{\partial\ln\rho}\right)_T d(\ln\rho) + \left(\frac{\partial\kappa}{\partial\ln T}\right)_\rho d(\ln T), \tag{B.12}$$

which is linearised to give

$$\kappa' = \left(\frac{\partial\kappa}{\partial\ln\rho}\right)_T \frac{\rho'}{\rho_0} + \left(\frac{\partial\kappa}{\partial\ln T}\right)_\rho \frac{T'}{T_0}, \tag{B.13}$$

which is left in this form, as the partial derivatives in this form are available as an output from MESA.

Similarly, the convective flux, $\boldsymbol{F}_{\rm c}$, as expressed as in equation 2.14, is

$$\boldsymbol{F}_{\rm c} = -\hat{\boldsymbol{r}} A \hat{\boldsymbol{r}} \cdot \boldsymbol{\nabla} s, \tag{B.14}$$

which is linearised to give

$$\boldsymbol{F}'_{\rm c} = -\boldsymbol{\Delta}\hat{\boldsymbol{n}}_{\rm c} A_0 \hat{\boldsymbol{r}} \cdot \boldsymbol{\nabla} s_0 - \hat{\boldsymbol{r}} A' \hat{\boldsymbol{r}} \cdot \boldsymbol{\nabla} s_0 - \hat{\boldsymbol{r}} A_0 \boldsymbol{\Delta}\hat{\boldsymbol{n}}_{\rm c} \cdot \boldsymbol{\nabla} s_0 - \hat{\boldsymbol{r}} A_0 \hat{\boldsymbol{r}} \cdot \boldsymbol{\nabla} s', \tag{B.15}$$

where $\boldsymbol{\Delta}\hat{\boldsymbol{n}}_{\rm c}$ is the perturbation to the direction of the convective flow, which is perpendicular to $\hat{\boldsymbol{r}}$ to first order. As $s_0$ only varies in the radial direction, the third term on the right hand side is equal to 0. To simplify this expression, we assume that the perturbation to the convective flux will be dominated by the entropy gradient in the non-adiabatic region where we expect $\boldsymbol{F}'_{\rm c}$ to be important. Therefore we set $A' = 0$.

Whilst it is possible to include the non-radial component of equation B.15 in the divergence of the energy flux, we make simplifying assumption that perturbation to the convective flux is dominated by the radial component, as we expect $s'$ to change over a small radial scale, and to avoid the complexity required in calculating the change in the direction in convection as a result of both the perturbation to the gravitational field and the perturbation to the horizontal entropy gradient. This gives the final expression for the perturbation to the total flux as

$$\boldsymbol{F'} = -K' \boldsymbol{\nabla} T_0 - K_0 \boldsymbol{\nabla} T' - \hat{\boldsymbol{r}} A_0 \frac{\partial s'}{\partial r}. \tag{B.16}$$

## B.7 Thermodynamic equations

Two more equations are required to relate a couple of specific quantities to the variables of interest. Both the specific entropy and the density are taken to be functions of $T$ and $p$, and their total derivatives are expanded accordingly. This gives rise to:

$$ds = \left(\frac{\partial s}{\partial p}\right)_T dp + \left(\frac{\partial s}{\partial T}\right)_p dT, \tag{B.17}$$

and we substitute in $c_p = T\left(\frac{\partial s}{\partial T}\right)_p$ and $\nabla_{ad} = \left(\frac{\partial \ln T}{\partial \ln p}\right)_s = \frac{p_0}{T_0}\left(\frac{\partial T}{\partial p}\right)_s$ used in conjunction with the triple product rule to give

$$s' = -\left(\frac{\partial s}{\partial T}\right)_p \left(\frac{\partial T}{\partial p}\right)_s p' + \left(\frac{\partial s}{\partial T}\right)_p T' = -\frac{c_p}{T_0}\frac{T_0}{p_0}\nabla_{ad} p' + \frac{c_p}{T_0} T', \tag{B.18}$$

which then leaves us with

$$s' = c_p \left( \frac{T'}{T_0} - \nabla_{ad} \frac{p'}{p_0} \right). \tag{B.19}$$

Similarly, for the density, we introduce $\chi_\rho \equiv \left( \frac{\partial \ln p}{\partial \ln \rho} \right)_T$ and $\chi_T \equiv \left( \frac{\partial \ln p}{\partial \ln T} \right)_\rho$, and once again use the triple product rule to give

$$\begin{aligned} d\ln\rho = \left( \frac{\partial \ln \rho}{\partial \ln p} \right)_T d\ln p + \left( \frac{\partial \ln \rho}{\partial \ln T} \right)_p d\ln T \\ = \left( \frac{\partial \ln \rho}{\partial \ln p} \right)_T \frac{p'}{p_0} - \left( \frac{\partial \ln \rho}{\partial \ln p} \right)_T \left( \frac{\partial \ln \rho}{\partial \ln T} \right)_\rho \frac{T'}{T_0}, \end{aligned} \tag{B.20}$$

which can be finally expressed as

$$\frac{\rho'}{\rho_0} = \frac{1}{\chi_\rho} \left( \frac{p'}{p_0} - \chi_T \frac{T'}{T_0} \right), \tag{B.21}$$

which completes the set of equations which we need.

## B.8 List of linearised equations

We are then left with the following linearised equations, which will then need to be cut down such that solving the system becomes a practical task. The equations are:

$$\frac{\partial}{\partial t} \left( \rho' + \boldsymbol{\nabla} \cdot (\rho_0 \boldsymbol{\xi}) \right) = 0, \tag{B.22}$$

$$\rho_0 \frac{\partial^2 \boldsymbol{\xi}}{\partial t^2} = -\boldsymbol{\nabla} p' - \rho_0 \boldsymbol{\nabla} \Phi_P - \rho' \boldsymbol{\nabla} \Phi_0, \tag{B.23}$$

$$\rho_0 T_0 \frac{\partial}{\partial t} \left( s' + \boldsymbol{\xi} \cdot \boldsymbol{\nabla} s_0 \right) = -\boldsymbol{\nabla} \cdot \boldsymbol{F'}, \tag{B.24}$$

$$\boldsymbol{F'} = -K' \boldsymbol{\nabla} T_0 - K_0 \boldsymbol{\nabla} T' - \hat{\boldsymbol{r}} A_0 \frac{\partial s'}{\partial r}, \tag{B.25}$$

$$\frac{K'}{K_0} = 3\frac{T'}{T_0} - \frac{\kappa'}{\kappa_0} - \frac{\rho'}{\rho_0}, \tag{B.26}$$

$$\kappa' = \left(\frac{\partial \kappa}{\partial \ln \rho}\right)_T \frac{\rho'}{\rho_0} + \left(\frac{\partial \kappa}{\partial \ln T}\right)_\rho \frac{T'}{T_0}, \tag{B.27}$$

$$s' = c_p \left(\frac{T'}{T_0} - \nabla_{ad} \frac{p'}{p_0}\right), \tag{B.28}$$

and

$$\frac{\rho'}{\rho_0} = \frac{1}{\chi_\rho}\left(\frac{p'}{p_0} - \chi_T \frac{T'}{T_0}\right). \tag{B.29}$$

This is a 12D set of equations, with the associated twelve variables being: $p'$, $T'$, $\boldsymbol{\xi}$, $\boldsymbol{F}'$, $\rho'$, $s'$, $K'$ and $\kappa'$. The four variables which we desire to remain once the equations have been linearly combined are $p', T', \xi_r$ and $F_r'$ where the subscripted $r$ denotes the radial component of the vector quantity.

Before jumping in to do the combining, we define what kind of solutions we will be looking for. Because the equations are all linear and have time-independent coefficients, we can separate the time dependence from the spatial dependence, so can then look for wave solutions of the form $e^{im\omega t}$ such that $\frac{\partial q'}{\partial t} = im\omega q'$, where $q'$ is some perturbed variable.

We are also looking for solutions which are in the form of spherical harmonics, such that they obey the equation:

$$\nabla_\perp^2 q' = -\frac{l(l+1)}{r^2} q' \tag{B.30}$$

where $\boldsymbol{\nabla}_\perp = \boldsymbol{\nabla} - \hat{r}\frac{\partial}{\partial r}$, and therefore $\nabla_\perp^2 A = \nabla^2 A - \frac{1}{r^2}\frac{\partial}{\partial r}\left(r^2 \frac{\partial A}{\partial r}\right)$. Note that the equilibrium variables are purely radial, so $\boldsymbol{\nabla}_\perp q_0 = 0$.

## B.9 Eliminating variables

In order to make use of the properties of spherical harmonics, the equations must be formed in such a way as to ensure that $\nabla_\perp$ only appears as $\nabla_\perp^2$. To do this, the vector equations must be split into their radial and tangential components, and the divergence terms must also be split into the radial and tangential parts. Also, we can use the time dependence of oscillatory solutions to immediately replace partial time derivatives with $im\omega$. This affects equations B.22 to B.25, giving:

$$\rho' + \frac{1}{r^2}\frac{\partial}{\partial r}(r^2 \rho_0 \xi_r) + \rho_0 \boldsymbol{\nabla}_\perp \cdot \boldsymbol{\xi}_\perp = 0, \tag{B.31}$$

$$-m^2\omega^2\rho_0\xi_r = -\frac{\partial p'}{\partial r} - \rho_0\frac{\partial \Phi_P}{\partial r} - \rho'\frac{\partial \Phi_0}{\partial r}, \tag{B.32}$$

$$-m^2\omega^2\rho_0\boldsymbol{\xi}_\perp = -\boldsymbol{\nabla}_\perp p' - \rho_0\boldsymbol{\nabla}_\perp\Phi_P, \tag{B.33}$$

$$im\omega\rho_0 T_0\left(s' + \xi_r\frac{\partial s_0}{\partial r}\right) = -\frac{1}{r^2}\frac{\partial}{\partial r}(r^2F_r') - \boldsymbol{\nabla}_\perp\cdot\boldsymbol{F}'_\perp, \tag{B.34}$$

$$F_r' = -K'\frac{\partial T_0}{\partial r} - K_0\frac{\partial T'}{\partial r} - A_0\frac{\partial s'}{\partial r}, \tag{B.35}$$

and

$$\boldsymbol{F}'_\perp = -K_0\boldsymbol{\nabla}_\perp T', \tag{B.36}$$

where the variables have been decomposed into their radial and tangential components, as $\boldsymbol{q}' = \hat{r}q_r' + \boldsymbol{q}'_\perp$.

Substituting equation B.33 into B.31, and B.36 into B.34 and then using the relation given in B.30 gives

$$\rho' + \frac{1}{r^2}\frac{\partial}{\partial r}(r^2\rho_0\xi_r) - \frac{l(l+1)}{r^2}\left(\frac{p'}{m^2\omega^2} + \frac{\rho_0\Phi_P}{m^2\omega^2}\right) = 0 \tag{B.37}$$

and

$$im\omega\rho_0 T_0\left(s' + \xi_r\frac{\partial s_0}{\partial r}\right) = -\frac{1}{r^2}\frac{\partial}{\partial r}(r^2F_r') - K_0\frac{l(l+1)}{r^2}T' \tag{B.38}$$

Substituting equation B.29 into B.37 gives us

$$\frac{1}{r^2}\frac{\partial}{\partial r}(r^2\rho_0\xi_r) + \left(\frac{\rho_0}{\chi_\rho p_0} - \frac{l(l+1)}{m^2\omega^2r^2}\right)p' - \frac{\rho_0}{T_0}\frac{\chi_T}{\chi_\rho}T' = \frac{l(l+1)}{m^2\omega^2r^2}\rho_0\Phi_P \tag{B.39}$$

which is the first of our oscillation equations, as it has only the desired variables.

By substituting equation B.28 into B.38 we get

$$\left(i\rho_0 m\omega c_p + \frac{l(l+1)}{r^2}K_0\right)T' - \left(im\omega c_p\nabla_{ad}\rho_0 T_0\right)\frac{p'}{p_0} + im\omega\rho_0 T_0\frac{\partial s_0}{\partial r}\xi_r + \frac{1}{r^2}\frac{\partial}{\partial r}(r^2F_r') = 0 \tag{B.40}$$

which is the second of our oscillation equations.

Using equations B.26, B.27, B.28 and B.29 by substituting them into equation B.35 results in:

$$-\frac{F_r'}{K_0}+\left(-\frac{\partial}{\partial r}+\frac{1}{T_0}\frac{\partial T_0}{\partial r}\left[-3+\frac{1}{\kappa_0}\left(\frac{\partial\kappa}{\partial\ln T}\right)_\rho-\frac{\chi_T}{\chi_\rho}\left(1+\frac{1}{\kappa_0}\left(\frac{\partial\kappa}{\partial\ln\rho}\right)_T\right)\right]\right)T'$$
$$+\frac{\partial T_0}{\partial r}\frac{1}{p_0\chi_\rho}\left(1+\frac{1}{\kappa_0}\left(\frac{\partial\kappa}{\partial\ln\rho}\right)_T\right)p'+\frac{\mathrm{d}r}{\mathrm{d}s_0}\frac{F_{c,r,0}}{K_0}\frac{\mathrm{d}}{\mathrm{d}r}\left(c_p\frac{T'}{T_0}\right)-\frac{\mathrm{d}r}{\mathrm{d}s_0}\frac{F_{c,r,0}}{K_0}\frac{\mathrm{d}}{\mathrm{d}r}\left(\nabla_{ad}\frac{p'}{p_0}\right)=0 \tag{B.41}$$

which gives us the penultimate oscillation equation, where we have used the background convective flux as $F_{c,r,0}=-A_0\frac{\partial s_0}{\partial r},$.

To get the final equation, substitute equation B.29 into B.32, giving

$$-m^2\omega^2\rho_0\xi_r+\left(\frac{\partial}{\partial r}+\frac{\rho_0}{\chi_\rho p_0}\frac{\partial\Phi_0}{\partial r}\right)p'-\frac{\partial\Phi_0}{\partial r}\frac{\rho_0}{T_0}\frac{\chi_T}{\chi_\rho}T'=-\rho_0\frac{\partial\Phi_P}{\partial r} \tag{B.42}$$

which completes the set of four equations for four unknowns: equations B.39, B.40, B.41, and B.42. However, the final equations should be in terms of dimensionless variables in order to avoid any unit-related issues of numbers being much too big or much too small, which could lead to truncation errors or other difficulties. We therefore introduce the variables:

$$\tilde{\xi}_r\equiv\frac{\xi_r}{R}, \tag{B.43}$$
$$\tilde{F}_r\equiv\frac{F_r}{F_{r_{BC}}}, \tag{B.44}$$
$$\tilde{p}\equiv\frac{p}{p_0}, \tag{B.45}$$
$$\tilde{T}\equiv\frac{T}{T_0}, \tag{B.46}$$

where $F_{r_{BC}}=F_{r_0}|_{r=R}$. Using these definitions and equations B.39, B.40, B.41 and B.42, and then by making the equations dimensionless (but avoiding any potential singularities) we come to:

$$\frac{1}{\rho_0 R}\frac{\partial}{\partial r}\left(\rho_0 r^2\tilde{\xi}_r\right)+\left(\frac{r^2}{\chi_\rho R^2}-\frac{l(l+1)p_0}{m^2\omega^2R^2\rho_0}\right)\tilde{p}-\frac{\chi_T}{\chi_\rho}\frac{r^2}{R^2}\tilde{T}=\frac{l(l+1)r^2f}{m^2\omega^2R^2}, \tag{B.47}$$

$$iA_{\mathrm{BV}}\frac{\chi_\rho}{\chi_T}\frac{r}{R}\tilde{\xi}_r+\frac{F_{r_{BC}}}{m\omega\rho_0T_0c_pR^2}\frac{\partial}{\partial r}\left(r^2\tilde{F}_r\right)-i\nabla_{ad}\frac{r^2}{R^2}\tilde{p}+\left(i\frac{r^2}{R^2}+\frac{l(l+1)K_0}{\rho_0m\omega c_pR^2}\right)\tilde{T}=0, \tag{B.48}$$

$$-\frac{F_{r_{BC}}}{K_0}\frac{\partial r}{\partial T_0}\tilde{F}_r+\frac{1}{\chi_\rho}\left(1+\frac{1}{\kappa_0}\left(\frac{\partial\kappa}{\partial\ln\rho}\right)_T\right)\tilde{p}$$
$$+\left(-4+\frac{1}{\kappa_0}\left(\frac{\partial\kappa}{\partial\ln T}\right)_\rho-\frac{\chi_T}{\chi_\rho}\left(1+\frac{1}{\kappa_0}\left(\frac{\partial\kappa}{\partial\ln\rho}\right)_T\right)\right)\tilde{T}-T_0\frac{\partial\tilde{T}}{\partial T_0}$$
$$+\frac{\partial r}{\partial T_0}\frac{F_{c,r,0}}{K_0}\frac{r\chi_T}{c_pA_{\rm BV}\chi_\rho}\left[\frac{\mathrm{d}}{\mathrm{d}r}\left(c_p\tilde{T}\right)-\frac{\mathrm{d}}{\mathrm{d}r}\left(c_p\nabla_{ad}\tilde{p}\right)\right]=0, \quad \text{(B.49)}$$

and

$$-\tilde{\xi}_r+\frac{1}{m^2\omega^2R}\left(\frac{1}{\rho_0}\frac{\partial\left(p_0\tilde{p}\right)}{\partial r}+\frac{g_0}{\chi_\rho}\tilde{p}\right)-\frac{\chi_Tg_0}{\chi_\rho m^2\omega^2R}\tilde{T}=-\frac{2f}{m^2\omega^2}\frac{r}{R}, \quad \text{(B.50)}$$

where the expression for the gravitational acceleration is used as $\boldsymbol{g}=-\boldsymbol{\nabla}\Phi_0=-g_0\hat{r}$, therefore $g_0=\frac{\partial\Phi_0}{\partial r}$, which, because of the approximate equilibrium, can be re-expressed as $g_0=\frac{1}{\rho_0}\frac{\partial p_0}{\partial r}$. The expression for the perturbing potential has been re-expressed using $\Phi_P=-\frac{Gm_P}{4D^3}r^2=fr^2$ (as the perpendicular and time dependent functions of all variables have already been separated out) where $f=-\frac{Gm_P}{4D^3}$. Also, $\frac{\partial s_0}{\partial r}=c_P\frac{A_{\rm BV}}{r}\frac{\chi_\rho}{\chi_T}$ where $A_{\rm BV}=\frac{N^2}{g_0}r$, as it is defined in MESA, and the other variables have previously been defined.

To clarify what happened to the equations: equation B.47 was multiplied by $\frac{r^2}{\rho_0R^2}$, equation B.48 was multiplied by $\frac{r^2}{R^2m\omega\rho_0T_0c_p}$, equation B.49 was multiplied by $\frac{\partial r}{\partial T_0}$, and equation B.50 was multiplied by $\frac{1}{\rho_0m^2\omega^2R}$.

# Appendix C

# Detailed explanation of the general Henyey Method

## C.1 Introduction

This is an explanation, record and walkthrough of the derivation and origin of the equations used in the code to solve the stellar oscillation equations using the Henyey method. Initially the discussion will be fairly abstract and general, but this will become more and more specific as we go along.

To start with, we will address the structure of the method overall, to get a feel for the big picture to try to avoid getting bogged down in details. Then we will move through the relevant sections of the method in sequence, first with the recurrence relations for $\boldsymbol{\alpha}$ and $\boldsymbol{\gamma}$; we will then discuss the application of the outer boundary conditions; finishing off with a discussion of the recurrence relation for $\boldsymbol{u}$ and $\boldsymbol{v}$.

## C.2 Overall structure

To start with, the structure of the equations must be set out. This method is used to solve four linear, first order differential equations. Whilst it is not necessary in general, here we will be restricting ourselves to the case where the two pairs of variables are on a staggered grid, with $\boldsymbol{u}$ being evaluated at the outer edge of the cell, and $\boldsymbol{v}$ being evaluated at the centre of the cell, where $\boldsymbol{u} = (a, b)^T$ and $\boldsymbol{v} = (c, d)^T$

The boundary equations are split, two apply at the centre ($\boldsymbol{u} = 0$) and two apply at the surface of the star. Because of this, it is difficult to work with a solution from one boundary to the other, as the problem is under-constrained until all boundary conditions can be applied.

In order to get around this, the Henyey method uses a two-stage approach. A relation between $\boldsymbol{u}$ and $\boldsymbol{v}$ is used, which is formulated in such a way that conditions upon the coefficients can be found which reproduce the central boundary condition. This relation is

$$\boldsymbol{u}_k + \boldsymbol{\alpha}_k \boldsymbol{v}_k + \boldsymbol{\gamma}_k = 0, \tag{C.1}$$

which obeys the central boundary condition if $\boldsymbol{\alpha}_0 = 0$ and $\boldsymbol{\gamma}_0 = 0$ are used as a surrogate. Recurrence relations for the coefficients in this equation ($\boldsymbol{\alpha}$ and $\boldsymbol{\gamma}$) are used to calculate the values of these coefficients at each point, including at the surface. Using the surface boundary conditions with the outermost coefficients, the values for $\boldsymbol{u}$ and $\boldsymbol{v}$ can be evaluated. Then, another recurrence relation can be found, which relates the values of $\boldsymbol{\alpha}$, $\boldsymbol{\gamma}$, $\boldsymbol{u}$ and $\boldsymbol{v}$ at a given point, to the values of $\boldsymbol{u}$ and $\boldsymbol{v}$ at the adjacent point just inside. This enables them to be evaluated at all points throughout the star, and the solution is complete. This process is shown diagrammatically in figure 2.1.

To describe this problem more specifically, we must look at the structure of the equations in question, and the variables involved. Two equations involve the derivative of $\boldsymbol{u}$ but not $\boldsymbol{v}$, and the other two include the derivative of $\boldsymbol{v}$ but not $\boldsymbol{u}$. Because of this, we can split the four equations into two matrix equations:

$$\mathbf{A}_{k,k+1}\boldsymbol{u}_k + \mathbf{C}_{k,k+1}\boldsymbol{u}_{k+1} + \mathbf{D}_{k,k+1}\boldsymbol{v}_{k+1} = \boldsymbol{M}_{k,k+1}, \tag{C.2}$$

and

$$\mathbf{E}_{k,k+1}\boldsymbol{u}_k + \mathbf{F}_{k,k+1}\boldsymbol{v}_k + \mathbf{H}_{k,k+1}\boldsymbol{v}_{k+1} = \boldsymbol{N}_{k,k+1}. \tag{C.3}$$

This structure means that the two equations with derivatives of $\boldsymbol{u}$ make up equation C.2, which is evaluated at the midpoint of cell $k+1$; and the two equations with derivatives of $\boldsymbol{v}$ make up equation C.3, which is evaluated at the outer edge of cell k. Notably, this structure ensures that the matrices B and G, which would be included in a more general formulation, are ignored from the start, as they would be null at all points, which helps to avoid issues like trying to invert a singular matrix. In this discussion, the star is divided into $J$ cells, so $k$ will run from 0 to $J-1$.

## C.3 Outward-going recurrence relations

The relation $\boldsymbol{u}+\boldsymbol{\alpha v}+\boldsymbol{\gamma}=0$ is formulated this way as it enables the central boundary condition to be re-expressed as $\boldsymbol{\alpha}=0$ and $\boldsymbol{\gamma}=0$ at the centre. By combining this initial condition with a recurrence relation, we can iterate outwards to find their values at all points in the star.

There are many different ways to formulate the recurrence relation, which will all be mathematically equivalent, although the particular form of the relations may have some computational effects, depending on how they are implemented. The relevant equations are equations C.1, C.2 and C.3. The key idea is to use these equations to reflect the structure of equation C.1, evaluated at $k+1$, and to compare coefficients in order to get the equations for $\boldsymbol{\alpha}_{k+1}$ and $\boldsymbol{\gamma}_{k+1}$.

For ease of reading, the subscripts on the coefficients in equations C.2 and C.3 will be dropped, but the $k, k+1$ subscripts are implied, and any other subscripts will be explicitly stated.

Use equation C.3 to substitute for $\boldsymbol{v}_k$ in equation C.1, giving

$$\boldsymbol{v}_k = \mathbf{F}^{-1}\left(\boldsymbol{N}-\mathbf{E}\boldsymbol{u}_k-\mathbf{H}\boldsymbol{v}_{k+1}\right), \tag{C.4}$$

which leads to

$$\begin{aligned}\mathbf{u}_k+\boldsymbol{\alpha}_k\mathbf{F}^{-1}\left(\boldsymbol{N}-\mathbf{E}\boldsymbol{u}_k-\mathbf{H}\boldsymbol{v}_{k+1}\right)+\boldsymbol{\gamma}_k=0&\\ \longrightarrow \boldsymbol{u}_k=\left(1-\boldsymbol{\alpha}_k\mathbf{F}^{-1}\mathbf{E}\right)^{-1}\left(\boldsymbol{\alpha}_k\mathbf{F}^{-1}\left(\mathbf{H}\boldsymbol{v}_{k+1}-\boldsymbol{N}\right)-\boldsymbol{\gamma}_k\right),&\end{aligned} \tag{C.5}$$

which can be used to eliminate $\boldsymbol{u}_k$ in equation C.2, as

$$\begin{aligned}\boldsymbol{u}_{k+1}+\mathbf{C}^{-1}\left(\mathbf{D}+\mathbf{A}\left(1-\boldsymbol{\alpha}_k\mathbf{F}^{-1}\mathbf{E}\right)^{-1}\boldsymbol{\alpha}_k\mathbf{F}^{-1}\mathbf{H}\right)\boldsymbol{v}_{k+1}&\\ -\mathbf{C}^{-1}\left(\boldsymbol{M}+\mathbf{A}\left(1-\boldsymbol{\alpha}_k\mathbf{F}^{-1}\mathbf{E}\right)^{-1}\left(\boldsymbol{\alpha}_k\mathbf{F}^{-1}\boldsymbol{N}+\boldsymbol{\gamma}_k\right)\right)=0.&\end{aligned} \tag{C.6}$$

This gives us the required recurrence relations as

$$\boldsymbol{\alpha}_{k+1}=\mathbf{C}^{-1}\left(\mathbf{D}+\mathbf{A}\left(1-\boldsymbol{\alpha}_k\mathbf{F}^{-1}\mathbf{E}\right)^{-1}\boldsymbol{\alpha}_k\mathbf{F}^{-1}\mathbf{H}\right), \tag{C.7}$$

and

$$\boldsymbol{\gamma}_{k+1} = -\mathbf{C}^{-1}\left(\boldsymbol{M} + \mathbf{A}\left(1 - \boldsymbol{\alpha}_k \mathbf{F}^{-1}\mathbf{E}\right)^{-1}\left(\boldsymbol{\alpha}_k \mathbf{F}^{-1}\boldsymbol{N} + \boldsymbol{\gamma}_k\right)\right). \tag{C.8}$$

## C.4 Outer boundary

In order to apply the outer boundary condition, it must be expressed in the similar terms to the discretised equations, that is, it must be formed as:

$$\boldsymbol{\eta}\,\boldsymbol{u}_{J-2} + \boldsymbol{\mu}\,\boldsymbol{u}_{J-1} + \boldsymbol{\nu}\,\boldsymbol{v}_{J-1} = \boldsymbol{x}. \tag{C.9}$$

In order to evaluate the variables without extrapolation this equation is evaluated at the centre of the outer-most cell. Whilst this is not at the very outermost location of the model, the boundary conditions are taken to be valid in the case that the outer cells are sufficiently small that the change over half a cell has a negligible impact.

In order to get values for $\boldsymbol{u}_{J-1}$ and $\boldsymbol{v}_{J-1}$, we must combine equation C.9 with equations C.2, C.3 and C.1, all evaluated for $k = J-2$. This gives us four equations for four unknowns, which is a closed set of independent equations, so can be solved.

Multiply equation C.3 by $\boldsymbol{\alpha}_{J-2}\mathbf{F}^{-1}$ from the left, and use equation C.1 to eliminate $\boldsymbol{\alpha}_{J-2}\boldsymbol{v}_{J-2}$, giving

$$\boldsymbol{\alpha}_{J-2}\mathbf{F}^{-1}\mathbf{E}\boldsymbol{u}_{J-2} - \boldsymbol{u}_{J-2} - \boldsymbol{\gamma}_{J-2} + \boldsymbol{\alpha}_{J-2}\mathbf{F}^{-1}\mathbf{H}\boldsymbol{v}_{J-1} = \boldsymbol{\alpha}_{J-2}\mathbf{F}^{-1}\boldsymbol{N} \tag{C.10}$$

which can be rearranged to give an expression for $\boldsymbol{u}_{J-2}$

$$\begin{aligned}\left(\boldsymbol{\alpha}_{J-2}\mathbf{F}^{-1}\mathbf{E} - 1\right)\boldsymbol{u}_{J-2} + \boldsymbol{\alpha}_{J-2}\mathbf{F}^{-1}\mathbf{H}\boldsymbol{v}_{J-1} &= \boldsymbol{\alpha}_{J-2}\mathbf{F}^{-1}\boldsymbol{N} + \boldsymbol{\gamma}_{J-2} \\ \longrightarrow \boldsymbol{u}_{J-2} = \left(\boldsymbol{\alpha}_{J-2}\mathbf{F}^{-1}\mathbf{E} - 1\right)^{-1}&\left(\boldsymbol{\alpha}_{J-2}\mathbf{F}^{-1}\boldsymbol{N} + \boldsymbol{\gamma}_{J-2} - \boldsymbol{\alpha}_{J-2}\mathbf{F}^{-1}\mathbf{H}\boldsymbol{v}_{J-1}\right).\end{aligned} \tag{C.11}$$

This enables $\boldsymbol{u}_{J-2}$ to be eliminated, but, for simplicity, we first eliminate $\boldsymbol{u}_{J-1}$ from equations C.9 and C.2.

Multiply equation C.9 by $\boldsymbol{\mu}^{-1}$, and equation C.2 by $\mathbf{C}^{-1}$, giving

$$\boldsymbol{\mu}^{-1}\boldsymbol{\eta}\,\boldsymbol{u}_{J-2}+\boldsymbol{u}_{J-1}+\boldsymbol{\mu}^{-1}\boldsymbol{\nu}\,\boldsymbol{v}_{J-1}=\boldsymbol{\mu}^{-1}\boldsymbol{x}, \tag{C.12}$$

and

$$\mathbf{C}^{-1}\mathbf{A}\boldsymbol{u}_{J-2}+\boldsymbol{u}_{J-1}+\mathbf{C}^{-1}\mathbf{D}\boldsymbol{v}_{J-1}=\mathbf{C}^{-1}\boldsymbol{M}. \tag{C.13}$$

Taking the difference of these equations allows us to get an expression for $\boldsymbol{v}_{J-1}$ in terms of $\boldsymbol{u}_{J-2}$, as

$$\left(\boldsymbol{\mu}^{-1}\boldsymbol{\eta}-\mathbf{C}^{-1}\mathbf{A}\right)\boldsymbol{u}_{J-2}+\left(\boldsymbol{\mu}^{-1}\boldsymbol{\nu}-\mathbf{C}^{-1}\mathbf{D}\right)\boldsymbol{v}_{J-1}=\boldsymbol{\mu}^{-1}\boldsymbol{x}-\mathbf{C}^{-1}\boldsymbol{M} \tag{C.14}$$

which gives, when equation C.11 is used to substitute an expression for $\boldsymbol{u}_{J-2}$:

$$\begin{aligned}\left(\boldsymbol{\mu}^{-1}\boldsymbol{\eta}-\mathbf{C}^{-1}\mathbf{A}\right)\left(\boldsymbol{\alpha}_{J-2}\mathbf{F}^{-1}\mathbf{E}-1\right)^{-1}\left(\boldsymbol{\alpha}_{J-2}\mathbf{F}^{-1}\boldsymbol{N}+\boldsymbol{\gamma}_{J-2}-\boldsymbol{\alpha}_{J-2}\mathbf{F}^{-1}\mathbf{H}\boldsymbol{v}_{J-1}\right)\\ +\left(\boldsymbol{\mu}^{-1}\boldsymbol{\nu}-\mathbf{C}^{-1}\mathbf{D}\right)\boldsymbol{v}_{J-1}=\boldsymbol{\mu}^{-1}\boldsymbol{x}-\mathbf{C}^{-1}\boldsymbol{M}.\end{aligned} \tag{C.15}$$

This can then be rearranged for an expression for $\boldsymbol{v}_{J-1}$ as

$$\begin{aligned}\boldsymbol{v}_{J-1}=&\left(\boldsymbol{\mu}^{-1}\boldsymbol{\nu}-\mathbf{C}^{-1}\mathbf{D}+\left(\boldsymbol{\mu}^{-1}\boldsymbol{\eta}-\mathbf{C}^{-1}\mathbf{A}\right)\left(1-\boldsymbol{\alpha}_{J-2}\mathbf{F}^{-1}\mathbf{E}\right)^{-1}\boldsymbol{\alpha}_{J-2}\mathbf{F}^{-1}\mathbf{H}\right)^{-1}\\ &\left(\boldsymbol{\mu}^{-1}\boldsymbol{x}-\mathbf{C}^{-1}\boldsymbol{M}+\left(\boldsymbol{\mu}^{-1}\boldsymbol{\eta}-\mathbf{C}^{-1}\mathbf{A}\right)\left(1-\boldsymbol{\alpha}_{J-2}\mathbf{F}^{-1}\mathbf{E}\right)^{-1}\left(\boldsymbol{\gamma}_{J-2}+\boldsymbol{\alpha}_{J-2}\mathbf{F}^{-1}\boldsymbol{N}\right)\right).\end{aligned} \tag{C.16}$$

This can be simplified further by using expressions for $\boldsymbol{\alpha}_{J-1}$ and $\boldsymbol{\gamma}_{J-1}$, and by using the expression $\boldsymbol{\mu}^{-1}\boldsymbol{\mu}=1$ to give:

$$\boldsymbol{v}_{J-1}=\left(\boldsymbol{\nu}-\boldsymbol{\mu}\,\boldsymbol{\alpha}_{J-1}+\boldsymbol{\eta}\,\mathbf{A}^{-1}\left(\mathbf{C}\,\boldsymbol{\alpha}_{J-1}-\mathbf{D}\right)\right)^{-1}\left(\boldsymbol{x}+\boldsymbol{\mu}\,\boldsymbol{\gamma}_{J-1}-\boldsymbol{\eta}\,\mathbf{A}^{-1}\left(\mathbf{C}\boldsymbol{\gamma}_{J-1}-\boldsymbol{M}\right)\right). \tag{C.17}$$

## C.5 Inward-going recurrence relation

At this point, $\boldsymbol{\alpha}_k$ and $\boldsymbol{\gamma}_k$ are known at all points, and both $\boldsymbol{u}_{J-1}$ and $\boldsymbol{v}_{J-1}$ are known. In order to find the solution at all points in the star, a recurrence relation must be found in order to express $\boldsymbol{u}_k$ or $\boldsymbol{v}_k$ in terms of $\boldsymbol{u}_{k+1}$ and $\boldsymbol{v}_{k+1}$. This doesn't match the title of the section, but that is just a simple shift in dummy variable to match my previous working, and to make it so that the implied subscripts of $k, k+1$ are still valid.

There are two ways to go about this, which is essentially a choice of which equation to use: equation C.2 or C.3.

### C.5.1 Case I

Because of previous choices, Case I uses equation C.3. We substitute for $\boldsymbol{u}_k$ using equation C.1, and rearrange for $\boldsymbol{v}_k$, giving

$$-\mathbf{E}\,\boldsymbol{\alpha}_k\boldsymbol{v}_k - \mathbf{E}\boldsymbol{\gamma}_k + \mathbf{F}\boldsymbol{v}_k + \mathbf{H}\boldsymbol{v}_{k+1} = \boldsymbol{N} \longrightarrow \boldsymbol{v}_k = (\mathbf{F} - \mathbf{E}\,\boldsymbol{\alpha}_k)^{-1}(\boldsymbol{N} + \mathbf{E}\boldsymbol{\gamma}_k - \mathbf{H}\boldsymbol{v}_{k+1})\,. \quad \text{(C.18)}$$

Relating this to the generalised expression given in equation 2.27, we have $\boldsymbol{f}_k = \boldsymbol{v}_k$; $\mathbf{RECu}_k = 0$; $\mathbf{RECv}_k = -(\mathbf{F} - \mathbf{E}\,\boldsymbol{\alpha}_k)^{-1}\mathbf{H}$; and finally $\boldsymbol{RECc}_k = (\mathbf{F} - \mathbf{E}\,\boldsymbol{\alpha}_k)^{-1}(\boldsymbol{N} + \mathbf{E}\boldsymbol{\gamma}_k)$.

### C.5.2 Case II

Case II uses equation C.2. This rearrangement is pretty simple, and gives us:

$$\boldsymbol{u}_k = \mathbf{A}^{-1}(\boldsymbol{M} - \mathbf{C}\boldsymbol{u}_{k+1} - \mathbf{D}\boldsymbol{v}_{k+1})\,. \quad \text{(C.19)}$$

Relating this to the generalised expression given in equation 2.27, we have $\boldsymbol{f}_k = \boldsymbol{u}_k$; $\mathbf{RECu}_k = -\mathbf{A}^{-1}\mathbf{C}$; $\mathbf{RECv}_k = -\mathbf{A}^{-1}\mathbf{D}$; and finally $\boldsymbol{RECc}_k = \mathbf{A}^{-1}\boldsymbol{M}$.

# Appendix D

# Euler angles and rotations

In calculating the response of the star, it is greatly simplified by working in the star's natural frame of reference, $(\theta_*, \phi_*)$, with the planet orbiting in the plane defined by $\theta_* = \pi/2$. In this frame, the observer if taken to be in the direction given by $(\theta_0, \phi_0)$. In the observer's frame, described by $(\theta_{\rm ob}, \phi_{\rm ob})$, the observer is at $\theta_{\rm ob} = 0$, with $\theta_{\rm ob} < \pi/2$ visible to the observer.

To convert between the two frames, we use the properties of spherical harmonics and Euler angles, guided by Morrison & Parker (1987). The two frames of reference are related to each other by a rotation given by

$$\boldsymbol{e}_{z_*} = \mathbf{R}^{(\rm a)}(\alpha, \beta, \gamma)\boldsymbol{e}_{z_{\rm ob}}, \tag{D.1}$$

with $\boldsymbol{e}_{z_*}$ being a unit vector in the star's frame, and $\boldsymbol{e}_{z_{\rm ob}}$ being the corresponding unit vector in the observer's frame. The operator $\mathbf{R}^{(\rm a)}(\alpha, \beta, \gamma)$ is equivalent to $\mathbf{R}_{z_{\rm ob}}(\alpha)\mathbf{R}_{y_{\rm ob}}(\beta)\mathbf{R}_{z_{\rm ob}}(\gamma)$ where the active convention for rotations is being used, and the $y_{\rm ob}$ and $z_{\rm ob}$ axes are those of the observer's frame. The Euler angles are found to be $(\alpha, \beta, \gamma) = (0, -\theta_0, -\phi_0)$.

This leads to the relation between a given spherical harmonic, $Y_l^m$, between the two frames as

$$Y_l^m(\theta_*, \phi_*) = \sum_{\mu=-l}^{l} Y_l^\mu(\theta_{\rm ob}, \phi_{\rm ob}) D^l_{\mu,m}(0, -\theta_0, -\phi_0) \tag{D.2}$$

where $D^l_{\mu,m}(\alpha, \beta, \gamma)$ is an element of the Wigner D-matrix.

The relevance of this on the system of interest is that the tidal potential $\phi_{\rm P}$ of the hot Jupiter (or any companion) can be expressed as a sum of spherical harmonics, and the lowest order (in terms of $R/D$, where $R$ is the stellar radius and $D$ is the semi-major axis of the orbiting body) non-constant term is:

$$\phi_{\rm P} \approx \Re\left(-\frac{Gm_{\rm p}}{4D}\left(\frac{r}{D}\right)^2 P_2^2(\cos\theta_*)\mathrm{e}^{2i(\omega t - \phi_*)}\right), \tag{D.3}$$

where $G$ is Newton's gravitational constant, $\omega$ is the angular frequency of the planet's orbit, $t$ is the time, measured from the start point defining the coordinate system, $m_{\rm p}$ is the planet's mass, $r$ is the radial position in the star, and $P_2^2(\cos\theta_*) = 3\sin^2\theta_*$ is the associated Legendre polynomial. This relates to spherical harmonics, as $Y_2^{-2}(\theta_*,\phi_*) = \frac{1}{4}\sqrt{\frac{15}{2\pi}}\sin^2\theta_* e^{-2i\phi_*}$. Since this is the only source of time and angular dependence in the system of linear equations describing the response of the star, any perturbed quantity $q'$ can be written as:

$$q'(r,\theta_*,\phi_*,t) = \Re\left(q'(r)\times 3\sin^2\theta_* e^{2i(\omega t-\phi_*)}\right). \tag{D.4}$$

By using equation D.2, this can be expressed in the coordinates of the observer's frame. The great benefit of this comes when integrating over the visible disc, as its limits are $\theta_{\rm ob}\in\{0,\frac{\pi}{2}\}$, and $\phi_{\rm ob}\in\{0,2\pi\}$. If integrating over the visible disc without any weighting in $\phi$, the complex expression in equation D.2 can be simplified by the fact that $\int_0^{2\pi} e^{im\phi}d\phi$ is non–zero (and equal to $2\pi$) only when $\mu = 0$. Therefore:

$$\int_0^{2\pi} Y_2^{-2}(\theta_*,\phi_*)d\phi_{\rm ob} = \int_0^{2\pi} D^2_{0,-2}(0,-\theta_0,-\phi_0)Y_2^0(\theta_{\rm ob},\phi_{\rm ob})d\phi_{\rm ob}.$$

Using:

$$D^2_{0,-2}(0,-\theta_0,-\phi_0) = \sqrt{\frac{3}{8}}\sin^2\theta_0 e^{-2i\phi_0},$$

and:

$$Y_2^0(\theta_{\rm ob},\phi_{\rm ob}) = \frac{1}{2}\sqrt{\frac{5}{4\pi}}\left(3\cos^2\theta_{\rm ob}-1\right),$$

we obtain the useful expression:

$$\int_0^{2\pi} d\phi_{\rm ob}\sin^2\theta_* e^{-2i\phi_*} = \pi\sin^2\theta_0 e^{-2i\phi_0}(3\cos^2\theta_{\rm ob}-1). \tag{D.5}$$

Therefore, the integral over the visible disc of a perturbed quantity which angular dependence is given by equation (D.4) is:

$$\int_0^{2\pi} d\phi_{\rm ob} q'(R,\theta_{\rm ob},\phi_{\rm ob},t) = 3\pi\Re\left[q'(R)(3\cos^2\theta_{\rm ob}-1)\sin^2\theta_0 e^{2i(\omega t-\phi_0)}\right], \tag{D.6}$$

where it is important to note the change from $\theta_*$ and $\phi_*$ to $\theta_0$ and $\phi_0$ in the sine function and exponential respectively, compared to equation D.4.

# Appendix E

# Luminosity variation derivation

Here, the details of the derivation of the luminosity variation are given and justified. The results derived below are used in section 4.2.1. The method followed is similar to that of Robinson et al. (1982), the primary difference being that this work explicitly keeps track of the non–radial perturbations to displacement, $\boldsymbol{\xi}_h$.

## E.1 Surface normal

The change in surface normal due to the oscillations is calculated by normalising:

$$\frac{\partial \boldsymbol{r}}{\partial \theta_{\rm ob}} \times \frac{\partial \boldsymbol{r}}{\partial \phi_{\rm ob}},$$

where $\boldsymbol{r}$ is the location of the surface, given by $R\hat{\boldsymbol{r}} + \boldsymbol{\xi}$, with $\boldsymbol{\xi}$ being the vector displacement of the surface. The calculation is done in the observer's frame. This leads to an expression for the perturbed normal to the surface as $\hat{\boldsymbol{n}} = \hat{\boldsymbol{r}} + \Delta\hat{\boldsymbol{n}}$, where the perturbation is:

$$\Delta\hat{\boldsymbol{n}} = \frac{1}{R}\left[\hat{\boldsymbol{\theta}}_{\rm ob}\left(\xi_\theta - \frac{\partial \xi_r}{\partial \theta_{\rm ob}}\right) + \hat{\boldsymbol{\phi}}_{\rm ob}\left(\xi_\phi - \frac{1}{\sin\theta_{\rm ob}}\frac{\partial \xi_r}{\partial \phi_{\rm ob}}\right)\right], \tag{E.1}$$

where $\xi_r$ and $\xi_\theta$ are evaluated at $(r, \theta_{\rm ob}, \phi_{\rm ob})$ and $\xi_\theta = \partial V/\partial\theta_{\rm ob}$.

Note that no rescaling is necessary to first order, and that the perturbation to the normal acts only perpendicular to the radial direction.

This yields a change of luminosity:

$$\Delta L_n = \int_0^{\pi/2}\int_0^{2\pi} h_0 \bar{F}_0 \Delta\hat{\boldsymbol{n}}\cdot\hat{\boldsymbol{n}}_{\rm ob}\,{\rm d}S_0, \tag{E.2}$$

with ${\rm d}S_0 = R^2\sin\theta_{\rm ob}{\rm d}\theta_{\rm ob}{\rm d}\phi_{\rm ob}$, and $\hat{\boldsymbol{n}}_{\rm ob}$ is in the direction of the $z$–axis in the observer's frame, so that $h_0 = c(1-u+u\cos\theta_{\rm ob})$. Using:

$$\Delta\hat{\boldsymbol{n}}\cdot\hat{\boldsymbol{n}}_{\rm ob} = \frac{-\sin\theta_{\rm ob}}{R}\frac{\partial}{\partial\theta_{\rm ob}}\left(V - \xi_r\right), \tag{E.3}$$

equation (E.2) becomes:

$$\Delta L_n = -RF_0 c \int_0^{\pi/2} \mathrm{d}\theta_{\mathrm{ob}} \Bigg\{ \sin^2\theta_{\mathrm{ob}} (1 - u + u\cos\theta_{\mathrm{ob}}) \\ \frac{\partial}{\partial \theta_{\mathrm{ob}}} \int_0^{2\pi} \mathrm{d}\phi_{\mathrm{ob}} \left[ V(R, \theta_{\mathrm{ob}}, \phi_{\mathrm{ob}}) - \xi_r(R, \theta_{\mathrm{ob}}, \phi_{\mathrm{ob}}) \right] \Bigg\}. \tag{E.4}$$

The integral over $\phi_{\mathrm{ob}}$ is given by equation (D.6), and after integration over $\theta_{\mathrm{ob}}$ we finally obtain:

$$\Delta L_n = \Re \left[ \frac{9}{2} \pi R c \left( 1 - \frac{7u}{15} \right) F_0 \left[ V(R) - \xi_r(R) \right] \sin^2\theta_0 \mathrm{e}^{2\mathrm{i}(\omega t - \phi_0)} \right]. \tag{E.5}$$

## E.2 Limb-darkening

Limb-darkening is given as:

$$h = c \left[ 1 - u \left( 1 - \hat{\boldsymbol{n}} \cdot \hat{\boldsymbol{n}}_{\mathrm{ob}} \right) \right], \tag{E.6}$$

where the variables are as described in section 4.2.1. This is perturbed through the normal to the surface, giving:

$$h = c \left[ 1 - u \left( 1 - \hat{\boldsymbol{r}} \cdot \hat{\boldsymbol{n}}_{\mathrm{ob}} \right) \right] + cu \Delta\hat{\boldsymbol{n}} \cdot \hat{\boldsymbol{n}}_{\mathrm{ob}}, \tag{E.7}$$

in which the first term is $h_0$, and the second is defined as $\Delta h$, with $\Delta\hat{\boldsymbol{n}} \cdot \hat{\boldsymbol{n}}_{\mathrm{ob}}$ given by equation (E.3).

This results in a change in luminosity of the form

$$\Delta L_h = \int_0^{\pi/2} \int_0^{2\pi} \Delta h \bar{F}_0 \hat{\boldsymbol{r}} \cdot \hat{\boldsymbol{n}}_{\mathrm{ob}} \mathrm{d}S_0. \tag{E.8}$$

This integral is calculated in the same way as the integral (E.2) which gives $\Delta L_n$, and this leads to the final expression:

$$\Delta L_h = \Re \left[ \frac{12\pi}{5} R c u F_0 \left[ V(R) - \xi_r(R) \right] \sin^2\theta_0 \mathrm{e}^{2\mathrm{i}(\omega t - \phi_0)} \right]. \tag{E.9}$$

## E.3 Flux

The emergent flux is defined as $\bar{F} = \boldsymbol{F} \cdot \hat{\boldsymbol{n}}$, which assumes that all flux which reaches the surface is radiated isotropically (or, more precisely, that the anisotropy is included through limb-darkening). This separates into the equilibrium and perturbed quantities as

$$\bar{F} = (F_0 \hat{\boldsymbol{r}} + \Delta\boldsymbol{F}) \cdot (\hat{\boldsymbol{r}} + \Delta\hat{\boldsymbol{n}}) = F_0 + \Delta\boldsymbol{F} \cdot \hat{\boldsymbol{r}}, \tag{E.10}$$

where second order terms in small quantities have been neglected, and the fact that $\hat{\boldsymbol{r}}\cdot\Delta\hat{\boldsymbol{n}} = 0$ has been used. $\Delta\boldsymbol{F}$ is the Lagrangian perturbed flux, equal to $\boldsymbol{F'} + (\boldsymbol{\xi}\cdot\nabla)\boldsymbol{F}_0$, where the prime indicates an Eulerian perturbation.

Therefore, the perturbation to the emergent flux can be finally expressed as:

$$\Delta\bar{F} = \Delta\boldsymbol{F}\cdot\hat{\boldsymbol{r}} = F_r' + \xi_r\frac{\mathrm{d}F_0}{\mathrm{d}r}, \tag{E.11}$$

where the subscript italic $r$ indicates the radial component.

This results in a change in luminosity as:

$$\Delta L_F = \int_0^{\pi/2}\int_0^{2\pi} h_0\Delta\bar{F}\,\hat{\boldsymbol{r}}\cdot\hat{\boldsymbol{n}}_{\mathrm{ob}}\mathrm{d}S_0. \tag{E.12}$$

With $F_r'$ and $\xi_r$ in $\Delta\bar{F}$ being evaluated at $(R,\theta_{\mathrm{ob}},\phi_{\mathrm{ob}})$, the integral over $\phi_{\mathrm{ob}}$ is here again given by equation (D.6). After integration over $\theta_{\mathrm{ob}}$ we then obtain:

$$\Delta L_F = \Re\left[\frac{3\pi}{4}R^2 c\left(1+\frac{u}{15}\right)\left(F_r'(R)+\xi_r(R)\frac{\mathrm{d}F_0}{\mathrm{d}r}\right)\sin^2\theta_0 \mathrm{e}^{2\mathrm{i}(\omega t-\phi_0)}\right]. \tag{E.13}$$

## E.4 Surface area

In the observer's frame, the surface area element is defined as $\mathrm{d}S_{(\mathrm{ob,P})} = r^2_{(\mathrm{ob,P})}\sin\theta_{(\mathrm{ob,P})}\mathrm{d}\theta_{(\mathrm{ob,P})}\mathrm{d}\phi_{(\mathrm{ob,P}}$ where the subscript $(\mathrm{ob,P})$ indicates that the coordinates are measured in the observer's frame and take into account the perturbation.
At equilibrium, the vector position of a point at the surface of the star is given by $\boldsymbol{r} = R\hat{\boldsymbol{r}}$ and its coordinates are $(R,\theta_{\mathrm{ob}},\phi_{\mathrm{ob}})$. When the star is perturbed, this point is moved and its vector position becomes:

$$\boldsymbol{r}_{\mathrm{P}} = \boldsymbol{r} + \boldsymbol{\xi} = (R+\xi_r)\hat{\boldsymbol{r}} + \xi_\theta\hat{\boldsymbol{\theta}}_{\mathrm{ob}} + \xi_\phi\hat{\boldsymbol{\phi}}_{\mathrm{ob}}. \tag{E.14}$$

Writing the displacement $\boldsymbol{r}_{\mathrm{P}} - \boldsymbol{r}$ as $\Delta r\hat{\boldsymbol{r}} + R\Delta\theta_{ob}\hat{\boldsymbol{\theta}}_{\mathrm{ob}} + R\sin\theta_{\mathrm{ob}}\Delta\phi_{\mathrm{ob}}\hat{\boldsymbol{\phi}}_{\mathrm{ob}}$ and identifying with equation (E.14) yields the perturbed coordinates of the point:

$$\begin{aligned}
r_{(\mathrm{ob,P})} &\equiv R + \Delta r = R + \xi_r,\\
\theta_{(\mathrm{ob,P})} &\equiv \theta_{\mathrm{ob}} + \Delta\theta_{ob} = \theta_{\mathrm{ob}} + \frac{\xi_\theta}{R},\\
\phi_{(\mathrm{ob,P})} &\equiv \phi_{\mathrm{ob}} + \Delta\phi_{ob} = \phi_{\mathrm{ob}} + \frac{\xi_\phi}{R\sin\theta_{\mathrm{ob}}}.
\end{aligned}$$

To first order in the perturbation we then obtain:

$$\begin{aligned}
r^2_{(\mathrm{ob,P})} &= R^2 + 2R\xi_r,\\
\sin\theta_{(\mathrm{ob,P})} &= \sin\theta_{\mathrm{ob}} + \frac{\xi_\theta}{R}\cos\theta_{\mathrm{ob}},
\end{aligned}$$

and we use the Jacobian to change the variables over which we are integrating as:

$$\mathrm{d}\theta_{(\mathrm{ob,P})}\mathrm{d}\phi_{(\mathrm{ob,P})} = \left[1 + \frac{1}{R}\left(\frac{\partial \xi_\theta}{\partial \theta_{\mathrm{ob}}} + \frac{1}{\sin\theta_{\mathrm{ob}}}\frac{\partial \xi_\phi}{\partial \phi_{\mathrm{ob}}}\right)\right]\mathrm{d}\theta_{\mathrm{ob}}\mathrm{d}\phi_{\mathrm{ob}}, \tag{E.15}$$

where second order terms have been neglected.
Using $\Delta\mathrm{d}S = \mathrm{d}S_{(\mathrm{ob,P})} - \mathrm{d}S_0$, where $\mathrm{d}S_0 = R^2\sin\theta_{\mathrm{ob}}\mathrm{d}\theta_{\mathrm{ob}}\mathrm{d}\phi_{\mathrm{ob}}$, gives the expression for the change in surface area element as:

$$\Delta\mathrm{d}S = R\left[\sin\theta_{\mathrm{ob}}\left(2\xi_r + \frac{\partial \xi_\theta}{\partial \theta}\right) + \cos\theta_{\mathrm{ob}}\xi_\theta + \frac{\partial \xi_\phi}{\partial \phi_{\mathrm{ob}}}\right]\mathrm{d}\theta_{\mathrm{ob}}\mathrm{d}\phi_{\mathrm{ob}}, \tag{E.16}$$

where second order terms in the perturbation have been neglected.

The change in luminosity due to this effect is given by

$$\Delta L_S = \int_0^{\pi/2}\int_0^{2\pi} h_0\bar{F}_0\hat{\boldsymbol{r}}\cdot\hat{\boldsymbol{n}}_{\mathrm{ob}}\Delta\mathrm{d}S. \tag{E.17}$$

To calculate this integral, $\xi_\phi(\theta_*,\phi_*)$ has to be transformed into $\xi_\phi(\theta_{\mathrm{ob}},\phi_{\mathrm{ob}})$ in the expression (E.16) for $\Delta\mathrm{d}S$. This involves summing up over the spherical harmonics $Y_l^\mu$, as indicated in equation (D.2). However, only the non–zero values of $\mu$ contribute to $\partial\xi_\phi/\partial\phi_{\mathrm{ob}}$, and the corresponding spherical harmonics give zero when integrated over $\phi_{\mathrm{ob}}$ in equation (E.17). Therefore, the term involving $\xi_\phi$ does not contribute. As above, using $\xi_\theta = \partial V/\partial\theta_{\mathrm{ob}}$ and equation (D.6) to calculate the integral over $\phi_{\mathrm{ob}}$, we obtain after integration over $\theta_{\mathrm{ob}}$:

$$\Delta L_S = \Re\left[\frac{3}{2}\pi Rc\left(1+\frac{u}{15}\right)F_0\left[\xi_r(R) - 3V(R)\right]\sin^2\theta_0 \mathrm{e}^{2\mathrm{i}(\omega t-\phi_0)}\right]. \tag{E.18}$$

## E.5 Limits

The limits of the visible disc, and therefore of any integrals, are given by the points at which the vector towards the observer is tangential to the surface, such that $\hat{\boldsymbol{n}}_{\mathrm{ob}}\cdot\boldsymbol{r} = 0$, which can be re-expressed as $\hat{\boldsymbol{n}}_{\mathrm{ob}}\cdot(\hat{\boldsymbol{r}} + \Delta\hat{\boldsymbol{n}}) = 0$, where $\Delta\hat{\boldsymbol{n}}$ is the change in surface normal, given in section E.1. For simplicity of notation, we can rewrite this as $\Delta\hat{\boldsymbol{n}} = A\hat{\boldsymbol{\theta}}_{\mathrm{ob}} + B\hat{\boldsymbol{\phi}}_{\mathrm{ob}}$, where $A$ and $B$ are both first order in the perturbation and can be found by identifying this expression with equation (E.1).

Since $\hat{\boldsymbol{n}}_{\mathrm{ob}} = \hat{\boldsymbol{z}}$ in the observer's frame, this leads to the expression for the limits to be given by $\hat{\boldsymbol{r}}\cdot\hat{\boldsymbol{z}} + A\hat{\theta}\cdot\hat{\boldsymbol{z}} + B\hat{\phi}\cdot\hat{\boldsymbol{z}} = 0$, which becomes $\cos\theta_{\mathrm{up}} - A\left(\theta_{\mathrm{up}}\right)\sin\theta_{\mathrm{up}} = 0$, where $\theta_{\mathrm{up}}$ is the coordinate of the point which delimits the visible disc and we have made it explicit that $A$ depends on $\theta_{\mathrm{ob}}$. Since the limit is $\pi/2$ at equilibrium, we write $\theta_{\mathrm{up}} = \pi/2 + \delta\theta$. The equation above then becomes, to first order in $\delta\theta$, $\delta\theta = -A_0$, where

$A_0$ is the value of $A$ at $\theta_{\rm ob} = \pi/2$. We have used $A\left(\theta_{\rm up}\right) = A_0 + \frac{\partial A}{\partial \theta_{\rm ob}}\delta\theta$ and neglected the second term on the right–hand side, which is second order in the perturbation.

This leads to the change in luminosity:

$$\Delta L_L = \int_0^{2\pi}\int_{\frac{\pi}{2}}^{\frac{\pi}{2}-A_0} h_0 \bar{F}_0 \hat{\boldsymbol{n}}_{\rm ob}\cdot\hat{\boldsymbol{r}}\,{\rm d}S_0. \tag{E.19}$$

Since $A_0$ depends on $\phi_{\rm ob}$, we have to integrate over $\theta_{\rm ob}$ first. This yields:

$$\Delta L_L = -\int_0^{2\pi} cR^2\bar{F}_0\left(\frac{u\sin^3 A_0}{3} + \frac{(1-u)\sin^2 A_0}{2}\right){\rm d}\phi_{\rm ob}, \tag{E.20}$$

which is equal to 0 to first order in $A$, which is a small quantity. Therefore, any change in luminosity due to a change in the limits of the integral can be neglected to first order.

# Appendix F

# Radial velocity variation derivation

Here, the details of the derivation of the radial velocity variation are given and fully justified. The results derived below are used in section 4.2.2.

The periodic change in shape of the star results in a periodic change in the velocity of any given surface element. Projecting this along the observer's line of sight gives the radial velocity (RV) which is proportional to the shift in wavelength caused by the motion (for the very non–relativistic motions considered here). Expressing this formally gives:

$$\mathrm{v_{RV}} = -\dot{\boldsymbol{r}} \cdot \hat{\boldsymbol{n}}_{\mathrm{ob}}, \tag{F.1}$$

where $\boldsymbol{r}$ is the vector from the centre of the star to the surface element in question.

To first order in perturbed quantities, this becomes:

$$\mathrm{v_{RV}} = -\dot{\boldsymbol{\xi}} \cdot \hat{\boldsymbol{n}}_{\mathrm{ob}} = \Re\left(-2\mathrm{i}\omega \boldsymbol{\xi} \cdot \hat{\boldsymbol{n}}_{\mathrm{ob}}\right) \tag{F.2}$$

This can be encapsulated by a single curve by integrating over the disk, weighted by the luminosity, as done by Dziembowski (1977):

$$\mathrm{v_{disc}} = \frac{\iint \mathrm{h}\hat{\boldsymbol{r}} \cdot \hat{\boldsymbol{n}}_{\mathrm{ob}} \bar{\mathrm{F}}_0 \mathrm{v_{RV}} \mathrm{dS}_0}{\iint \int \mathrm{h}\hat{\boldsymbol{r}} \cdot \hat{\boldsymbol{n}}_{\mathrm{ob}} \bar{\mathrm{F}}_0 \mathrm{dS}_0} = \frac{1}{2\pi \mathrm{R}^2} \int_0^{\pi/2} \int_0^{2\pi} \mathrm{h}\hat{\boldsymbol{r}} \cdot \hat{\boldsymbol{n}}_{\mathrm{ob}} \mathrm{v_{RV}} \mathrm{dS}_0, \tag{F.3}$$

which can be analytically solved.

Using $\mathrm{d}S_0 = R^2 \sin\theta_{\mathrm{ob}} \mathrm{d}\theta_{\mathrm{ob}} \mathrm{d}\phi_{\mathrm{ob}}$, $\hat{\boldsymbol{n}}_{\mathrm{ob}} = \hat{\boldsymbol{z}}$, and $\xi_\theta = \partial V / \partial \theta_{\mathrm{ob}}$, we obtain:

$$\begin{aligned} \mathrm{v_{disc}} = \Re \Bigg\{ & \frac{-\mathrm{i}\omega \mathrm{R}^2}{\pi} \int_0^{\pi/2} \mathrm{d}\theta_{\mathrm{ob}} h \cos\theta_{\mathrm{ob}} \sin\theta_{\mathrm{ob}} \\ & \left[ \cos\theta_{\mathrm{ob}} \int_0^{2\pi} \xi_r\left(R, \theta_{\mathrm{ob}}, \phi_{\mathrm{ob}}\right) \mathrm{d}\phi_{\mathrm{ob}} \right. \\ & \left. - \sin\theta_{\mathrm{ob}} \frac{\partial}{\partial \theta_{\mathrm{ob}}} \int_0^{2\pi} V\left(R, \theta_{\mathrm{ob}}, \phi_{\mathrm{ob}}\right) \mathrm{d}\phi_{\mathrm{ob}} \right] \Bigg\} \end{aligned} \tag{F.4}$$

The integrals over $\phi_{\rm ob}$ are given by equation (D.6), which yields:

$$\begin{aligned} \mathrm{v_{disc}} = \Re \Big\{ -3\mathrm{i}\omega \sin^2\theta_0 \mathrm{e}^{2\mathrm{i}(\omega \mathrm{t}-\phi_0)} \times \\ \int_0^{\frac{\pi}{2}} \mathrm{d}\theta_{\rm ob} \mathrm{c}\,(1-\mathrm{u}+\mathrm{u}\cos\theta_{\rm ob})\cos\theta_{\rm ob}\sin\theta_{\rm ob} \times \\ \left[\xi_r(R)\left(3\cos^2\theta_{\rm ob}-1\right)\cos\theta_{\rm ob}+6V(R)\cos\theta_{\rm ob}\sin^2\theta_{\rm ob}\right]\Big\}. \end{aligned} \tag{F.5}$$

Evaluating this integral gives the final expression for the disc-integrated radial velocity as:

$$\mathrm{v_{disc}} = \Re\left\{ -\frac{4}{5}\mathrm{i}\omega \mathrm{c}\sin^2\theta_0 \mathrm{e}^{2\mathrm{i}(\omega \mathrm{t}-\phi_0)} \left[\left(1-\frac{\mathrm{u}}{16}\right)\xi_{\mathrm{r}}(\mathrm{R})+3\left(1-\frac{3\mathrm{u}}{8}\right)\mathrm{V}(\mathrm{R})\right]\right\}. \tag{F.6}$$

# Appendix G

# Non–disc–integrated approaches

Whilst we are unable to spatially resolve the surface of the star, there are still some possibilities for observing signals without simply taking the average effect.

## G.1 Inhomogeneous line broadening

Because of the different motions across the visible surface of the stellar disc, different parts of the stellar surface will emit light which has been Doppler shifted differently. Instead of taking the average of the total Doppler shift by looking at the variation in the central wavelength, we can examine the variation in the line–broadening by tracking how the brightness at each wavelength changes over the course of the oscillation.

By summing the luminosity contributions at each wavelength we determine the overall shape of the line–broadening that results from the non–uniform surface motion. This can be expressed as:

$$\frac{\mathrm{d}L(\mathrm{v})}{\mathrm{d}\mathrm{v}} = \frac{1}{\Delta\mathrm{v}} \sum_{\mathrm{v}-\frac{\Delta\mathrm{v}}{2}}^{\mathrm{v}+\frac{\Delta\mathrm{v}}{2}} h\cos\theta_{\mathrm{ob}}\bar{F}_0\mathrm{d}S_0, \tag{G.1}$$

where $\Delta\mathrm{v}$ is the width of the bin. This sums over only the area elements that fall within the bin centred on $\mathrm{v}$.

In general, the resulting shape will not be simple, and can have significant luminosity at radial velocities much greater than the disc–integrated value. All viewing angles will produce this broadening, with greatest time–dependence when the system is viewed edge–on, and a steady state when viewed at either pole.

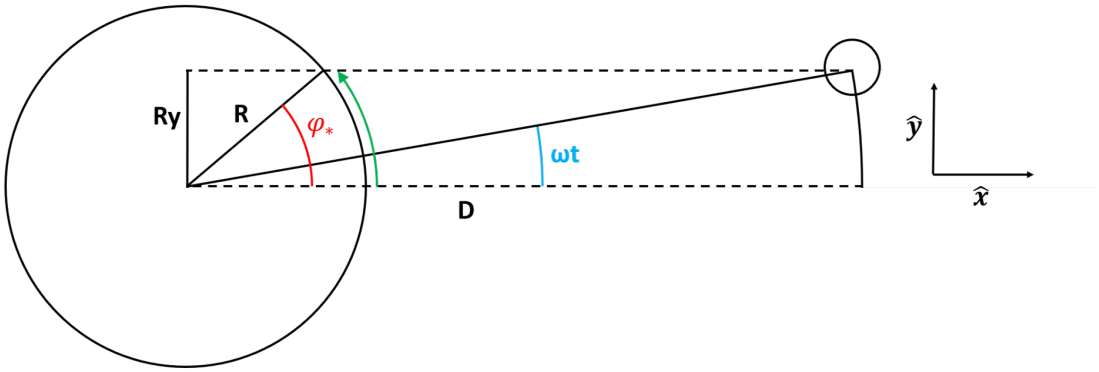


Figure G.1: This figure depicts the coordinates used in section G.2, as viewed from above the plane of the planet's orbit, in the case that $\delta\theta = 0$. The observer is at infinity in the $\hat{\boldsymbol{x}}$ direction, and at $t = 0$ the planet is at $(D, 0)$ in the $(x, y)$ plane. After time $t$ the planet has moved to be approximately at $(D, D\omega t)$ and the location which is blocked by the planet's silhouette has moved from $(R, 0)$ to $(R\cos\phi_*, Ry)$, as shown by the green arrow, where $y$ is the the dimensionless coordinate introduced for eq. G.5.

## G.2 Observations during transit

In the case of a transiting planet, a portion of the star is blocked from view by the planet, enabling the behaviour of the surface at that specific location to be studied. As the stellar oscillations occur at twice the orbital frequency, subtracting the signal whilst the planet is occluded (secondary eclipse) from the signal during the transit will isolate the signal from the blocked portion of the stellar surface.

We define $\delta\theta = \pi/2 - i$, where $i$ is the orbital inclination. Since the planet is transiting, $|\delta\theta| \leq R/D \ll 1$ is a small quantity. We therefore describe the stellar surface as if $\delta\theta = 0$ (that is, as if we view it exactly edge–on), which corresponds to $\theta_0 = \pi/2$, but allow the planet's silhouette to deviate from being exactly edge–on. As the transit occurs over an interval of time short compared to the oscillation period, we assume that the motion of the surface is constant for the duration of the transit, and that the planet's motion is linear. These introduce fractional errors of order $R/D$. This arrangement is shown diagrammatically in Figure G.1.

The centre of the silhouette will cross the stellar surface according to:

$$R\sin\theta_*\sin\phi_* = D\omega t, \tag{G.2}$$

with:

$$R\cos\theta_* = D\delta\theta, \tag{G.3}$$

We assume $\phi_0 = 0$, as the origin of the phase is arbitrary, which implies that $t = 0$ corresponds to the centre of the transit. This gives:

$$\cos\theta_* = \frac{D}{R}\delta\theta,$$
$$\sin\phi_* = \frac{D\omega t}{R\sqrt{1-(\frac{D\delta\theta}{R})^2}}.$$

#### G.2.0.1 Radial velocity

We have $\xi_\theta = \partial V/\partial\theta_*$, $\xi_\phi = (\partial V/\partial\phi_*)/\sin\theta_*$ and $\hat{n}_{\rm ob} = \hat{\boldsymbol{x}}$. Both $\xi_r$ and $V$ are given by equation (D.4), in which $\omega t$ is taken to be zero as the transit happens over a time interval short compared to the period of the oscillations, as already mentioned above. Therefore, equation F.2 can be written as:

$$\mathrm{v_{RV}}(\theta_*,\phi_*) = \Re\left\{-6\mathrm{i}\omega\sin\theta_*\mathrm{e}^{-2\mathrm{i}\phi_*}\left[\xi_\mathrm{r}(\mathrm{r})\sin\theta_*\hat{\boldsymbol{r}} + 2\mathrm{V}(\mathrm{r})\left(\cos\theta_*\hat{\boldsymbol{\theta}}_* - \mathrm{i}\hat{\boldsymbol{\phi}}_*\right)\right]\cdot\hat{\boldsymbol{x}}\right\}, \tag{G.4}$$

which we now re–express in terms of $\delta\theta$ and $t$.

Introducing the coordinates $y = \frac{D\omega t}{R}$ and $z = \frac{D\delta\theta}{R}$ we get

$$\mathrm{v_{RV}}(y,z) = \frac{-6\omega}{1-z^2}\left[2y\sqrt{1-y^2-z^2} + \mathrm{i}\left(1-2y^2-z^2\right)\right] \times\left\{\sqrt{1-y^2-z^2}\left[\xi_r + z^2\left(2V-\xi_r\right)\right] + 2\mathrm{i}Vy\right\} \tag{G.5}$$

which is valid over the range $y^2+z^2<1$.

To describe the approximate width of the obscured $\mathrm{v_{RV}}$, we can use

$$\Delta\mathrm{v_{RV}} \approx \max\left(\frac{\partial \mathrm{v}_{RV}}{\partial y}\frac{R_P}{R}, \frac{\partial \mathrm{v}_{RV}}{\partial z}\frac{R_P}{R}\right) \tag{G.6}$$

where $R_P$ is the planetary radius. The luminosity of the blocked region can also be found, as

$$L_{\rm blocked} = \pi R_P^2 h\bar{F}_0. \tag{G.7}$$

Equations G.6 and G.7 are valid once the entirety of the planet's silhouette is visible, or equivalently whilst $y^2+z^2<(1-\frac{R_P}{R})^2$.

The disc-integrated RV signal defines a line of solutions for $\xi_r$ and $V$, as it is one measurement being used to determine two complex values. By observing the variation in the radial velocity signal which is blocked during the transit the components can be separated, giving an independent measure of $\xi_r$ and $V$. Exactly how this works out in practise with real and imaginary components may not be straightforward, but it would be another way to look at the system and gain information.

#### G.2.0.2 Luminosity

The same technique could also be applied to variations in luminosity arising as a result of the transit, however this signal would be the result of the blocking of both the equilibrium flux and the perturbed flux. As such, the extra blocking due to the obscured perturbed flux would be very small, on the order of $\frac{R_P^2 F'}{R^2 F_0}$.

# Appendix H

# MESA inlists

Here the inlist used to create the 1.0 $M_{\odot}$ model used in chapter 3. To create the 1.4 $M_{\odot}$ model only the stellar mass was changed.

To create the models used to test the observed systems, a similar inlist was used, although the initial mass was changed to that given in table 4.1, such that the observed parameters were reproduced in an appropriate model.

```
! inlist to evolve a 1.0 solar mass star

&star_job
  ! begin with a pre-main sequence model
    create_pre_main_sequence_model = .true.
  ! save a model at the end of the run
    save_model_when_terminate = .false.
  ! display on-screen plots
    pgstar_flag = .true.
/ !end of star_job namelist

&controls
  ! starting specifications
    initial_mass = 1.0 ! in Msun units
  ! starting metallicity
    initial_z = 0.02d0
  ! mixing length
    mixing_length_alpha = 2
  ! stop when the star nears ZAMS (Lnuc/L > 0.99)
    Lnuc_div_L_zams_limit = 0.99d0
```

```
    stop_near_zams = .false.
  ! stop when the center mass fraction of h1 drops below this limit
    xa_central_lower_limit_species(1) = 'he4'
    xa_central_lower_limit(1) = 1d-3
  ! stop when star age reaches
    max_age = 11.58d9

   ! Maximum number of grid points allowed.
      max_allowed_nz = 17500
         ! mesh_delta_coeff
         ! A larger value increases the max allowed deltas and decreases
         !  the number of grid points.
         ! default is 1.0d0
      mesh_delta_coeff = 0.2d0

         !### max_center_cell_dq
         ! Largest allowed dq at center
         ! (dq = cell mass as fraction of total mass)
         ! default is 1d-7
      max_center_cell_dq = 1d-14

         !### mesh_delta_coeff_for_highT
         ! Use different mesh_delta_coeff at higher temperatures.
         ! default is 3.0d0
      mesh_delta_coeff_for_highT = 1.0d0

         !### profile_interval
         ! save a model profile info when
         ! `mod(model_number, profile_interval) = 0`.
      profile_interval = 20

/ ! end of controls namelist
```

# Bibliography


Alsubai K., et al., 2017, AJ, 153, 200

Arras P., Burkart J., Quataert E., Weinberg N. N., 2012, MNRAS, 422, 1761

Beichman C., et al., 2014, PASP, 126, 1134

Biermann L., 1932, ZAp, 5, 117

Borucki W. J., et al., 2011, ApJ, 736, 19

Brickhill A. J., 1983, MNRAS, 204, 537

Brickhill A. J., 1992, MNRAS, 259, 529

Brown T. M., Gilliland R. L., Noyes R. W., Ramsey L. W., 1991, ApJ, 368, 599

Brown D. J. A., Collier Cameron A., Hall C., Hebb L., Smalley B., 2011, MNRAS, 415, 605

Bunting A., Papaloizou J. C. B., Terquem C., 2019, MNRAS, 490, 1784

Burkart J., Quataert E., Arras P., Weinberg N. N., 2012, MNRAS, 421, 983

Chandrasekhar S., 1939, An introduction to the study of stellar structure. The University of Chicago press

Chaplin W. J., Miglio A., 2013, ARA&A, 51, 353

Coughlin J. L., et al., 2016, ApJS, 224, 12

Cox J. P., 1976, ARA&A, 14, 247

Csizmadia S., et al., 2011, A&A, 531, A41

Cunha M. S., et al., 2007, A&A Rev., 14, 217

Darwin G. H., 1879, Philosophical Transactions of the Royal Society of London Series I, 170, 1

Deubner F.-L., Gough D., 1984, ARA&A, 22, 593

Di Mauro M. P., 2017, Proceedings of Frontier Research in Astrophysics - II, Proceedings of Science, 269, 29

Dziembowski W., 1977, Acta Astron., 27, 203

Dziembowski W. A., 2016, Commmunications of the Konkoly Observatory Hungary, 105, 23

Faigler S., Mazeh T., 2011, MNRAS, 415, 3921

Fuller J., 2017, MNRAS, 472, 1538

Garg A., et al., 2010, AJ, 140, 328

Goldreich P., Nicholson P. D., 1989, ApJ, 342, 1079

Gough D. O., 1977, ApJ, 214, 196

Hart A. B., 1954, MNRAS, 114, 17

Henyey L. G., Forbes J. E., Gould N. L., 1964, ApJ, 139, 306

Heynderickx D., Waelkens C., Smeyers P., 1994, A&AS, 105, 447

Hoffleit D., 1997, Journal of the American Association of Variable Star Observers (JAAVSO), 25, 115

Hotta H., Rempel M., Yokoyama T., Iida Y., Fan Y., 2012, A&A, 539, A30

Houdek G., Dupret M.-A., 2015, Living Reviews in Solar Physics, 12, 8

Howard R., Harvey J., 1970, Solar Physics, 12, 23

Howard A. W., et al., 2012, ApJS, 201, 15

Howarth I. D., Morello G., 2017, MNRAS, 470, 932

Huang C. X., et al., 2020, ApJ, 892, L7

Jakeman E., Parry G., Pike E. R., Pusey P. N., 1978, Contemporary Physics, 19, 127

Jetsu L., Porceddu S., 2015, PLoS ONE, 10

Kjeldsen H., et al., 2003, The Astronomical Journal, 126, 1483

Kupka F., Muthsam H. J., 2017, Living Reviews in Computational Astrophysics, 3, 1

Lai D., 1997, ApJ, 490, 847

Leighton R. B., Noyes R. W., Simon G. W., 1962, ApJ, 135, 474

Maciejewski G., Knutson H. A., Howard A. W., Isaacson H., Fernández-Lajús E., DiSisto R. P., Migaszewski C., 2020a, Acta Astron., 70, 1

Maciejewski G., Niedzielski A., Villaver E., Konacki M., Pawłaszek R. K., 2020b, ApJ, 889, 54

Markham S., Stevenson D., 2018, Icarus, 306, 200

Masuda K., 2014, ApJ, 783, 53

Mayor M., Queloz D., 1995, Nature, 378, 355

Mazeh T., Faigler S., 2010, A&A, 521, L59

Mazeh T., Nachmani G., Sokol G., Faigler S., Zucker S., 2012, A&A, 541, A56

Mislis D., Hodgkin S., 2012, MNRAS, 422, 1512

Mitalas R., Sills K. R., 1992, ApJ, 401, 759

Morrison M. A., Parker G. A., 1987, Australian Journal of Physics, 40, 465

Paxton B., Bildsten L., Dotter A., Herwig F., Lesaffre P., Timmes F., 2011, ApJS, 192, 3

Paxton B., et al., 2013, ApJS, 208, 4

Paxton B., et al., 2015, ApJS, 220, 15

Paxton B., et al., 2018, ApJS, 234, 34

Paxton B., et al., 2019, ApJS, 243, 10

Penoyre Z., Stone N. C., 2019, AJ, 157, 60

Pfahl E., Arras P., Paxton B., 2008, ApJ, 679, 783

Plaskett H. H., 1916, ApJ, 43, 145

Quataert E. J., Kumar P., Ao C. O., 1996, ApJ, 463, 284

Robinson E. L., Kepler S. O., Nather R. E., 1982, ApJ, 259, 219

Salaris M., Cassisi S., 2008, A&A, 487, 1075

Savonije G. J., Papaloizou J. C. B., 1983, MNRAS, 203, 581

Shporer A., et al., 2019, AJ, 157, 178

Smeyers P., Willems B., Van Hoolst T., 1998, A&A, 335, 622

Szabó G. M., Pál A., Derekas A., Simon A. E., Szalai T., Kiss L. L., 2012, MNRAS, 421, L122

Taylor A., Taylor J., 1806, Rhymes for the Nursery. By the authors of "Original Poems", 1st edn. Darton and Harvey, London

Terquem C., Papaloizou J. C. B., Nelson R. P., Lin D. N. C., 1998, ApJ, 502, 788

Thorsett S. E., Arzoumanian Z., Taylor J. H., 1993, ApJ, 412, L33

Triaud A. H. M. J., et al., 2010, A&A, 524, A25

Ulrich R. K., 1970, ApJ, 162, 993

Unno W., 1967, PASJ, 19, 140

Unno W., Osaki Y., Ando H., Saio H., Shibahashi H., 1989, Nonradial oscillations of stars, 2nd edn. University of Tokyo Press, Tokyo

Weinberg N. N., Arras P., Quataert E., Burkart J., 2012, ApJ, 751, 136

Welsh W. F., Orosz J. A., Seager S., Fortney J. J., Jenkins J., Rowe J. F., Koch D., Borucki W. J., 2010, ApJ, 713, L145

Welsh W. F., et al., 2011, ApJS, 197, 4

Willems B., 2003, MNRAS, 346, 968

Willems B., Aerts C., 2002, A&A, 384, 441

Willems B., van Hoolst T., Smeyers P., 2003, A&A, 397, 973

Winn J. N., Fabrycky D. C., 2015, ARA&A, 53, 409

Wolszczan A., Frail D. A., 1992, Nature, 355, 145

Wright J. T., Marcy G. W., Howard A. W., Johnson J. A., Morton T. D., Fischer D. A., 2012, ApJ, 753, 160